Effects of Dopants on the Power Factor of Tellurium Telluride Chalcogenide Nano System

By

Waqas Muhammad Khan

39-FBAS/PHDPHY/F14

Supervisor:

Dr. Wiqar Hussain Shah

(Associate Professor)

Department of Physics

Faculty of Basic and Applied Sciences

International Islamic University, Islamabad.

(2022)

Nanostructured materials

Chalcogenides

Tellurium telluride

Semiconductors electric properties

Nanotechnology materials

Chalcogenides effect of electricity on

Effects of Dopants on the Power Factor of Tellurium Telluride Chalcogenide Nano System

By

Waqas Muhammad Khan

(39-FBAS/PHDPHY/F14)

This Thesis was submitted to the Department of Physics, International Islamic University Islamabad for the award of a degree of Doctor of Philosophy in Physics.

Chairman, Department of Physics

International Islamic University, Islamabad

Dean Faculty of Basic and Applied Science

International Islamic University, Islamabad

(2022)

Final approval

It is certified that the work presented in this thesis entitled, **"Effects of Dopants on the Power Factor of Tellurium Telluride Chalcogenide Nano System"** by **Waqas Muhammad Khan**, Registration No. **39-FBAS/PHDPHY/F14** fulfills the requirements for the award of Doctor of Philosophy (PhD) Degree in Physics from Department of Physics, International Islamic University Islamabad, Pakistan.

Viva Voce Committee

Chairperson

Dr. Shaista Shahzada

Associate Professor, Department of Physics,

International Islamic University, Islamabad .....

Supervisor

Dr. Wiqar Hussain Shah

Associate Professor, Department of Physics,

International Islamic University, Islamabad .....

External Examiner

Dr. Iftikhar Hussain Gul,

Professor,NUST, H-12, Islamabad .....

External Examiner

Dr. Maaz,

Principal Scientist,

PINSTEC, Nilore, Islamabad .....

Internal Examiner

Dr. Kashif Nadeem

Associate Professor, Department of Physics,

International Islamic University, Islamabad .....

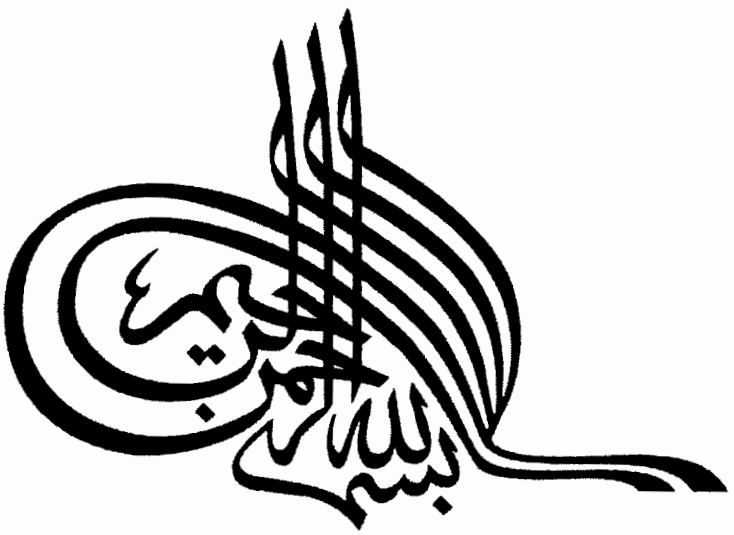

In the name of Allah,
the Most Beneficent,
the Most Merciful

Dedication

DEDICATED TO MY BELOVED TEACHERS, MY

LOVING

MY FATHER & (LATE) MOTHER, MY BROTHERS & SISTERS

WHO GIVE ME

SUPPORT AT EVERY STAGE OF LIFE.

Forwarding Sheet by Research Supervisor

The thesis titled **"Effects of Dopants on the Power Factor of Tellurium Telluride Chalcogenide Nano System"** *was* submitted by **Waqas Muhammad Khan** (Registration No: **39-FBAS /PHDPHY /F 14**) in partial fulfilment of his PhD degree in Physics has been completed under my supervision. I am satisfied with the quality of his research work and allow him to submit his thesis for further processing for a doctor of philosophy degree from the Department of Physics, FBAS, as per IIUI Islamabad rules and regulations.

Supervisor:

Dr. Wiqar Hussain Shah
Associate Professor
Department of Physics,
International Islamic University,
Islamabad, Pakistan.

Dated: 29-03-2022

Department of Physics,

International Islamic University (IIUI)

Islamabad Pakistan

Declaration of Originality

I hereby declare that the work contained in this dissertation and the intellectual content of this dissertation are the product of my work. This dissertation has not been previously published in any form nor does it contain any section of the published resources which could be treated as a deviation of the international copyright law.

I also declare that I do understand the terms 'copyright' and 'plagiarism,' and that in case of any copyright violation or plagiarism found in this work, I will be held fully responsible for the consequences of any such violation.

Signature: _____

Name: **Waqas Muhammad Khan**

Date: 29/09/22

Acknowledgement

I have no words to express my deepest sense of gratitude and numerous thanks to **Almighty Allah**, who enabled me to complete this study, and with innumerable blessings for the **Holy Prophet Muhammad (PBUH),** who is forever a torch of guidance and knowledge for the whole humanity. I would like to thank my supervisor **Dr. Wiqar Hussain Shah**, firstly for taking me on as a research student and then for providing support, and advice for letting me develop my ideas, and for helping me make it to the end. I would like to pay lots of appreciation to all my teachers. My journey wouldn't have been the same without the lab fellows for all the conversations that we had over the year. I also pay special thanks to my lab fellows **Tufail Ahmad, Liaqat Masum,** and **Muhammad Sabir Khan** for being helpful to me in all my research work. My humble and heartfelt gratitude is reserved for my beloved parents, brother, and sisters. Without their prayers and encouragement, the completion of this task would have been a dream for me.

Waqas Muhammad Khan

TABLE OF CONTENTS

LIST OF FIGURES

LIST OF TABLE

LIST OF PUBLICATIONS

I. Publications Included as a Co-Author

1. W. H. Shah*, A. Khan, **M. Waqas**, W.A. Syed. "**Effects of Pb Doping On the Seebeck Co-Efficient and Electrical Properties Of $Tl_{8.67}pb_xsb_{1.33-x}te_6$ Chalcogenide System.**" Chalcogenide Letters Vol. 14, No. 2, 2017, p. 61 – 68

2. W. H. Shah*, **W. M. Khan**, S. Tajudin, M. Tufail, W. A. Syed. "**Optimization of Power Factor in Sn doped $Tl_{10-x}sn_xte_6$ Thermoelectric Chalcogenide nano-Material.**" Chalcogenide Letters Vol. 14, No. 5, May 2017, p. 187 – 193

II. Publications Included as Part of Thesis

1. **W. M. Khan**, W. H. Shah, S. Shah, S. Khan, W. A. Syed, N. Ahmad, A. Safeen, K. Safeen."**Increasing The Power Factor By Sb Doped $Tl_{10-x}sb_xte_6$ In Chalcogenide System.**" Chalcogenide Letters Vol. 16, No. 7, July 2019, p. 343 – 349

2. **W. M. Khan**, W. H. Shah, M. Tufail, S. Khan, W. A. Syed, N. Ahmad. **"Enhancement Of Power Factor By Sn Doping In $Tl_8sb_{2-x}sn_xte_6$ Nano- Chalcogenide System."** Chalcogenide Letters Vol. 16, No. 8, August 2019, p. 395 – 403

3. **Waqas Muhammad Khan**, Altaf Ur Rahman, Muhammad Tufail, Muhammad Ibrar, Wiqar Hussain Shah, Waqar Adil Syed, Banat Gul. "**Toward controlled thermoelectric properties of Pb and Sb co-doped nanostructured Thallium Telluride for energy applications**". *MaterialsResearchExpress,* **2020,** *7* (10)105010.

4. W. M. Khan, W. H. Shah, N. Khan, M. Tufail, S. Khan, W. A. Syed. "**Effects On The Seebeck Co-Efficient and Electrical Properties of Tl_{10-x} Ate_6 (A= Pb & Sn) In Chalcogenide System.**" Journal of Ovonic Research Vol. 17, No. 2, March - April 2021, p. 201 - 208

LIST OF SYMBOLS

η_{max}	max maximum efficiency of a thermoelectric power generator
φ_{max}	max maximum efficiency of a thermoelectric refrigerator
zT	the dimensionless figure-of-merit of the thermo-element
σ	electrical conductivity
α	Seebeck coefficient
κ	thermal conductivity
T	temperature n carrier concentration
n	mobility; chemical potential
E_F	Fermi energy
k_B	Boltzmann constant
κ_E	electrical thermal conductivity
K_L	lattice thermal conductivity
g(E)	density of states
m*	density of states effective mass
N	number of degenerate valleys
m_d	density of states effective mass for individual valley
τ	relaxation time
e	elementary charge
Fj(η)	the j^{th} order Fermi integral
η	reduced chemical potential
λ	scattering parameter; thermal diffusivity
L	Lorenz number

C_V	heat capacity of the lattice per unit volume
υ	average phonon velocity
θ_D	Debye temperature
V_C	the unit cell volume
N	atom the number of atoms per cell
T_m	melting point
ρ_m	mass density
K_{min}	the minimum lattice thermal conductivity
$\hbar$	reduced Planck constant
Δ	the average volume per atom

LIST OF ABBREVIATIONS

PGEC	phonon-glass electron-crystal
XRD	X-ray diffraction
SEM	scanning electron microscopy
GSAS	General Structure Analysis System
EDX	energy dispersive X-ray analysis
DFT	density functional theory
LDA	local density approximation
GGA	generalized gradient approximation
APW	augmented plane wave
LMTO	linear muffin tin orbital method FP full-potential
LCAO	linear combination of atomic orbitals
TB	tight-binding method
ASA	atomic-spheres-approximation
DOS	density of states

Abstract

Thermoelectric materials (TEM) are the compounds that are capable of straightly changing the heat energy into electrical energy (Seebeck effect) or vice-versa (Peltier effect). Thermoelectric-based appliances are composed of solid-state materials such as p-type and n-type semiconductors which are coupled into the electrical circuit and display a temperature gradient. The efficiency of the compounds is investigated by the mathematical expression $ZT = \frac{S^2\sigma}{k} T$ where "S" represents the Seebeck coefficient, "σ" represents the electrical conductivity, "κ" is the thermal conductivity, "PF" is the power factor, and 'T" is the average of the coldest and hottest regions of the temperature. The ZT value is high for the best thermoelectric compounds mostly electrical appliances in utilization to show that ZT can be measured up to 3. The high-temperature change is composed of a high ZT value that increases to large-performance thermoelectric compounds that affect.

In the present research, optimization and advanced thermoelectric compounds are evaluated by different elements. Scientists are continuously in search of an advance material that has the leading properties: the quality of holding higher temperatures, thus enhanced the "T" term showing a high Seebeck coefficient and electrical conductivity controlled with doping methods and immediate low thermal conductivity, "κ". Nowadays, research observation has changed from "$S^2\sigma$" to "κ", which can help enhance the thermoelectric material fabricated from different methods to determine the complex crystal structure and initialization of structural defects such as nano-domains/nano-structuring. As a consequence of their trend in the configuration of complex crystal structures and bonding, Te-based compounds have enhanced the desire results for TE research and optimization. The compounds with Te anions added different heavy metals such as alkali (A) metals, alkaline earth (R) elements, or heavy p-block elements regarded with the triels (Tr), tetrels (Tt), or pnictogens (Pn) have enhanced a primary based of new and ground-breaking thermoelectric compounds. Similarly, improvement of the present thermoelectric compounds with these compositions has increased the ZT values to double those compared with the previous study.

Tl_5Te_3 is a well-studied thermoelectric compound. It is one of the which is change the thermoelectric area. It displayed narrow band-gap semiconducting characterization

that can be adjusted to p- or n-type values based on the doped process, and it's κ values are built-in low due to the existence of heavy elements and their composition. An ordering of quaternary compound $(SnTl)_x(PbTe_3)_y$ was laid down on be constructed via the modification of x: y.

In our research, various compounds were investigated as ternary and quaternary which may help to be used as thermoelectric compounds. TlSnTe and TlSbTe are the leading compounds due to their in order layering motifs and complex compositions. Phase range studies, crystal structure refinements, and synthesis optimizations to assure that the compounds were better- defined and showed the phase-pure in front of unsuccessful PF optimized. By sterilization the measure of progressive charge carriers in these compounds, modification in ZT can be determined this is carried through doping with primarily, heavy Tr elements Pb, Sn, and Sb. So that the physical characteristics are calculated and contrasted for a definite quantity Tl_9SnTe_6, Tl_9SbTe_6, etc.

As Tl is the sustainable element in this group and is noted that it exhibits both Tl^{+1} and Tl^{3+} cation forms and, in thermoelectric devices, dominate unambiguously the low κ values. Thallium telluride composites such as $Tl_{10}Te_6$ are thus rather applicable as physically found in this group. The ancestry composites are considered as Tl_9SnTe_6 – one of the improved substantial with PF = 10.2~$Wcm^{-1}K^{-2}$ (500 K) exploitation of a hot-pressed pellet. Herein, the system is expanded to include $Tl_{10-x}Sn_xTe_6$ which shows good TE potential of ZT ($Tl_{10}Sn_xTe_6$) = 0.6 (617 K) with a cold-pressed pellet. The incorporation of tetrels elements is investigated through measurements of $Tl_{10-x-y}Sn_xPb_yTe_6$ and also applies to the lesser-studied Tl_9SbTe_6 compound via research on the systems $Tl_9Sn_xSb_{1-x}Te_6$ and $Tl_9Pb_xSb_{1-x}Te_6$. Tt elements are systematically added to the $Tl_9[Tt]_xSb_{1-x}Te_6$ structure with $1.0 \leq x \leq 2.0$. Crystallographic studies, electronic structure calculations, and physical properties are explored for each series.

Due to the Te's ability to form complex Te–Te compounds in certain environments, the combination of alkaline earth metals, namely R = Sb with the chalcogenides (Q = Sn, Pb) and Te form a plethora of previously unknown crystal structures. Many of these are Zintl-phase narrow-band gap semiconductors with complex Q–Q bonding schemes combined with their heavy element incorporation the family is of great

interest to the thermos electrics community. The chalcogenide elements display unique Q–Q or Te–Te bonding with varying dimensional. The electronic structures and bonding calculations are reported for each compound, as they are the single crystal study. The first two of the aforementioned compounds are narrow-band gap semiconductors whereas the latter two exhibits metallic behavior.

(i) "Sn" doped $Tl_{10}Te_6$ nano-compound have been synthesized by ball milling method. The deformation of the density of states in the valence band of $Tl_{10}Te_6$ by "Sn" importantly raises the pristine Seebeck coefficient from ~ 80 $\mu V\ K^{-1}$ to ~ 158 $\mu V\ K^{-1}$. By the XRD investigation, our thermoelectric material has been found as a tetragonal structure. The flimsy modification of lattice parameters between different series of $Tl_{10}Te_6$ develops lattice disruption in the matrix which is one of the central components to decrease the lattice thermal conductivity by scattering heat-carrying phonons.

(ii) Co-doping of "Sb" with extra "Te" has been better designed for the thermoelectric compound. In contrast, the Seebeck coefficient of the "Sb" in the doped $Tl_{10}Te_6$ group displays a larger value than the pristine $Tl_{10}Te_6$. It can be evaluated that the larger valence band beginning of $Tl_{10}Te_6$ substantially decreased by "Sb" which accepted the heavy hole valence band to take part in the electron-hole transport scheme. It keeps point defects, nano-precipitates, and grain boundaries importantly increased power factor is ~ 10.2 $\mu Wcm^{-1}K^{-2}$ of the series of $Tl_{10}Te_6$ so it enhances the performance of thermoelectric characterization.

(iii) A dopant ratio of 1:2 between "Sn" and "Pb" interactivity developed electronic and thermal characterization of Sn/Sb co-doped $Tl_{10}Te_6$ system done with band application and structure technology. The high atomic mass variation allying guest (Pb) and host (Sb) atoms change the phonon scattering. Theoretical computation declared the adjustment of pristine $Tl_{10}Te_6$ band structure by Sn/Sb co-doping. The synchronisation of resonance energy level and valence band happens to enhance the electrical transport characterization. High density of "Sn" and "Pb" can fully powerfully scatter phonons and importantly increased the power factor from ~ 1.66 $\mu Wcm^{-1}K^{-2}$ to ~ 8.56 $\mu Wcm^{-1}K^{-2}$.

(iv) Sb/Sn co-doping in $Tl_{10}Te_6$ was successfully synthesized by the co-precipitation technique. Extended theoretical computing displayed important valence band occurrence and principal band gap enhancement which results in a rise in the PF from ~5.01 $\mu Wcm^{-1}K^{-}$ in the pristine $Tl_{10}Te_6$ to ~8.25 $\mu Wcm^{-1}K^{-}$ in the $Tl_{10}Te_6$. The co-existence of point defects, strain field, dislocations, and grain boundaries for important to increase the power factor.

(v)An grade-appropriate dopant ratio of 1:2 between "Sb" and "Pb" cooperatively reinforced the electronic and thermal characterizations of Sn/Sb co-doped TlTe system band application and structure technology. The large atomic mass fluctuation between the guest (Sb) and host (Sn) atoms strengthens the phonon scattering. Theoretical calculation suggests the modification of pristine $Tl_{10}Te_6$ band structure by Pb/Sb co-doping. The co-existence of resonance energy level and valence band convergence improved the electrical transport properties. High density of "Sn" and "Sb" rich nano-precipitates cause strain defects which can strongly scatter the phonons and reduce the lattice thermal conductivity leading to high *ZT*. We estimated the device efficiency based on average *ZT* and it was found that the device increases the efficiency which can be achieved.

(vi) "Sn" doped $Tl_{10}Te_6$ particles have been synthesized by using the ball milling technique. The distortion of the density of states in the valence band of $Tl_{10}Te_6$ by "Sn" significantly enhances the pristine power factor from ~ 4.7 $\mu Wcm^{-1}K^{-2}$ to ~ 10.2 $\mu Wcm^{-1}K^{-2}$. An extensive TEM analysis was performed to investigate the structure of $Tl_{10}Te_6$ nano-precipitate and a tetragonal crystal structure was observed. The slight variation of lattice parameters between $Tl_{10}Te_6$ evolves lattice dislocation in the matrix which is one of the key factors. This is accepting that the larger valence band firstly in a $Tl_{10}Te_6$ substantially decreased with the help of "Sn" than coincide heavy hole valence band to take part in electron hole transport system. More than that, many nano-precipitates were characterized in the matrix of $Tl_{10}Te_6$. A large number of point defects, nano-precipitates, and grain boundaries thereby improved the high thermoelectric performance.

Chapter 1

INTRODUCTION

1.1 Thermoelectric Phenomena

Resources such as petroleum and coal are rapidly depleting due to continued exploitation. The number of countries suffering from a lack of electrical energy is growing by the day. Last, during the thirty years, the rate of energy consumption on the Global level has almost increased this level of consumption up to 60% by 2030 shown in Fig.1.1.

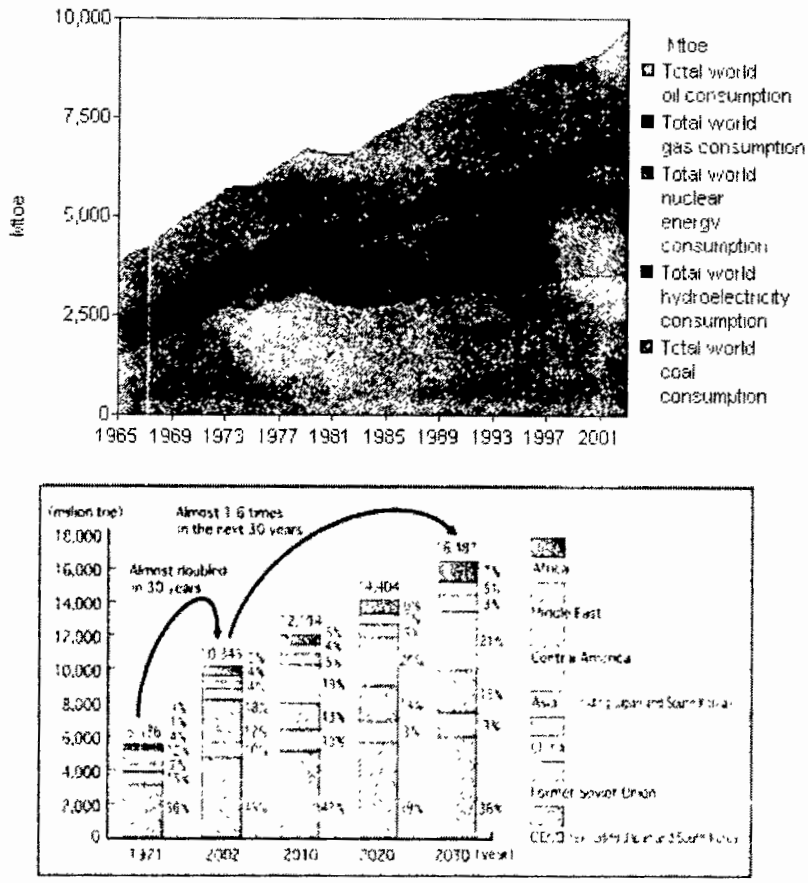

Figure.1.1: Global primary energy consumption, 1971-2030. [*Source: Energy White Paper 2005 Japan.*] [1]

According to a report by the International Energy Agency (IEA) and the Organization for Economic Co-operation and Development (OECD), it is estimated that in 1971, the consumption level of global energy increased to 5.5 billion toe (tonnes of oil equivalent) which was further increased to 10.3 billion toe (tonnes of oil equivalent) in 2002. Global energy demand is expected to reach 16.3 billion toe by

2030, which was 1.6 billion toe in 2002 [1]. Most of this massive energy consumption is lost to the atmosphere in terms of heat, which humans cannot use efficiently. It is important to look for a technique to convert this colossal amount of wasted heat into electric energy.

Because of traditional energy sources such as coal and petroleum, the importance of renewable energy sources has grown as people's willingness to consume them. People have been looking for new sources of energy to exchange for conventional fossil fuels, such as wave energy, nuclear energy, solar energy, water energy, geothermal energy, and wind energy [2].

However, despite the fact that new energy sources have been investigated by researchers, the efficiency of the previously mentioned alternative energy sources is typically low. According to Energie- Fakten [3] as of 2002, coal accounted for 23% of global energy sources, with 3.4 billion tonnes of coal equivalents (tCE) producing 7000 billion kWh of electricity. Coal-fired power plants are placing them among the most efficient power generation technologies available today, with a global average efficiency of around 31%. It is now widely accepted that coal-fired power plants can compete favorably with any other power generation technology. The majority of the energy produced by burning coal is lost as heat, amounting to roughly 70% of the total energy produced. If we can capture and convert even a small portion of it for use as electricity, we can produce twice the amount of electricity currently produced, which will meet the world's energy demand for the next few decades. According to Fig.1.1, about 60% will expect to increase global energy consumption by 2030. The sun, terrestrial heat, and heat from a car engine are all sources of heat energy in nature. As a result, thermoelectric energy generation is a top priority today. More energy can be obtained while also helping to preserve the environment.

The process of harvesting energy from the environment and storing it in a usable form is known as energy harvesting. This term is frequently used when referring to pollutants produced by the combustion of fossil fuels. The intermittent nature of some renewable sources is a major criticism [4].

"But a variety of renewable sources in combination can overcome this problem. The challenge of the variable power supply may be further alleviated by energy storage."

Hydrogen fuel cells, pumped-storage hydro systems, thermal mass, and batteries are among the available storage options. Energy storage systems can cost a lot up front but they pay off in the long run because they store energy. Renewable energy sources are frequently dismissed as untrustworthy. Major failures may be impossible with today's more efficient, diverse, dispersed, and renewable energy systems. Storage of renewable energy systems can also improve the system's reliability. Additionally, people may overlook the energy's low efficiency of utilization. A significant portion of the energy generated may be wasted [5]. As a result, the requirement for an

"Energy Management system, which mixes the energy available from a variety of sources, stores the surplus energy, routes it to a variety of sinks and efficiently controls the acquisition as well as the delivery to minimize energy wastage."

1.2 History of Thermoelectric Materials

1.2.1 Seebeck Effect

A German physicist named Johann Seebeck belong to the Baltic German merchant family, (Tallinn, April 9, 1770 - Berlin, December 10, 1831). He discovered that when two metals in a closed circuit i.e. a thermocouple, are not the same temperature, they deflect a compass magnet placed in proximity of the circuit when the circuit's two junctions have thermal variation. The angle of deflection changes depending on the variation in temperature between the two junctions of the circuit. This happened more than twenty years prior to Seebeck's discovery. Seebeck findings were published in 1821 [6] incorrectly assumed that the observed phenomenon was due to magnetism induced by temperature differences which eventually led him to think that the Earth's magnetic field was caused by variation of temperature in-between its two cold poles and its hot equator.

Using the linear relationship defining the Seebeck coefficient S for a material, the emf V generated at the two junctions is dependent on both the material and the temperature T_{12}.

$$\Delta V = S\,\Delta T_{12} \quad \ldots\ldots\ldots\ldots\ldots\ldots\ldots\ldots\ldots\ldots\ldots\ldots\ldots\ldots (1.1)$$

By connecting wire-A to B wire in a circuit, the Seebeck coefficient can be determined as shown in Fig.1.2. Two temperatures (T_1 and T_2) are maintained at the two junctions (the ends of wire A), and V is varied as shown in Fig. 1.2.

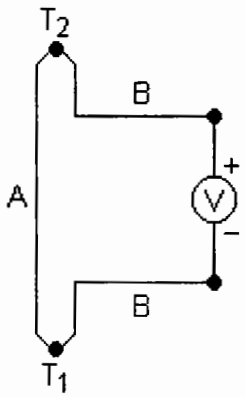

Figure 1.2: Experimental setup for measuring the Seebeck coefficient S.

If the B-leads at the voltmeter are kept at the same temperature, only terminals 1 and 2 need to be considered when calculating the voltage. If T_1 is greater than T_2 where electrons flow to T_1 making T_2 more positive.

$$V_b - V_a = S_A(T_2 - T)$$

$$V_c - V_b = S_B(T_1 - T_2)$$

$$V_d - V_c = S_A(T - T_1)$$

$$V = (V_b - V_a) + (V_c - V_b) + (V_d - V_c)$$

$$V = S_A T_2 - SA\ T + S_B T_1 - S_B T_2 + S_A T - S_A T_1$$

$$V = S_A(T_2 - T_1) - S_B(T_2 - T_1) = (S_A - S_B)(T_2 - T_1)$$

$$Q = q\ V = q\ (S_A - S_B)(T_2 - T_1)$$

$$dQ/dt = I\ (S_A - S_B)(T_2 - T_1) = I\ \Pi_{12} \quad \ldots\ldots\ldots\ldots\ldots\ldots\ldots\ldots\ (1.2)$$

1.2.2 Peltier Effect

The Seebeck effect along with new ideas about electromagnetism led to a new field of study about how heat can be changed into electricity. Jean Charles Athanasy Peltier (Ham, February 22, 1785–Paris, October 27, 1845), a French watchmaker and part-time physicist, discovered in 1834 that forcing a current across an iso-thermal junction of dissimilar metals as shown in Fig.1.3. They found that coolness and hotness of iso-thermal junction is depending on the direction of the current [7]. Peltier made every effort to explain the phenomenon in terms of the Joule theory of heat dissipation but he failed. Uncertainty about the physical origins of the effect continued until 1838, despite his best efforts. Heinrich Friedrich Emil Lenz (Dorpat, February 12, 1804 – Rome, February 10, 1865) the Russian physicist, demonstrated that Peltier's effect and Joule's effect are separate and unrelated physical phenomena

from each other. In this effect, when forcing the current across the junction of two dissimilar conductors, the heat is absorbed and eliminated from them [8].

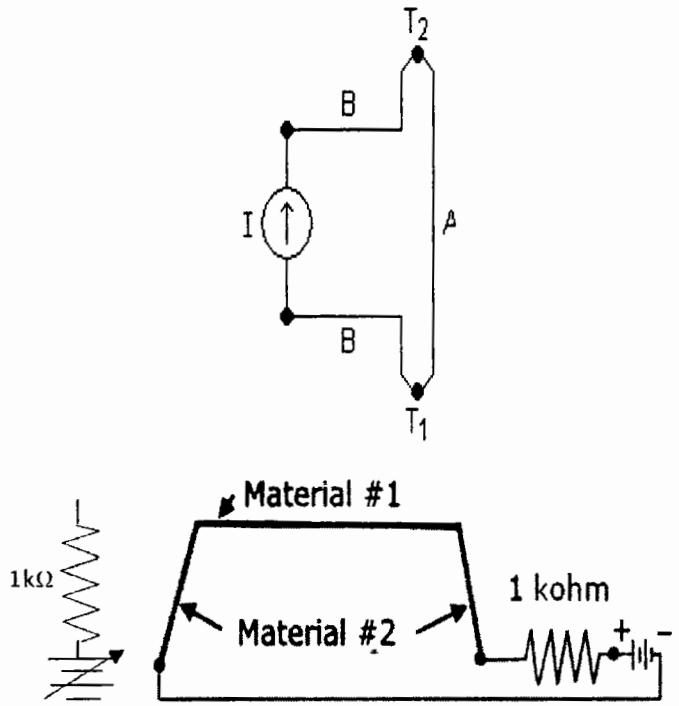

Figure 1.3: Experimental setup for measuring by Peltier coefficient

The Peltier effect has been dubbed the "Peltier coefficient" and quantified using the Peltier coefficient.

$$V_b - V_a = S_A(T_2 - T)$$

$$V_c - V_b = S_B(T_1 - T_2)$$

$$V_d - V_c = S_A(T - T_1)$$

$$V = (V_b - V_a) + (V_c - V_b) + (V_d - V_c)$$

$$V = S_A T_2 - S_A T + S_B T_1 - S_B T_2 + S_A T - S_A T_1$$

$$V = S_A(T_2 - T_1) - S_B(T_2 - T_1) = (S_A - S_B)(T_2 - T_1)$$

$$Q = q\,V = q\,(S_A - S_B)(T_2 - T_1)$$

$$dQ/dt = I\,(S_A - S_B)(T_2 - T_1) = I\,\Pi_{12} \quad \ldots\ldots\ldots\ldots\ldots\ldots\ldots\ldots\ldots\ldots (1.3)$$

Q shows the released or absorbed additional heat energy over the time at the junction, while I show the flow of electric current.

1.2.3 Thomson's Effect

In 1854, British mathematician and engineer William Thomson is better known as Lord Kelvin. Thomson (Belfast, June 26, 1824- Glasgow, December 17, 1907) wrote a detail thermodynamic behavior of the Seebeck and Peltier effects [9, 10]. He did fundamental works on the mathematical analysis of electricity and the first and second laws of thermodynamics origination at Glasgow University. He was able to predict the presence of a third thermoelectric effect. It indicates that when current pass from the homogeneous material with the temperature gradient. The released or absorbed the heat energy itself. He found that exchanging the heat amount is related to the temperature gradient and electric current. Also determined that whether the heat is absorbed or released is determined by the mutual direction of these two variables. It defines as the Thomson effect and Thomson Coefficient expresses this effect in equation (1.4).

$$\tau = \frac{q}{j.\Delta T} \quad \text{..... (1.4)}$$

where q denotes the absorb or release of the amount of heat over the volume and time. j denotes the current density. Finally, Thomson derived the Thomson coefficients. These coefficients were used for time-reversal-symmetric materials which are, [11]

$$\pi = \alpha T \quad \text{..... (1.5)}$$

$$\tau = T \frac{d\alpha}{dT} \quad \text{..... (1.6)}$$

by employing a methodology that is no longer widely accepted for the description of non-equilibrium thermodynamics [10].

1.2.4 Lars Onsager

Lars Onsager (Oslo, November 27, 1903–Coral Gables, October 5, 1976) the Norwegian-born American Physical Chemist, finally formulated a systematic way of describing the transport process in non-equilibrium states which is valid for the calculation of quasi-equilibrium in 1931 [12, 13]. Because of the extensive use of Onsager's thermoelectric theory, generalized Thomson coefficients for an isotropic non-time-reversal symmetric media could be derived in 1950 [14, 15] and are now cast in the form.

$$\bar{\bar{\pi}}(B) = \bar{\bar{\alpha}}'(-B)T \quad \text{..... (1.7)}$$

$$\bar{\bar{\tau}}(B) = T\frac{d\bar{\bar{\alpha}}'(-B)}{dT} \quad \text{..... (1.8)}$$

1.3 Electrical Conductivity in Metals.

Consider a conductor having a length (L) with a cross-sectional area (A) of a certain size. The electric current (I) is relative to the voltage drop (V) across the conductor, is known as Ohms Law, and can be calculated using the equation

$$V = IR. \quad \text{..... (1.9)}$$

We rewrite the above equation,

$$I = \frac{V}{R} \quad \text{..... (1.10)}$$

$$\frac{I}{A} = \frac{V}{AR} \quad \text{..... (1.11)}$$

$$\frac{I}{A} = \frac{LV}{ARL} \quad \text{..... (1.12)}$$

We identify the above quantities as current density

$$J = \frac{I}{A} \quad \text{..... (1.13)}$$

electrical conductivity

$$\sigma = \frac{L}{RA} \quad \text{..... (1.14)}$$

and electric field

$$E = \frac{V}{L} \quad \text{..... (1.15)}$$

Then,

$$J = \sigma E \quad \text{..... (1.16)}$$

which is Ohm's law in a general form. Since we aim to find the expression for the electrical conductivity. We use the above equation in the following form

$$\sigma = J/E \quad \text{..... (1.17)}$$

Substituting the definition of J back in the above equation, we get

$$\sigma = I/AE \quad \text{..... (1.18)}$$

Now, we need to find the expression for current I in the conductor. Let n be the number of electrons per unit volume of the conductor and "v_d" be the drift velocity of electrons with charge "e". Then, the number of electrons crossing any

cross-section per unit time is "n (v_dA)". Therefore, the current passing through any cross-section of the conductor is given by

$$I = nev_dA \quad \text{..... (1.19)}$$

Plugging this expression into that of conductivity, we get

$$\sigma = nev_dA /AE \quad \text{..... (1.20)}$$

$$\sigma = nev_d/ E \quad \text{..... (1.21)}$$

Using the equation of drift velocity (1.22)

$$v_d = eE\tau/ me \quad \text{..... (1.22)}$$

in the above equation, we have

$$\sigma = ne\ eE\tau /Eme \quad \text{..... (1.23)}$$

$$\sigma = ne^2\ \tau/ me \quad \text{..... (1.24)}$$

This is the expression of electrical conductivity.

1.3.1 Effect of Impurity and Temperature on Electrical Resistivity of Metals

We know that the electrical conductivity of a metal is given by

$$\sigma = ne^2\ \tau /me \quad \text{..... (1.25)}$$

We write τ in terms of thermal velocity v_{th} and mean free path λ

$$\tau = \lambda /v_{th} \quad \text{. . . . . (1.26)}$$

Substituting for

$$v_{th} = \sqrt{\frac{3kT}{m_e}} \quad \text{.....(1.27)}$$

we get

$$\tau = \sqrt{\frac{3kT}{m_e}} = \lambda \sqrt{\frac{m_e}{3kT}} \quad \text{..... (1.28)}$$

Plugging τ into the expression for conductivity, we get

$$\sigma = ne^2 /m_e\ \lambda \sqrt{\frac{m_e}{3kT}} \quad \text{..... (1.29)}$$

$$\sigma = ne^2\lambda/ \sqrt{3mekT} \quad \text{..... (1.30)}$$

Hence, resistivity is given by

$$\rho = \sqrt{3mekT}/ ne^2\lambda \quad \text{..... (1.31)}$$

According to this equation, a metal's resistivity must be directly proportional to the temperature under square root. Metals resistivity is a result of electron scattering during the conduction process. Scattering of electrons occurs for two reasons: one is caused by collisions of conduction electrons with vibrating lattice ions, and the other is due to electron scattering by impurities in metal. The resistivity due to electron scattering by lattice vibrations known as phonon is denoted by p. This increases as the temperature rises. It exists even in pure conductors and is thus referred to as ideal resistivity. Whereas the resistivity of metals caused by electron scattering with impurities is denoted by "I". This is temperature independent and present even at absolute zero and is thus referred to as residual resistivity. As a result, the total resistivity of metal can be expressed as the sum of the two resistivities. This is known as Mathieson's rule.

Mathematically,

$$\rho = \rho_p + \rho_i \quad \text{..... (1.32)}$$

Since

$$\rho = me/ ne^2\tau \quad \text{..... (1.33)}$$

We can rewrite the above equation in the following form

$$\rho = m_e /ne^2\tau p + m_e ne^2\tau \quad \text{..... (1.34)}$$

Where τ_p and τ_i are the mean collision times of electrons with phonons and impurities respectively. At lower temperatures, ρ_p tends zero as the amplitude of lattice vibrations becomes small which essentially means that all the resistivity will be due to impurities i.e.

$$\rho = \rho i \quad \text{..... (1.35)}$$

1.4 Thermal Conductivity

The rate at which heat is transferred through a material is known as its thermal conductivity. It is possible to transfer heat using both charge carriers and crystal lattice vibrations (phonon). The summation of both phonon and charge carriers derives the total amount of thermal conductivity.

$$\kappa = \kappa_e + \kappa_{ph} \quad \text{(1.36)}$$

The electronic component of thermal conductivity is more important in metals than the phonon component. A law called the Wiedemann-Franz law [16] says that

the thermal to electrical conductivity ratio for all metals at a given temperature is the same.

$$\kappa_e = L\sigma T \quad \text{..... (1.37)}$$

Where L is Lorentz number ($L=2.45\times10^{-8}$ $w\Omega K^{-2}$). Knowing the relationship between the electrical conductivity and electronic contribution of thermal conductivity, one can rewrite the figure-of-merit as:

$$ZT=\frac{S^2}{L(1+\frac{K_e}{K_{ph}})} \quad \text{..... (1.38)}$$

1.5 Power Factor

With the help of power factor (PF), we can determine the success of a thermoelectric cooler (TEC) or generator (TEG). It is calculated by multiplying the Seebeck coefficient square by electrical conductivity at specific temperature. Mathematically, it can be expressed as follows:

$$PF = S^2\sigma \quad \text{..... (1.39)}$$

In the equation above, The power factor is represented by the letter PF, the Seebeck coefficient by the letter S, and the electrical conductivity by the letter σ.

1.6 Thermoelectric Figure-of-Merit

A thermoelectric material with high efficiency is required to have a low thermal conductivity in addition to having a high electrical conductivity. With regard to these circumstances. It will have a high "ZT" (K^{-1}) figure of merit and a very high "S-squared" power factor (PF). In thermoelectric "ZT," the relationship between electrical and thermal conductivity can be expressed as

$$ZT = \frac{S^2\sigma T}{\kappa}[K^{-1}] \quad \text{..... (1.40)}$$

This equation (1.40) shows that "S" stands for "coefficient of Seebeck". In this equation, "σ" stands for "electrical conductivity", "T" stands for "temperature", and "κ" stands for "whole thermal conductivity". It is equivalent to electrons and phonons conductivity ($\kappa = \kappa_{ph} + \kappa_e$) together. A dimensionless "ZT" can be written as,

$$ZT = T \times \frac{S^2\sigma}{\kappa} \quad \text{..... (1.41)}$$

The thermoelectric material of power factor (PF) is "$S^2\sigma$" as shown in the equation.

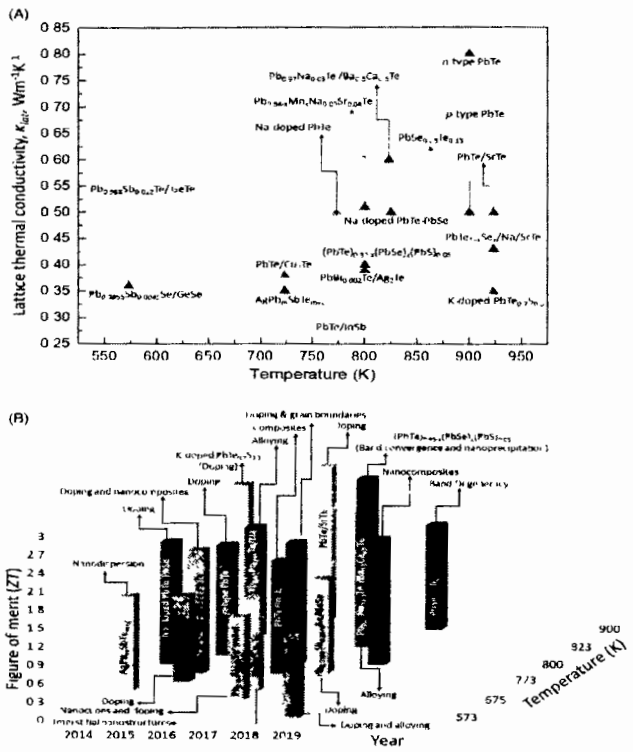

Figure 1.4: (A) Miscellaneous PbTe alloys with its ultra-low κ_{lat} value at divergent temperature range. (B) Enhanced ZT values of best performing PbTe alloys using miscellaneous optimization techniques [17, 18, 19, 20-35].

The "thermoelectric figure of merit" is primarily dependent on the PF. Power factor (PF) affects thermoelectric efficiency, so a reasonable thermoelectric efficiency is achieved by having a high power factor. The following equation can be used to obtain a relationship for a thermoelectric unit that is composed of both p and n-type semiconductors:

$$ZT = T \times \frac{(S_p - S_n)^2}{\left(\sqrt{\frac{\kappa_n}{\sigma_n}} + \sqrt{\frac{\kappa_p}{\sigma_p}}\right)^2} \quad \ldots\ldots\ldots\ldots\ldots\ldots\ldots\ldots\ldots\ldots\ldots\ldots (1.42)$$

In the above, $\sigma_p, S_p, and\ \kappa_p$ represent the electrical conductivity, Seebeck effect, and thermal conductivity of p-kind thermos-electric semiconductors respectively, while σ_n, $S_n, and\ \kappa_n$ represent the electrical conductivity, Seebeck effect, and thermal conductivity of n-kind thermos-electric semiconductors. "ZT" is a thermoelectric figure of merit, and it has a direct relationship to the coefficient of performance (ϕ), efficiency (η), and power generation.

$$\eta = \frac{W}{Q_H} = \frac{T_H - T_C}{T_H} \times \frac{\sqrt{1+ZT}-1}{\sqrt{1+ZT}+\frac{T_C}{T_H}} \quad \text{.....(1.43)}$$

$$\phi = \frac{Q_C}{W} = \left(\frac{T}{T_H - T_C} \times \frac{\sqrt{1+ZT}-1}{\sqrt{1+ZT}+1}\right) - \frac{1}{2} \quad \text{.....(1.44)}$$

The efficiency of power generation (η) is equivalent to the proportion of produced electrical power (W) to thermal power (Q_H) provided, despite the fact that the coefficient of performance (ϕ) is equivalent to refrigeration (Q_c) rate divided by providing electrical power (W). The overhead equation has two key terms: $\frac{T_H - T_C}{T_H}$ (Carnot efficiency) and $\frac{\sqrt{1+ZT}-1}{\sqrt{1+ZT}+\frac{T_C}{T_H}}$ (thermoelectric figure of merit), where "ZT" stands for "thermoelectric figure of merit".

If the values of "ZT" increase, the efficiency of thermoelectric increases as well. When the values of "ZT" are reached to infinity state, demonstrates the maximum efficiency of thermoelectric, which is the equivalent to the Carnot efficiency. The high electrical conductivity (σ) and Seebeck effect (S) have [36] to achieve a high "ZT," while the thermal conductivity (κ) must be low, as can be seen from the "ZT" formula.

1.7 Optimization of Thermoelectric Performance

As shown in equation 1.41 a TE material with a higher value of ZT requires a high power factor and a lower thermal conductivity. However, in case of bulk materials "S" are connected in this way that no one can be optimized separately to meet the conditions for increasing ZT. The crystal structure, the electronic structure of the material, and the concentration of carriers all have an impact on the properties "κ" and "S" [37, 38]. There have been many materials studied in the past to find a good Thermo-electric material that met the above criteria.

Insulators, metals, and semiconductors are the types of most materials depending on the electronic structure and carrier concentration. At 300 K, the thermoelectric properties of insulators, metals, or semiconductors are summarized in Table 1.1 and plotted in Fig. 1.5.

Table 1.1 Comparison of thermoelectric properties of metals, semiconductors, and insulators at 300 K [39]

Property	Metals	Semiconductor	Insulators
S, (μVK^{-1})	~ 5	~ 200	~ 1000
σ, ($\Omega^{-1}cm^{-1}$)	~ 10^{6}	~ 10^{3}	~ 10^{-12}
Z, (K^{-1})	~ 3×10^{-6}	~ 2×10^{-3}	~ 5×10^{-17}

As shown in Table 1.1, semiconductors have the best thermoelectric properties of all bulk materials having a maximum value of Z is ~2 × 10^{-3} K^{-1}. Several types of thermoelectric materials have high power factors and are found in the narrow band gap semiconductor region (fig 1.5) with a carrier concentration of around 1 × 10^{-19} cm^{-3}. As previously stated, Slack [40] believes that a narrow band gap semiconductor with a high mobility career is the most promising candidate for a good TE material. Later, as previously stated by Slack [41, 42] Mahan stated that the characteristic of an excellent thermoelectric (TE) material is that it is characterized by a narrow band gap semiconductor (e.g. 0.25 eV at 300 K). As the best available bulk TE material, semiconductors ($Z=\sim2\times10^{-3}$) have a limited application range. Those materials' TE efficiency was previously improved.

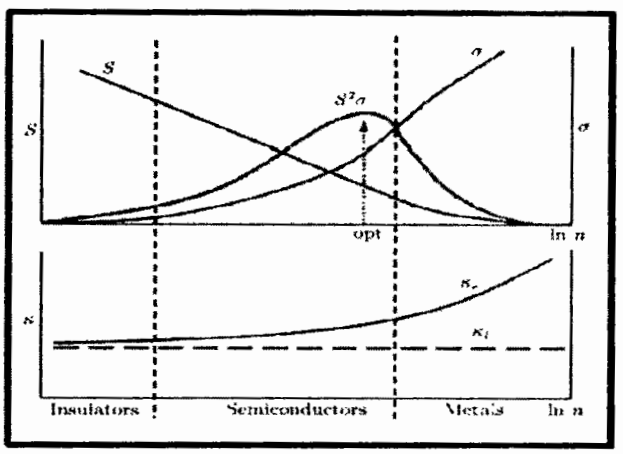

Figure 1.5: Seebeck coefficient (S), electrical conductivity (σ), power factor ($S^2\sigma$), and electronic (κ_e) and lattice (κ_l) thermal conductivity as a function of free-charge-carrier concentration n, the optimal carrier concentration is about 1×10^{19} cm^{-3}, which is indicated by an arrow [38,39].

1.8 Research Progress in the Field of Thermoelectric

Thermoelectric research has come a long way in the last few decades in general. Traditional thermoelectric material's performance has been greatly enhanced as a result of theoretical advances and new synthesis methods. On top of that new and improved thermoelectric material has been investigated as well as their applications. Among the earliest applications of the TE effect were metallic thermo-couples, which have been in use for many years to measure temperature [43]. There is a big challenge in reducing the thermal conductivity below the alloy limit [44]. The family of $Bi_{2\,(1-x)}$ Sb_{2x} $Te_{3\,(1-y)}$ $Se_{3}y$ having ZT value 1 with a room temperature for $Bi_{0\,5}Sb_{1\,5}Te_{3}$ exhibits the highest thermos-electric efficiency in all bulk thermos-electric material. Although there are many complex materials such as skutterudite [45–46], clathrates [47–48], and other zintls compounds [49]. They have been studied in order to obtain ZT values ranging from 1 to 15 as prospective PGEC materials. It is still very far from being realized that a perfect PGEC material will be realized at any point in the future. A few years later, the structures such as nano-tubes and nano-wires [50, 51] two-dimensional super lattices such as GaAs/ AlAs/ ErAs [52, 53] and Si/Si -Ge [54, 55] super lattices and three-dimensional super lattices were applied thermal conductivity reduction method.

The increase in publication indicates a surge in research interests in thermoelectric materials following the development of various processing techniques such as nano-structuring for TE materials, which enabled the TE materials ZT to be increased.

As shown in Fig.1.6, a graph shows the published papers on various thermos-electric materials in the last five years (2014-2018). The thermoelectric materials Bi_2Te_3 alloy and "Pb" chalcogenides still get a lot of attention from scientists. Skutterudite, on the other hand, has a lot of potential because of its high power factor. A type of burger-like thermo-electric material such as "Sn" chalcogenides also have a lot of research potential.

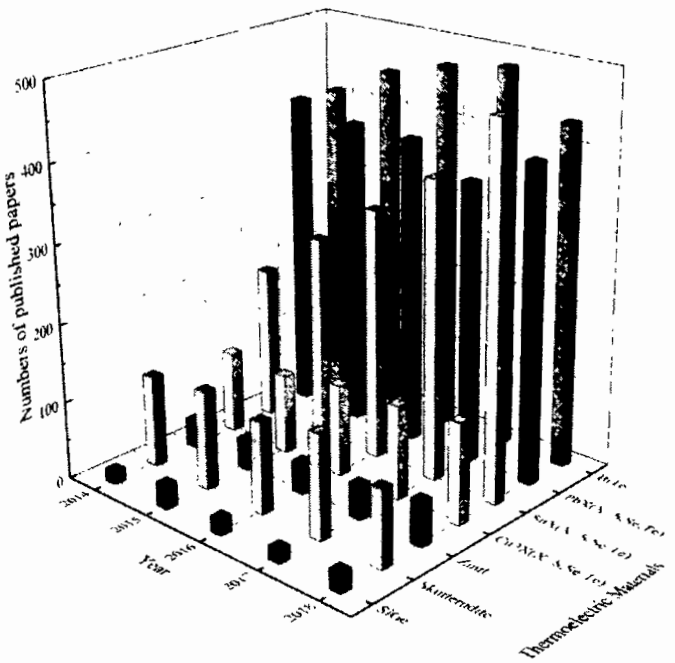

Figure.1.6: Number of published papers on some typical thermoelectric materials in recent 5 years (2014-2018), data are extracted from the web of science core collection.

1.9 Research Projects and Research Goals

In order to meet the demand for increased energy, we will need a wide range of clean and renewable energy sources for the world's population by 2050. In spite of the fact that there are periods of time when the sun does not shine and that usable sunlight is distributed unevenly across the globe. Solar energy is widely regarded as the most favorable alternative energy source. Thermal electricity is a viable renewable source of power from wasted heat but its widespread use is still in its infancy. The difference in temperature between the hot outside and cool inside environment is used to generate thermal electricity by embedding nano-fabricated pellets of thermoelectric nano-materials inside window glasses. Potentially usable power could be generated from 9 m^2 of window area at 206 ^0C temperatures for the first time in this work. Natural temperature gradients may serve as an energy source for green construction when they exist.

A new way to get energy from the sun is shown that uses a thermoelectric with a material that shows a lot of strain because of stress-induced electric field and phase change. The coefficient of thermal expansion of a material that undergoes such a phase shift increases dramatically over a small temperature range (usually several degrees Kelvin).

The thermally induced strain is changed to an electric field when a material is organized in a geometric configuration, such as a laminate having stress induced electric field (e.g. a piezo-electric material).

1.10. Applications of Thermal electricity

After neglecting thermal and electrical contact resistances, Ioffee theoretically [56] derived the correlation between the efficiency and figure of merit for the generation of thermoelectric power or performance coefficient for thermoelectric cooling. As a result, efforts to find new thermoelectric materials must focus on increasing the figure of merit, which is the primary determinant of the efficiency of material. Fig. 1.7 (a) shows the generation of Thermoelectric power by using the following devices as the Seebeck effect and to cool TE using the Peltier effect, use thermocouples made of p-type and n-type thermos elements. Charge carriers (n-type and p-type thermos-elements) are used for the power generation when they tend to penetrate from the hot to cold side (Fig. 1.7(a)) and also in the direction of the applied voltage in case of cooling (Fig. 1.7(b)).

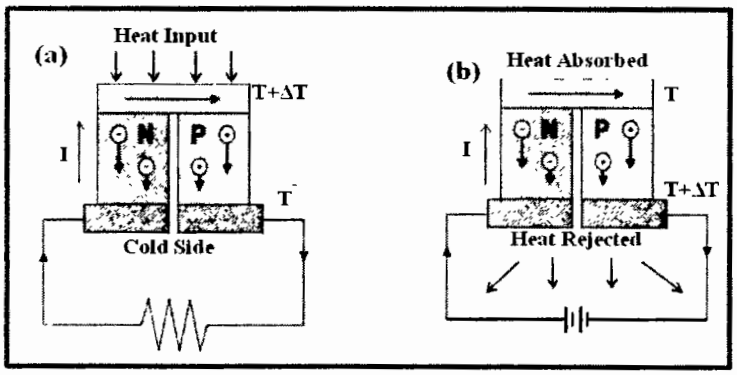

Figure 1.7: Thermoelectric devices for a) power generation and b) cooling.

1.10.1. Thermoelectric Cooling

Fig 1.7 (b) shows how a thermocouple works, applying an electric current to a thermocouple to pump heat from one end to the other. So long as the hot side is cooled, quickly down the cold junction to ambient temperatures.

To calculate the thermoelectric cooler's performance coefficient (COP), take the cooling capacity Q_c and divide it by the total power consumption P [57].

$$\Phi=\frac{Q_c}{P} \quad \text{..... (1.45)}$$

The maximum COP is given by the following equation

$$\Phi_c = \frac{T_c(\alpha+1)-\Delta T}{\Delta T(\alpha+1)} \quad \text{(1.46)}$$

Where

$$\alpha=(1+ZT)^{\frac{1}{2}} \quad \text{(1.47)}$$

the average temperature of the hot and cold joints is T. The performance of a thermoelectric cooler depends on the figures of merit of the thermocouple materials

Consumer products such as refrigerators and wine chillers can withstand temperatures as low as 0 °C on a macro scale. Thermoelectric cooling devices are important in applications requiring small size and quiet operation despite having lower cooling performance than conventional refrigerators [58]. When AC power is not available, it can also be used with DC power. It is also possible to use thermoelectric modules to cool electronics with a variety of different performance parameters. Temperature control using thermoelectric cooling is less efficient at the macro-scale but it is becoming more popular at the micro-scale due to its maintenance-free operation and small size, which makes it attractive.

1.10.2. Thermoelectric Power Generation

Thermoelectric generators use the Seebeck effect to turn heat into electricity. In Fig. 1.7 you can see the basic operation in action (a). Thermocouples are interconnected in form of parallel and series in the thermoelectric devices respectively. The thermocouples prevent heat from escaping from one side of the couple to the other. Open circuit voltage of the generator is proportional to the Seebeck coefficients of n and p-type legs, the temperature gradient between the cold and hot junctions (ΔT), and the number of thermocouples.

With a load resistance R_L, the generator's Seebeck voltage generates an electrical current. The generator's output power is calculated as follows:

$$\Phi_H=\frac{P}{Qc} \quad \text{(1.48)}$$

The figure of merit of thermocouple materials temperatures of both sides such as hot and cold the generator load resistance all affect power generation efficiency. according to equation (1.49).

$$P=\frac{V^2}{R_L}=\frac{N^2(\alpha_p-\alpha_n)^2\Delta T^2}{R_L} \quad \text{(1.49)}$$

In addition to cooling, a system for determining the generation of power was also developed for train carriages [59].

$$\Phi_H = \frac{\Delta T(\alpha-1)}{T_H(\alpha+1)-\Delta T} \quad \text{.....(1.50)}$$

Equation 1.50 shows that power generation efficiency depends on the thermocouple materials figure of merit, the temperatures of the hot and cold sides, and the generator load resistance.

A system likewise advanced for train carriages which were used for the determination of making power besides cooling [59].

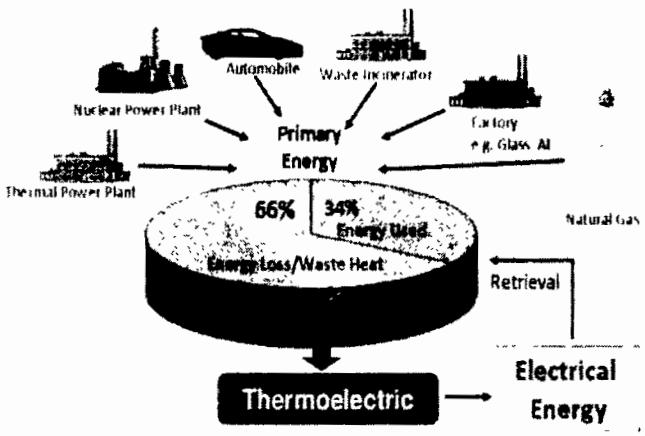

Figure 1.8: Applications of Thermoelectric Materials [59].

Military forces as well as firefighters used this light thermal uniform after its completion on their approach to producing electrical power from the body heat of human beings while dong their services [60]. Minor mobile thermoelectric coolers (TECs) are commercialized then it is likely to substitute air conditioners besides refrigerators through thermoelectric coolers (TECs) to switch the ozone reduction because of refrigerant gases [61]. The solar-based thermoelectric generators (TEGs) can be developed in remote areas. These solar types of thermal energy (STE) convert solar energy into electrical power [62]. Nowadays, It has an important function in atmosphere protection. These thermal electrical generators (TEGs) are also utilized to consume wide-open in the workshop of automobiles [63] with gas turbines to convert waste thermal energy into useful electrical energy [64,60]. Likely, minor electric applications such as mobile phones, wristwatches, and Laptops are where these

generators are used [61]. Yet, it is not commercialized due to reason of low power factor and high price with gives low efficiency of the device and a low thermoelectric figure of merit.

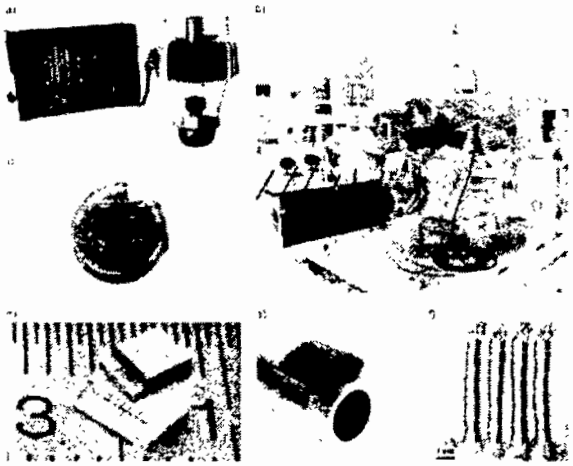

Figure. 1.9: a) Oil-burning lamp powering a radio using one of the first commercial thermoelectric generators, made of ZnSb/constantan thermocouples. Built-in USSR at the beginning of 1948. Reproduced and adapted from [65]. b) New Horizons in the assembly hall. The black RTG is visible on the left side of the satellite. c) Cardiac peacemaker Medtronic Laurens-Alcatel Model 9000, incorporating a small bar of 238 Pu as the heat source. Reproduced and adapted from [66]. d) Micro thermoelectric generators from Micro pelt. Reproduced and adapted with permission from Micro pelt. e) Concept of an organic-based generator design suitable for round surfaces. Reproduced and adapted with permission from Otego GmbH. f) In-plane embroidered textile thermoelectric device with 4 n/p elements, comprised of *n*-type coated PET yarns (11 yarns per leg), *p*-type dyed silk yarns (2 yarns per leg), and silver paste for contacts [67] with an appreciable diminution of the power output of only a few percentage points over a period of decades.

1.11. Thermoelectric Materials

1.11.1. Bulk Thermoelectric Materials

For macro-level purposes, bulk thermoelectric materials have shown to be effective. Introducing bulk materials into electronics may be done in two ways. One way is to prepare each element separately before aligning and bonding them to the device framework. The second way is to combine the large pieces of TE material and cut away the excess material. Fig.1.10 depicts the figure of merit for a variety of common materials across wide temperature ranges.

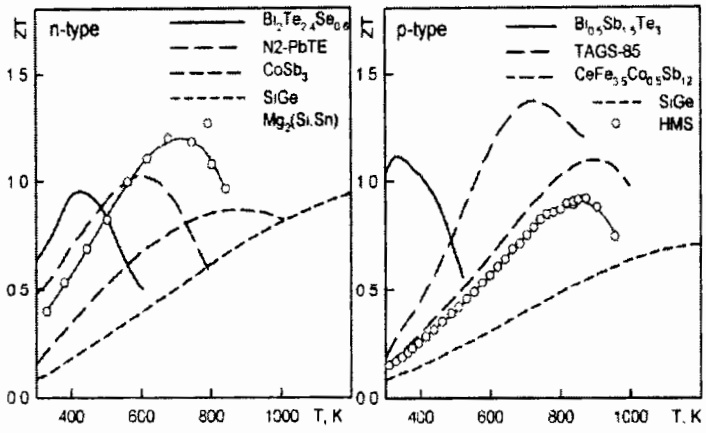

Figure 1.10: The thermoelectric Figure of merit of the best representatives of silicate thermoelectric in comparison with the other thermoelectric, having the highest ZT in their temperature range [68]

1.11.1.1. Silicon

One of the most commonly used thermoelectric materials is SiGe alloy which can operate at high temperatures (up to 1275 K). It has been used for space exploration. Its structure has a face-centred cubic lattice and crystallizes in the Fd3m space group. Ge and Si can coexist in a continuous solid state [70].

Yu et al. [71] achieved a value of 1.3 ZT in $Si_{95}Ge_5$ by modulation doping via nano-composites containing nano $Si_{70}Ge_{30}P_3$ particles, as illustrated in Fig. 1.11 (a) in 2012. Due to modulation-doping, the carrier mobility was improved while keeping the nano-particles low thermal conductivity. As shown in Fig. 1.11(b), a ZT-T plot summarized some outstanding SiGe alloys. It appears plausible that n-type SiGe alloys possess superior ZT to p-type forms.

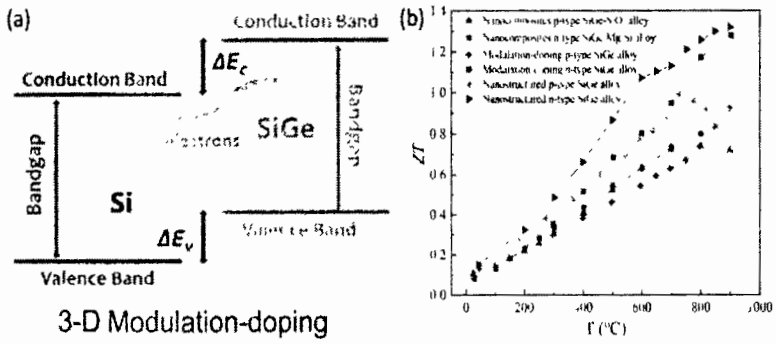

Figure. 1.11: (a) Band alignment of strained Si on SiGe [71]. (b)Temperature dependence of ZT for some excellent SiGe alloys [71-76].

1.11.1.2. Lead Chalcogenides

At 800 K, Hsu et al. [77] found a 2.2 value of the thermoelectric figure of merit for the $AgPb_mSbTe_{m+2}$ system which was considered to be excellent. Fig. 1.9 depicts the variation of the ZT of $AgPb_{18}SbTe_{20}$ with temperature, which reveals 2.2 is the ZT_{max} value at 800K.

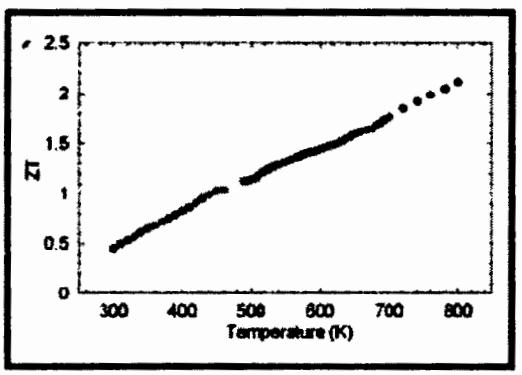

Figure 1.12: Thermoelectric figure of merit of $AgPb_{18}SbTe_{20}$ as a function of temperature [77].

Also, Heremans et al. [78] found that distorting the electronic density of the state increased the Seebeck coefficient of PbTe. At 773K p-type PbTe obtained greater than 1.5 value of thermoelectric figure of merit. This is obtained by creating the impurity in PbTe with the help of thallium.

1.11.1.3. Skutterudites

Composing structure of eight corners shared octahedrons $CoSb_6$ creating a large space at cubic lattice center linked with other octahedrons as shown in fig. 1.13(a) [79, 80]. It is common for some metal atoms to be filled into the void. These can vibrate to increase the photons scattering. Additionally, electron transport properties of material can enhance with the doping effect process which is caused by the filling atoms significantly.

Rare-earth metals [81,82], alkaline-earth metals [83,84], and other metals [85,86] were filled into $CoSb_3$ with the majority of them containing heavy elements. Pei et al. [87] reported in 2009 that Na-filled $CoSb_3$ had a high PF and good mobility. Following that, Zhang et al. [88, 89] synthesize Li-filled $CoSb_3$ under high pressure. Previously, it was impossible to do using conventional synthesis methods at ambient pressure. Zhao et al. [90] were able to control both electron transport and phonon by

putting soft magnetic nano-particles Co into the $Ba_{0.3}In_{0.3}Co_4Sb_{12}$ matrix in 2017. scattered electron causes the super paramagnetic fluctuation is multiplying in nano-Compounds as shown in Fig 1.13 (b).

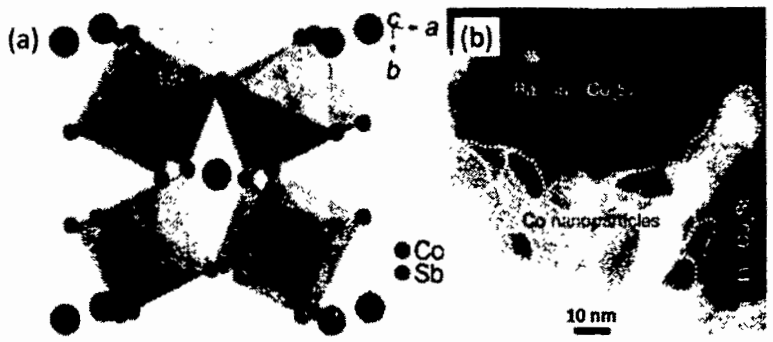

Figure. 1.13: (a) Crystal structure of $CoSb_3$ (b) HRTEM image indicating Co nano-particles distributed randomly at the interfaces and boundaries of the matrix [79,90].

1.11.1.4. Bismuth-Antimony Alloys

Using bismuth telluride as a test material, Goldsmith demonstrated excellent thermoelectric properties in 1954 [91]. These properties were attributed primarily to the high mean molecular mass, low melting temperature, and partial degeneracy of the conduction and valence bands of this V-VI chalcogenide's conduction band.

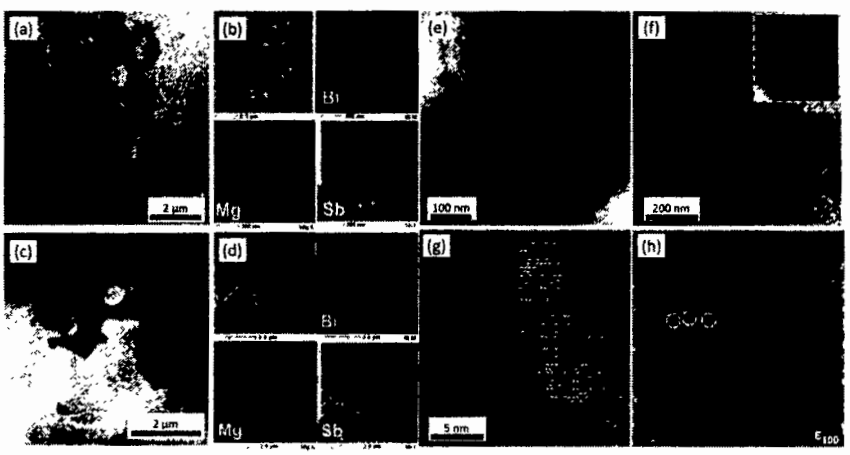

Figure.1.14: The HADDF-STEM and EDS-Mapping images of $Mg_3Sb_{1.5}Bi_{0.5}$ (Mg-poor) sample ((a) and (b)) and $Mg_{3.2}Sb_{1.5}Bi_{0.5}$ (Mg-rich) sample ((c) and (d)). (e)-(h) Microstructure of $Mg_{3.15}Mn_{0.05}Sb_{1.5}Bi_{0.49}Te_{0.01}$ sample indicating sub-micron grains, grain boundary, Bi-rich precipitates and strain-region [91, 92].

1.11.1.5. Bismuth Telluride

The commercialized thermoelectric refrigeration material Bi_2Te_3 was first investigated as a thermoelectric candidate in 1954. It crystallizes in a layered structure (Fig. 1.15) with space group $R\bar{3}m$.[15] The hexagonal unit cell dimensions at room temperature are a = 3.8 Å and c = 30.5 Å. The atomic layers stacked along the c-axis form the sequence Te [1]–Bi–Te [2]–Bi–Te[1]. The tellurium and bismuth layers are connected by strong ionic-covalent bonds whereas the bonding between neighboring Te layers is based on weak van der Waals-type forces [93].

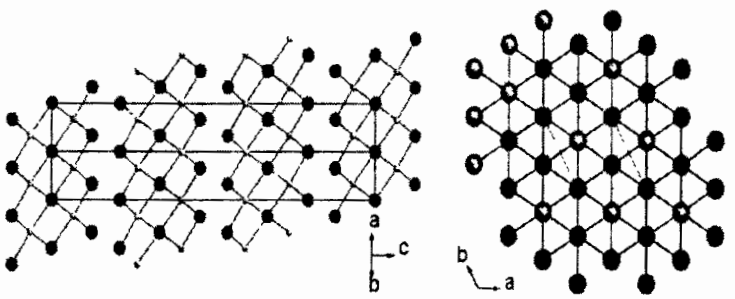

Figure 1.15: Crystal structure of Bi_2Te_3 Bi: cyan, Te: red [93]

1.11.1.6. Antimony Telluride

Using bulk p-type nanocrystalline BiSbTe alloy at 373 K Poudel et al. [94] found a peat value of ZT is 1.4 in 2008. Ball milling p-type BiSbTe alloy ingots yielded the Nano powders which were then consolidated by hot pressing. Fig. 1.16(b-e) shows an abundance of nanodots, nanograins, and nanostructures, that scatter phonons strongly. Because of this, the bipolar effect was reduced by the existing interfacial potential. The concentration of carriers in p-type materials increased as the amount of nano SiC increased. Fig. 1.16(f) shows that the nano inclusions of SiC also served as scattering lower energy carriers, and effective energy filters and increased the Seebeck coefficient [95]. $Bi_{0.5}Sb_{1.5}Te_3$ having the 1.86 value of ZT was reported in 2015 by Kim et al. [96] using melt spinning-spark plasma sintering and excessive Te was used as a reaction raw material when it was melted and expelled during spark plasma sintering, dense dislocation arrays were left at low-energy grain boundaries. The dense dislocation arrays effectively scattering the mid-frequency phonons led to a substantially lower lattice thermal conductivity (Fig. 1.16(g and h)).

In 2019, Kim et al. [97] introduced nanodiamonds into polycrystalline BiSbTe alloys, forming clustered zones of point defects (Fig. 1.16(i)) and generating a local strain field that intensified the point defects.

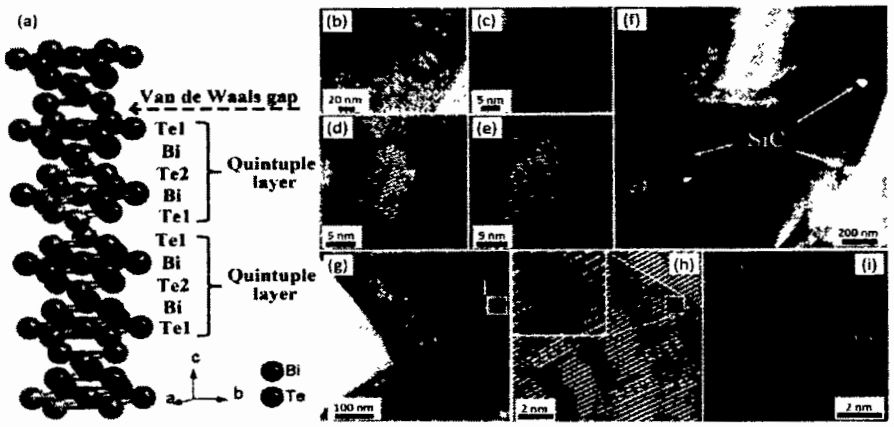

Figure. 1.16: (a) Crystal structure of Bi_2Te_3 compound. (b – e) Microstructure of $Bi_2(Sb, Te)_3$ materials showing nano-grains, nano-size grain boundaries, and nano-dots. (f) Nano-SiC grains in$Bi_2(Sb, Te)_3$ materials. (g) Grain boundaries dislocation and (h) dense dislocation arrays in $Bi_2(Sb, Te)_3$ materials prepared with excess Te. (i) The interface between nano-diamond and $Bi_2(Sb, Te)_3$ is indicated by a red-dotted line wherein strain remained around [94-98].

1.11.1.7. (Bi, Sb)Te-based Ternary Alloys

Several samples had ZT values in the vicinity of unity which was extremely high. Additionally, alloying, in addition to creating vacancies is an increasingly popular method of maximizing thermal energy conversion efficiency [99,100]. Substitutions of "Sn" and "Pb" in the materials are predicted to induce extrinsic p-type carriers because "Sn" and "Pb" have one fewer valence electrons than Sb and Bi. Additionally, the disorder caused by random atomic substitution may introduce strain and mass fluctuations into the material, scattering phonons and lowering thermal conductivity [101].

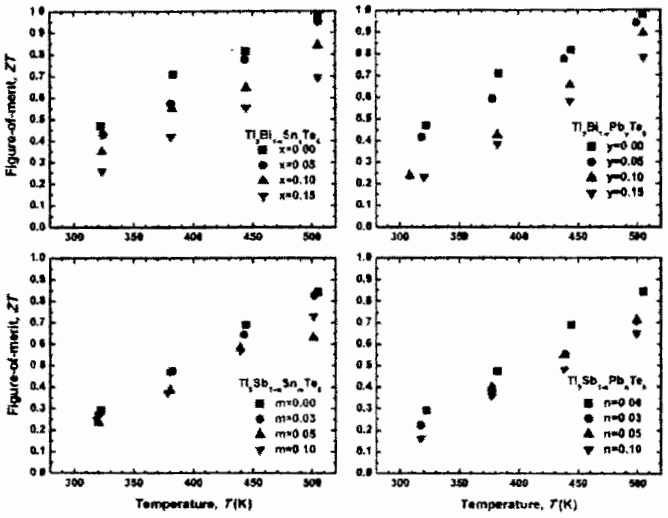

Figure 1.17: Thermoelectric figure-of-merit ZT of Tl_9Bi_1 [88].

1.12. Literature Review

The "$TlSbTe_2$" was stirred up by K. Kurosaki et al. [102] using a hot press technique and after the formation of compound, they examined that as related to Sintered Bi_2Te_3 and TAGS "$(GeTe)_{1-x}(AgSbTe_2)_x$" materials, the thermal conductivity and electrical resistivity of the stirrup material was variate correspondingly. At 666 K, the Seebeck coefficient of the material was 224 μvk^{-1}. Seebeck coefficient for the material in the total range of temperature was positive (S+) which demonstrates the performance of the P-type. The current thermoelectric devices have a power factor of about $10^{-3}\ Wm^{-1}k^{-2}$, but at 576 K they found the "PF" for their material of about $8.9 \times 10^{-4}\ Wm^{-1}k^{-2}$. In comparison to current devices, this was low. Also at 715 K, they found a "ZT" rank of 0.87 for the material.

A unique low-valent $Tl_6Si_2Te_6$ was synthesized and compared to $Tl_6Ge_2Te_6$ by Assoud et al. [103]. Crystals, electronic structures, and their electronic possessions were all equated. They noticed that their substance and the other had similar crystal structures. The measurable outcomes for their material are $a = 9.4325(6)Å$, $b = 9.6606(7)Å$, $c = 10.3889\ (7)Å$, $\alpha = 89.152(2)°$; $\beta = 96.544\ (2)°$; $\gamma = 100.685\ (2)°$; $V = 923.3(1)Å^{-1}$ $(Z = 2)$. Because of Si-Si single bond, The crystal structure of the dimeric $[Si_6Te_6]^{2-}$ units were tracked due to the Si-Si single bond. The bond between Tl and Tl is weak by nature and it is irregularly coordinated by 5 or 6 atoms of "Te.". For other compounds, notify dark color with a small band gap of rank 0.5 ev and 0.9 ev for $Tl_6Ge_2Te_6$ and $Tl_6Si_2Te_6$, respectively. At temperature 300

K, they examined Seebeck coefficient and electrical conductivity of their prepared material electrical conductivity is $+65\ \mu v K^{-1} K$ and $5.5\ \Omega^{-1} cm^{-1}$.

Kurosaki *et al.* [104] fixed Ag_9TlTe_5 models of polycrystalline. They have used the concentration of "x" as Ag_9TlTe_x where ($X = 5.0, 5.05, 5.1, 5.2, 5.3, 5.5, 5.7$ *and* 6.0) . By heating of Ag_2Te, Tl_2Te, Tl_2Te_{12} plus "Te" they made the samples of Ag_9TlTe_x. They used quartz tube which was closed and then with an appropriate quantity for the creation of needed samples the ball-milling plus hot-press procedures were used. The phase relationship was examined using the X-Ray Diffraction (XRD) method. Except for Ag_9TlTe_{50} sample, the calculated electrical resistivity was decreased through increase in temperature. They examined Seebeck coefficient is just about autonomous of temperature aside from Ag_9TlTe_{50}, PF is the high rank of 0.3 to $0.4 \times 10^{-3}\ Wm^{-1}K^{-2}$ while low of the order of $0.05 \times 10^{-3}\ Wm^{-1}K^{-2}$ For Ag_9TlTe_{50} He found that the dimensionless thermoelectric figure of merit is quite low such as 0.08, whereas the $X \geq 5.0$ value is approximately high which is 1, which demonstrated that by altering "Te" content in Ag_9TlTe_x, altering entirely physical possessions.

Using the knowledge of the electronic density of states in "PbTe", Joseph P. Heremans *et al.* [105] raise "ZT". They improved the Seebeck Coefficient by altering the electronic density of states which principles to double the "ZT" and they went on to say that it may provide better results in nanostructured materials.

Tl_4MTe_4 was created by H. Kleinke *et al.* [106] where "M" is indicated by "Zr" and "Hf". They examined the structure of their thermoelectric plus crystal system. They employed XRD to investigate crystal structure. They establish that Tl_4MTe_4 has an octahedral crystal structure with the space group $R\bar{3}$. Tl_4ZrTe_4 has unit cell dimensions of $a = 14.6000(5)Å$ and $c = 14.189(1)Å$ whereas Tl_4HfTe_4 has a unit cell dimension of $a = 14.594(1)Å$ and $c = 14.142(3)Å$. They employed the LMTO method such as linear muffin-tin orbital to calculate the electric structure. The indirect band gap of Tl_4MTe_4 is 0.3 eV, demonstrating semiconducting capability. They discovered that when the temperature rose, the thermal conductivity increased whereas the electrical resistivity and Seebeck Coefficient reduced. The "ZT" of the compound Tl_4ZrTe_4 rose from 0.14 to 0.1 while the temperature was between 370K and 420 K but when the temperature was above 420 K the compound "ZT" decreased.

From another point of view, the temperature between 370 K to 540 K, the figure of merit (ZT) varies from 0.05 to 0.09 for the Tl_4HfTe_4 compound.

In additional work, Tl_2ZrTe_3 was developed by H. Kleinke *et al.* [107] which is ternary. For the inspection of different possessions for example structural, physical, and thermal properties were compared with Tl_2SnTe_3. Tl_2ZrTe_3 is a cubic compound with lattice constants $a = 19.118(1)\text{Å}\ (Z = 36)$. They studied the electronic characteristics of Tl_2ZrTe_3, and the electronic properties indicated that it is semiconducting. Band gap of Tl_2ZrTe_3 (Eg=0.7 eV) is greater than that of Tl_2SnTe_3 (Eg=0.4 eV). From room temperature to 450 K, electrical conductivity changes inversely. When temperature is increased above 450 K, electrical conductivity decreases spontaneously, The electrical conductivity of Tl_2SnTe_3 decreases from $22\ \Omega^{-1}cm^{-1}$ to $15\ \Omega^{-1}cm^{-1}$ when temperature increases from room to 515 K. Thermal conductivity for Tl_2ZrTe_3 decreases from $0.39\ Wm^{-1}K^{-1}$ to $0.30\ Wm^{-1}K^{-1}$ from 373 K to 450 K, whereas thermal conductivity for Tl_2SnTe_3 reduces from $0.24\ Wm^{-1}K^{-1}$ at 420 K to $0.20\ Wm^{-1}K^{-1}$ at 450 K. Seebeck Coefficient is usually matching in rank of 373 K to 450 K for Tl_2ZrTe_3 counts but lowers with temperature more than 450K highest measured score of Seebeck coefficient is $120\ \mu VK^{-1}$. The Seebeck coefficient of Tl_2SnTe_3 increases from room temperature to 450 K from $240\ \mu VK^{-1}$ to $330\ \mu VK^{-1}$. Tl_2ZrTe_3 describes power factor fluctuation are almost identical, ranging from $0.35\ \mu Wcm^{-1}K^{-1}$ to $0.41\ \mu Wcm^{-1}K^{-1}$ .However, with Tl_2SnTe_2 "PF" is cumulative in tandem with temperature. The Thermoelectric Figure of merit (ZT) value of Tl_2ZrTe_3 is ranging from 0.18 at 450 K which is somewhat lower than the Tl_2SnTe_3 "ZT" value.

Bangarigadu-Sanasy et al. [108] discussed the thermoelectric properties of $TlGdQ_2$, where "Q" referred to "SE" and "TE," as well as the properties of Tl_9GdTe_6. $TlGdQ_2$ has an iso-structural relationship with $TlSbQ_2$, while Tl_9GdTe_6 has an iso-structural relationship with Tl_9BiTe_6. $TlGdQ_2$ has high Seebeck coefficient values but poor electrical conductivity values. $TlGdTe_2$ has a poor thermal conductivity which is 0.5 $Wm^{-1}K^{-1}$at room temperature which was investigated. At 550 K of Tl_9GdTe_6 sample because of high electrical conductivity, it is found that the power factor was the low value which is 850 $\Omega^{-1}cm^{-1}$whereas Seebeck coefficient has a low value27 μVK^{-1}. Throughout the study, it was figured out that at 500 K the thermoelectric

properties of $TlGdTe_2$ are good throughout the entire study, and figure of merit "ZT" was 0.5.

$Tl_{10-x}Ln_xTe_6$ is prepared by S. Bangarigadu-Sanasy et. al. [109]. Pr, Nd, CE, Sm, Gd, Tb, Dy, Ho, and Er were the elements Ln in the combination while "X" value ranged between 0.25 to 1.32. The samples were prepared through the Hot press procedure. During the study, $Tl_{10-x}Ln_xTe_6$ has iso-structural crystal construction to Tl_9BiTe_6. It was also studied that increases the Seebeck coefficient and volume of unit cells by raising the quantity of "Lanthanide" while decreasing the conductivities of electrical and thermal. $Tl_{8.97}Ce_{1.03(5)}$ Te_6, $Tl_{8.92}Pr_{1.08(8)}$ Te_6, and $Tl_{8.99}Sm_{1.01(7)}$ Te_6, all have higher electrical and thermal conductivity with a low Seebeck coefficient than Tl_9LnTe_6 compounds. This is due to the discontinuity in the band gap. On cold press pellets, the finest "ZT" value of 0.22 was achieved at 550 K in the stoichio metric compound on lanthanum content "x" increases in the $Tl_{9-x}Ln_xTe_6$ compound.

Kyung Tae Kim *et al.* [110] synthesized $Bi_{0.5}Sb_{1.5}Te_3$ matrix composites with alumina nano-particle-dispersion and also improve the properties of thermoelectric for composites. The ball milling procedure was used to prepare the nano-particles which were then followed by spark plasma sintering way. Through Ball milling technique, the Nanopowder of bismuth antimony telluride of p-type was prepared by the mechanical chemical method. Nano-particles of Al_2O_3 were added to the nanopowder at a rate of 1.0, 0.0, and 0.3 vol. per cent. They looked at the size of nano-particles using surface morphology analysis. As the same range of temperature rises from 293 K to 473 K, electrical resistivity increases from $1.5 \times 10^{-5}\ \Omega m$ to $2.5 \times 10^{-5}\ \Omega m$, while the Seebeck coefficient (S) increases from 205 μVK^{-1} to 210 μVK^{-1}, indicating the presence of P-type semiconducting conduct. The 0.3 vol.% Al_2O_3/BST Nano composite has the highest Seebeck coefficient (s) 235 μVK^{-1} at 373 K. They indicated that increasing the volume fraction of Al_2O_3 results in an increase in carrier density, which affects carrier mobility, electrical resistivity, and Seebeck coefficient of BST/Al_2O_3 Nanocomposites. At 393 K, 0.3 vol% Al_2O_3/BST Nanocomposites have 1.7 times the experiential power factor (PF) from actual BST, with 33 μWK^{-2} cm versus 22 μWK^{-2}cm for actual BST. The addition of Al_2O_3 Nanoparticles reduces the thermal conductivity having 0.8 $Wm^{-1}K^{-1}$ for actual BST and 0.7 $Wm^{-1}K^{-1}$ for Al_2O_3/BST. At 373 K, the figure of merit (ZT) is higher than actual BST which is 1.5 for 0.3 vol.% Al_2O_3/BST composite.

Thermoelectric properties of nano-structured indium-doped SnTe ($In_xSn_{x-1}Te$) were examined by Zhang et al. [111]. The hot press and Ball-milling methods were used to prepare the compound. They examined that the power factor (PF) and Seebeck coefficient (S) are increased while electrical conductivity, thermal conductivity, and diffusivity reduction whereas no change occurred practically in specific heat, a little rise in $In_xSn_{x-1}Te$ was observed at the 300 K to 900 K temperature range. They used ball mill method and the hand mill method to find their comparable result. The result was similar to what they had previously seen using other procedures. As the carrier concentration increases, they observe the correlation between carrier concentration and Seebeck effect demonstrating that "In" doped SnTe shows irregular behavior. They obtain the images of $In_xSn_{x-1}Te$ using SEM, TEM, and HRTEM techniques. These images identify that small and large grain boundaries, as well as a high degree of crystallinity of the sample, affect the thermal conductivity of the sample. At 873 K, observed thermal electric figure of merit for $In_{0.0025}Sn_{0.9975}Te$ was better than "1".

The thermoelectric properties of indium-doped $PbTe_{1-y}Sey$ alloys were studied by Bali et. al. [112] using solid-state method. They revealed that increasing temperature causes an increase in electrical resistivity as well as carrier concentration in n-type indium doped $PbTe_{1-y}Se_y$ blends affecting Seebeck coefficient (S) and as a result, the PF of $PbTe_{1-y}Se_y$ alloys. High temperatures of about 800 K resulted in a bipolar effect, 0.66 is the limiting value of "ZT" by using 30 percent content. Additionally, they define that increasing carrier concentration must be reduced at higher temperatures improves the quality of thermoelectric properties.

Thermos-electric properties of telluride quadruple sequence ($Tl_{10-x-y}Sn_xBi_yTe_6$) were improved by Kuropatwa *et al.* [113]. XRD process was used to study the crystal structure and it was found to be similar to Tl_5Te_3 type construction, with an increase in volume due to increase in concentration of "Sn" in "$Tl_{10-x-y}Sn_xBi_yTe_6$". According to the electronic structure. $Tl_{8.5}SnBi_{0.5}Te_6$ and $Tl_9Sn_{0.5}Bi_{0.5}Te_6$ are p-type intrinsic and extrinsic semiconductors with narrow band gaps. $Tl_9Sn_{1-y}Bi_yTe_6$, $Tl_{8.67}Sn_{1-y}Bi_yTe_6$ and $Tl_{8.33}Sn_{1.12}Bi_{55}Te_6$ having electrical conductivity are lost with enlargement in the temperature. Owing to the electron of thermal conductivity κ_{el}, thermal conductivity of $Tl_{10-x-y}Sn_xBi_yTe_6$ types materials exhibits a modest rise of the sequence of 0.4 $Wm^{-1}K^{-1}$ to 1.4 $Wm^{-1}K^{-1}$, while $Tl_9Sn_{0.2}Bi_{0.8}Te_6$ thermal conductivity drops as inflation in temperature due to enlargement in lattice vibration. The temperature also increases the quantity of (PF), Seebeck coefficient (S), and (ZT). Tl_9(Sn, Bi)Te_6 type materials

showed the highest value of power factor $S^2\sigma = 8.1\ \mu Wcm^{-1}K^{-2}$. They revealed that concentration of "Sn" decreases (PF) and (S) increases as temperature decreases power factor (PF) decreases.

Quansheng Guo [114] used a collection of melting and hot-pressing techniques to produce multiple crystalline majority substances with the structure "$Tl_9Sb_{1-m}Te_6$ " $\{(0 \leq m, n \leq 0.10)\}$. "Sb" occupies the 4c site of space group I4/mcm in the Tl_5Te_3-type structure, as shown by XRD. From the standpoint of valence band filling, he interpreted the replacements of "Sn" atoms for "Sb" to be P-type doping a analyzed the relationship between increasing electrical and thermal conductivity and decreasing Seebeck coefficient. He also noted that pristine Tl_9SbTe_6 and Tl_9BiTe_6 still have the best thermoelectric characteristics.

1.13 References

[1] Japan Agency for Natural Resources and Energy. *Energy White Paper 2005* (Tokyo, 2005).

[2] http://www.altenews.com/Alternative%20Energy%20Overview.pdf

[3]http://www.euractiv.com/en/energy/analysis-efficiency-coal-fired-power-stations-evolutionprospects/ article-154672.

[4] Jason Hu, "Energy Harvesting Support for Sensor Network", *IPSN* 2005.

[5] http://intel-alliance.org/signal/articles/anmviewer.asp?a=1279&print=ye

[6] T.J. Seebeck, Ann. Phys. **82** (1826) 253–286.

[7] J.C.A. Peltier, Ann. Chem. Phys. **56** (1834) 371–386.

[8] E. Lenz, Analen der Physik **120** (1838) 342–349.

[9] W. Thomson, Math. Phys. Pap. **1** (1851) 175–183.

[10] W. Thomson, Proc. R. Soc. Edinburgh (1851).

[11] D.M. Rowe. "Thermoelectric handbook: macro to nano." CRC/Taylor & Francis, Boca Raton, (2006).

[12]. L.Onsagar, Phys. Rev.**37** (1931) 405-406.

[13]. L.Onsagar, Phys. Rev.**37** (1931) 2265-2279

[14]. C.A.Domenicali, Rev.Mod.Phys.**26** (1954) 237-275

[15]. T.C.Harman, J.M.Honig, "Thermoelectric and thermo-magnetic effect and application." McGraw-Hill, New York, (1967)

[16] R. Franz and G. Wiedemann, Ann Phys-Berlin **165**, (1853), 497.

[17]. Gayner C, Kar KK." Recent advances in thermoelectric materials". Prog. Mater Sci. **83**, (2016), 330-382.

[18]. Zhang J, Wu D, He D." Extraordinary thermoelectric performance realized in n-type PbTe through multiphase nano-structure engineering". Adv. Mater. **29**, (2017), 1703148.

[19]. Yang L, Chen Z-G, Hong M. "N-type Bi-doped PbTe nano-tubes with enhanced thermoelectric performance". Nano Energy. **31**, (2017), 105-112.

[20]. Luo ZZ, Zhang X, Hua X. "High thermoelectric performance in supersaturated solid solutions and nano-structured n-type PbTe-GeTe". Adv. Funct. Mater. **28**, (2018), 1801617.

[21]. Lee MH, Yun JH, Kim G. "Synergetic enhancement of thermoelectric performance by selective charge and localization-delocalization transition in n-type Bi-doped PbTe/Ag_2Te nano-composite". ACS Nano. **13**, (2019), 3806-3815.

[22]. Luo J, You L, Zhang J. "Enhanced average thermoelectric figure of merit of the PbTe-SrTe-MnTe alloy". ACS Applied Mater Interfaces. **9**, (2017), 8729-8736.

[23]. Pei Y, Tan G, Feng D. "Integrating band structure engineering with all-scale hierarchical structuring for high thermoelectric performance in PbTe system". Adv. Energy Mater. **7**, (2017), 1601450.

[24]. Xiao Y, Wu H, Li W. "Remarkable roles of Cu to synergistically optimize phonon and carrier transport in n-type PbTe- Cu_2Te". J Am Chem. Soc. **139**, (2017), 18732-18738.

[25]. Luo Z-Z, Hao S, Zhang X, et al. "Soft phonon modes from off-center Ge atoms lead to ultralow thermal conductivity and superior thermoelectric performance in n-type PbSe–GeSe." Energy Environ Sci. **11**, (2018), 3220-3230.

[26]. Korkosz RJ, Chasapis TC, Lo S-h, et al. "High ZT in p-type $(PbTe)_{1-2x}(PbSe)_x(PbS)_x$ thermoelectric materials." J Am Chem. Soc. **136**, (2014), 3225-3237.

[27]. Wu H, Zhao L-D, Zheng F. "Broad temperature plateau for thermoelectric figure of merit ZT> 2 in phase-separated $PbTe_{0.7}S_{0.3}$". Nat Commun. **5**, (2014), 4515.

[28]. Tan G, Shi F, Hao S. "Non-equilibrium processing leads to record high thermoelectric figure of merit in PbTe-SrTe". Nat. Commun. **7**, (2016), 12167.

[29]. Wang H, Hwang J, Snedaker ML. "High thermoelectric performance of a heterogeneous PbTe nanocomposite". Chem. Mater. **27**, (2015), 944-949.

[30]. Jian Z, Chen Z, Li W, Yang J, Zhang W, Pei Y. "Significant band engineering effect of YbTe for high performance thermoelectric PbTe". J Mater Chem. C. **3**, (2015), 12410-12417.

[31]. Hu X, Jood P, Ohta M. "Power generation from nanostructured PbTe-based thermoelectric comprehensive development from materials to modules". Energy Environ Sci. **9**, (2016), 517-529.

[32]. Li Z-Y, Li J-F, Zhao W-Y. "PbTe-based thermoelectric nanocomposites with reduced thermal conductivity by sic nano dispersion". Appl. Phys Lett. **104**, (2014), 113905.

[33]. Sarkar S, Zhang X, Hao S. "Dual alloying strategy to achieve a high thermoelectric figure of merit and lattice hardening in p-type nanostructured PbTe". ACS Energy Lett. **3**, (2018), 2593-2601.

[34]. Tan G, Hao S, Cai S. "All-scale hierarchically structured p-type PbSe alloys with high thermoelectric performance enabled by improved band degeneracy". J Am Chem. Soc. **141**, (2019), 4480-4486.

[35]. Ginting D, Lin C-C, Lydia R. "High thermoelectric performance in pseudo quaternary compounds of $(PbTe)_{0.95-x}$ $(PbSe)_x(PbS)_{0.05}$ by simultaneous band convergence and nano precipitation". Acta Mater. **131**, (2017), 98-109.

[36] P. Pichanusakorn, Y. J. Kuang, C. Patel, C. W. Tu, and P. R. Bandaru. "Feasibility of enhancing the thermoelectric power factor in GaN_xAs_{1-x}," Phys. Rev. B., **86**, (2012), 085314

[37]. G. K. H. Madsen. "Automated search for new thermoelectric materials: the case of LiZnSb" J. Am. Chem. Soc., **128**, (2006), 12140.

[38]. J-C Zheng, "Recent advances on thermoelectric materials. "Front. Phys. China, **3,** (2008), 3.

[39]. C. Wood, "Materials for thermoelectric energy conversion." Rep. Prog. Phys. **51,** (1988), 459.

[40]. G. A. Slack, CRC Handbook of thermoelectric, CRC Press, Boca Raton, (1995), 407.

[41]. G.D. Mahan, J.O. Sofo, "The best thermoelectric" Proc. Natl. Acad. Sci. **93** (1996), 7436.

[42]. G.D. Mahan, B. Sales, J. Sharp, "Thermoelectric materials: new approaches to an old problem." Phys. Today, **50,** (1997), 42.

[43]. C. Wood, "Materials for thermoelectric energy conversion." Rep. Prog. Phys. **51**, (1988), 459.

[44]. H. J. Goldsmid, "Electronic refrigeration." Ion, London, (1986).

[45]. T. Caillat, J. P. Fleurial and A. Borshchevsky. "Nanostructured $Co_{1-x}Ni_xSb_3$ skutterudites: synthesis, thermoelectric properties, and theoretical modeling." Proc. Int. Conf. Thermoelectric. **1**, (1996), 100.

[46]. G.S. Nolas, D.T. Morelli, T.M. Tritt, "Glass-electron crystal approach to advanced thermoelectric energy conversion applications." Annu. Rev. Mater. Sci., **29**, (1999), 89.

[47]. H. Kleinke, "New bulk materials for thermoelectric power generation: clathrates and complex antimonides." Chem. Mater.**22**, (2009), 604.

[48]. P. Rogl, CRC thermoelectrics handbook, CRC Press, Boca Raton, (2006), 32.

[49]. E.S. Toberer, A.F. May, G.J. Snyder, "Zintl chemistry for designing high efficiency thermoelectric materials."Chem. Mater.**22**, (2010), 624.

[50]. M.S. Dresselhaus, G. Chen, M.Y. Tang, R.G. Yang, H. Lee, D.Z. Wang, "New directions for low-dimensional thermoelectric materials." Advanced materials.**19**, (2007), 1043.

[51]. A. I. Hochbaum, R. Chen, R. D. Delgado, W. Liang, E. C. Garnett, M. Najarian, A. Majumdar, P. Yang, "Enhanced thermoelectric performance of rough silicon nanowires." Nature **451**, (2008), 163.

[52]. D. Vashaee and A. Shakouri, "Improved thermoelectric power factor in metal-based superlattices" Phys. Rev. Lett. **92**, (2004), 106103

[53]. W. Kim, S. L. Singer, A. Majumdar, D. Vashaee, Z. Bian,A. Shakouri, G. Zeng, J. E. Bowers, J. M. O. Zide, A. C. Gossard, "Thermoelectric power generator module of 16×16 $Bi_2Te_3Bi_2Te_3$ and 0.6% ErAs: $(InGaAs)_{1-x}(InAlAs)_x$ segmented elements. " Appl. Phys. Lett. **88**, (2006), 242107

[54]. S. M. Lee, D. G. Cahill, R. Venkatasubramanian, "Thermal conductivity of Si–Ge superlattices." Appl. Phys. Lett. **70**, (1997), 2957.

[55]. D. Vashaee, A. Shakouri, "Detrimental influence of nano structuring on the thermoelectric properties of magnesium silicide." J. Appl. Phys. **101,** (2007), 053719.

[56]. M. Hansen, K. Anderko, "Constitution of binary alloys." New York: McGraw HillBook Company, (1958), 332.

[57]. Nolas, G.S., Sharp, J., and Goldsmid, H.J. "Thermoelectrics: basic principles and new materials developments." Springer Verlag, (2001).

[58]. Gross, A.J. "Low power, integrated, thermoelectric micro-coolers for microsystems applications." Ph.D. dissertation, University of Michigan, (2010).

[59] A.S. Ivanov, "Thermoelectric air conditioner for railways-modification, results, prospects." in 21st International Conference on Thermoelectric, Voronezh, (2002).

[60] B. wang, "Thermo electronics for cars, trucks, submarines, refrigerators and more," © 2014 New Big Future Inc, 04 October 2007. [Online]. Available: http://nextbigfuture.com/2007/10/thermoelectronics-for-cars-trucks.html.

[61] S. Amandeep Sharma, "Thermoelectric effect, its background, and scope in dairy: review." © global journal of engineering science and research management, **8**, (2014) 14-28.

[62] L. L. G. F. Hongxia Xi, "development and applications of solar-based thermoelectric technologies." Renewable and Sustainable Energy Reviews, **11**, (2007), 923-936.

[63] H. Kaibe, "Recovery of plant waste heat." **57**, (2011), 26-30.

[64] J. I. G. Jihad G. Haidar, "Waste heat recovery from the exhaust of low-power diesel engine using thermoelectric generators." in 20th International Conference on Thermoelectric, Melbourne, (2001).

[65] A.F. Ioffe, "Semiconductor Thermos elements, and Thermoelectric Cooling." Info search, London, (1957).

[66] https://www.orau.org/ptp/collection/Miscellaneous/pacemaker.html, last access (2018).

[67] J.D. Ryan, A. Lund, A.I. Hofmann, R. Kroon, R. Sarabia-Riquelme, M.C. Weisenberger, C. Müller, "All-Organic Textile Thermoelectric with Carbon-Nanotube-Coated n-Type Yarns." ACS Appl. Energy Mater. **1** (2018) 2934–2941.

[68] Fedorov, M.I., "Thermoelectric silicide's: past, present, and future." Journal of Thermoelectricity **2**, (2009), 51-60.

[69] J. Yang, T. Caillat, "Thermoelectric materials for space and automotive power generation." MRS Bull. **31** (2011) 224-229.

[70] B.A. Abdurakhmanov, K.M. Iliev, S.A. Tachilin, A.R. Toshev, "Silicon solar cells with si-ge micro hetero junctions." Russ. Microelectron. **41**, (2012), 169-171.

[71] B. Yu, M. Zebarjadi, H. Wang, K. Lukas, H. Wang, D. Wang, C. Opeil,M. Dresselhaus, G. Chen, Z. Ren, "Enhancement of thermoelectric properties by modulation-doping in silicon germanium alloy nanocomposites." Nano Lett. **12**, (2012), 2077-2082.

[72] Usenko, Andrey; Moskovskikh, Dmitriy; Gorshenkov, Mikhail; Voronin, Andrey; Stepashkin, Andrey; Kaloshkin, Sergey; Arkhipov, Dmitriy; Khovaylo, Vladimir, "Enhanced Thermoelectric figure of merit of p-type $Si_{0.8}Ge_{0.2}$ nanostructured spark plasma sintered alloys with embedded SiO_2 nanoinclusions". Scripta Materialia, **127,** (2017), 63–67

[73] Wang, X. W.; Lee, H.; Lan, Y. C.; Zhu, G. H.; Joshi, G.; Wang, D. Z.; Yang, J.; Muto, A. J.; Tang, M. Y.; Klatsky, J.; Song, S.; Dresselhaus, M. S.; Chen, G.; Ren, Z. F." Enhanced thermoelectric figure of merit in nanostructured n-type silicon germanium bulk alloy". Applied Physics Letters, **93**, (2008), 193121.

[74] Joshi, Giri; Lee, Hohyun; Lan, Yucheng; Wang, Xiaowei; Zhu, Gaohua; Wang, Dezhi; Gould, Ryan W.; Cuff, Diana C.; Tang, Ming Y.; Dresselhaus, Mildred S.; Chen, Gang; Ren, Zhifeng." Enhanced thermoelectric figure-of-merit in nano-structured p-type silicon germanium bulk alloys". Nano Letters, **8**, (2008) 4670–4674.

[75] Usenko, Andrey; Moskovskikh, Dmitry; Korotitskiy, Andrey; Gorshenkov, Mikhail; Zakharova, Elena; Fedorov, Aleksandr; Parkhomenko, Yury; Khovaylo, Vladimir "Thermoelectric properties and cost optimization of spark plasma sintered n-type $Si_{0.9}Ge_{0.1}$ - Mg_2Si nano-composites". Scripta Materialia, **146**, (2018). 295–299

[76] Zebarjadi, Mona; Joshi, Giri; Zhu, Gaohua; Yu, Bo; Minnich, Austin; Lan, Yucheng; Wang, Xiaowei; Dresselhaus, Mildred; Ren, Zhifeng; Chen, Gang." Power factor enhancement by modulation doping in bulk nano-composites." **11**, (2011) 2225–2230.

[77]. K. F. Hsu, S. Loo, F. Guo, W. Chen, J.S. Dyck, C. Uher, "Cubi $AgPb_{(m)}SbTe_{(2+m)}$: bulk thermoelectric materials with high figure of merit." Science **303**, (2004), 818.

[78]. J.P. Heremans, V. Jovovic, E.S. Toberer, A. Saramat, K. Kurosaki, "Enhancement of thermoelectric efficiency in PbTe by distortion of the electronic density of states" A. Charoenphakdee. Science **321**, (2008), 554

[79] J.R. Sootsman, D.Y. Chung, M.G. Kanatzidis," New and old concepts in thermoelectric materials," Angew. Chem. **48**, (2009), 8616-8639.

[80] Y.-P. Jiang, X.-P. Jia, W. Guo, H.-W. Xu, L. Deng, S.-Z. Zheng, H.-A. Ma, "Elevation of the power factor of Co_4Sb_{12} skutterudite with sm-doping in high-pressure high-temperature synthesis", Chin. Phys. Lett. **27**, (2010), 068102.

[81] G.S. Nolas, M. Kaeser, R.T. Littleton, T.M. Tritt, "High figure of merit in partially filled ytterbium skutterudite materials," Appl. Phys. Lett. **77**, (2000), 1855.

[82] Y. Tang, R. Hanus, S.-W. Chen, G. Jeffrey Snyder, "Solubility design leading to high figure of merit in low-cost ce-cosb$_3$ skutterudites." **(6)**, (2015), 7584.

[83] X. Li, Q. Zhang, Y. Kang, C. Chen, L. Zhang, D. Yu, Y. Tian, B. Xu, "High pressure synthesized ca-filled $CoSb_3$ skutterudites with enhanced thermoelectric properties," J. Alloy. Comp. **677**, (2016), 61-65.

[84] Y. Kang, F. Yu, C. Chen, Q. Zhang, H. Sun, L. Zhang, D. Yu, Y. Tian, B. Xu, "High pressure synthesis and thermoelectric properties of Ba-filled $CoSb_3$ Skutterudites," J. Mater. Sci. Mater. Electron. **28**, (2017), 8771-8776.

[85] K. Kurosaki, A. Harnwunggmoung, S. Yamanaka, "Thermoelectric properties of $CoSb_3$ based skutterudites filled by group 13 elements," in: X. Wang, Z.M. Wang (Eds.), Nano-scale Thermoelectrics, **16**, (2014), 301-325.

[86] G.S. Nolas, J. Yang, H. Takizawa, "Transport properties of germanium-filled $CoSb_3$", Appl. Phys. Lett. **84**, (2004), 5210-5212.

[87] Y.Z. Pei, J. Yang, L.D. Chen, W. Zhang, J.R. Salvador, J. Yang, "Improving thermoelectric performance of caged compounds through light-element filling," Appl. Phys. Lett. **95**, (2009), 042101.

[88] J. Zhang, B. Xu, L.-M. Wang, D. Yu, Z. Liu, J. He, Y. Tian, "Great thermoelectric power factor enhancement of $CoSb_3$ through the lightest metal element filling," Appl. Phys. Lett. **98**, (2011), 072109.

[89] J. Zhang, B. Xu, L.-M. Wang, D. Yu, J. Yang, F. Yu, Z. Liu, J. He, B. Wen, Y. Tian, "High-pressure synthesis of phonon-glass electron-crystal featured thermoelectric $Li_xCo_4Sb_{12}$", Acta Mater. **60**, (2012), 1246-1251.

[90] W. Zhao, Z. Liu, Z. Sun, Q. Zhang, P. Wei, X. Mu, H. Zhou, C. Li, S. Ma, D. He, P. Ji, W. Zhu, X. Nie, X. Su, X. Tang, B. Shen, X. Dong, J. Yang, Y. Liu, J. Shi, "Super-paramagnetic enhancement of thermoelectric performance," Nature **549**, (2017), 247-251.

[91]. J. shuai, B.Ge, J.Mao,Song, Y.wang, Z.Ren, "Significant role of mg stoichiometry in designing high thermoelectric performance for $Mg_3(Sb,Bi)_2$ based n-type zintls," j.AM. Chem. Soc. **140**, (2018) 1910-1915.

[92]. X.Chen, H.Wu, J.Cui, Y.Xaio, Y.Zhang, J.He, Y.Chen, J.cao, W.cai, S.J.Pennycook,Z.Liu, L.D.Zhao, J.sui, "Extra ordinary thermoelectric performance in n-type manganese doped : high band degeneracy tuned carried scattering mechanism and hierarchical micro-structure." Nano Energy **52**,(2018), 246-256

[93]. J. Drabble and C. Goodman, "Chemical bonding in bismuth telluride." J Phys Chem Solids **5**, (1958), 142.

[94]. Yan, X.; Wang, D.; Muto, A.; Vashaee, D.; Poudel, B.; Hao, Q.; Ma, Y.; Lan, Y.; Minnich, A.; Yu, B. "High-thermoelectric performance of nano-structured bismuth antimony telluride bulk alloys.", **320** (2008), 634–638.

[95] Li, Jianhui; Tan, Qing; Li, Jing-Feng; Liu, Da-Wei; Li, Fu; Li, Zong-Yue; Zou, Minmin; Wang, Ke. "BiSbTe-based nano-composites with high <I>ZT</I>: the effect of sic nanodispersion on thermoelectric properties." Advanced Functional Materials, **23,** (2013), 4317–4323.

[96] Kim, S. I.; Lee, K. H.; Mun, H. A.; Kim, H. S.; Hwang, S. W.; Roh, J. W.; Yang, D. J.; Shin, W. H.; Li, X. S.; Lee, Y. H.; Snyder, G. J.; Kim, S. W. "Dense dislocation arrays embedded in grain boundaries for high-performance bulk thermoelectrics". Science, **348,** (2015), 109–114.

[97] Kim, Kyung Tae; Min, Tae Sik; Kim, Sung Dae; Choi, Eun-Ae; Kim, Dong Won; Choi, Si-Young "Strain-mediated point defects in thermoelectric p-type bismuth telluride polycrystalline." Nano Energy, **55,** (2019), 486-393.

[98] Shi, X.; Chen, L.; Uher, C. "Recent advances in high-performance bulk thermoelectric materials". International Materials Reviews, **61**(2016), 379-415.

[99] A. Majumdar, "Thermoelectricity in semiconductor nanostructures." Science **303**, (2004), 777

[100] E. S. Toberer, A. F. May, and G. J. Snyder, "Zintl chemistry for designing high efficiency thermoelectric materials." Chem Mater **22**, (2010), 624.

[101] J. R. Sootsman, D. Y. Chung, and M. G. Kanatzidis, Angew, "New and old concepts in thermoelectric material." Chem **48**, (2009), 8616.

[102] H. U. H. M. S. Y. Ken Kurosaki, "Thermoelectric properties of thallium antimony telluride," Journal of Alloys and Compounds, (2004), 43-48.

[103] N. S. H. K. Abdeljalil Assoud, "Crystal structure, electronic structure and physical properties of the new low-valent thallium silicon telluride $Tl_6Si_2Te_6$ in comparison to $Tl_6Ge_2Te_6$," Journal of Solid State Chemistry, **179,** (2006), 2707-2713.

[104] Y. Ken Kurosaki, "Fabrication and thermoelectric properties of Ag_9TlTe_X(X=5:0~6:0)," Materials Transactions, **48**, (2007), 2083-2087.

[105] J. S. Joseph P. Heremans, "Enhancement of thermoelectric efficiency in PbTe by distortion of the electronic density of states," Science, **321**, (2008), 554-557.

[106] H. K. Cheriyedath Raj Sankar, "Syntheses, crystal structures and thermoelectric properties of two new thallium tellurides: Tl_4ZrTe_4 and Tl_4HfTe_4," Journal of Materials Chemistry, **20**, (2010), 7485-7490.

[10] H. K. Cheriyedath Raj Sankar, "Structural, thermal, and physical properties of the thallium zirconium telluride Tl_2ZrTe_3," Chemistry of Materials, **23**, (2011), 3886-3891.

[108] H. K. Cheriyedath Raj Sankar, "Thermoelectric properties of $TlGdQ_2$ (Q = Se, Te) and Tl_9GdTe_6," Journal of Electronic Materials, **41**, (2012), 1662-1666.

[109] H. K. Savitree Bangarigadu-Sanasy, "Thermoelectric properties of $Tl_{10-x}Ln_xTe_6$, with Ln=Ce, Pr, Nd, Sm, Gd, Tb, Dy, and Er, and $0.25<x<1.32$," Journal of Alloys and Compounds, (2013), 126-134.

[110] H. Kyung Tae Kim, "Fabrication and enhanced thermoelectric properties of alumina nano-particle-dispersed $Bi_{0.5}Sb_{1.5}Te_3$ matrix composites," Journal of Nano-materials, **20**, (2013).

[111] Z. R. Qian Zhang, "High thermoelectric performance by resonant dopant indium in nano-structured SnTe," Applied Physical Sciences, **110,** (2013), 13261-13266.

[112] C. M. Ashoka Bali, "Thermoelectric properties of indium doped $PbTe_{1-y}Se_y$ alloys," Journal of Applied Physics, **116**, (2014), 033707.

[113] H. K. Bryan A. Kuropatwa, "Optimization of the telluride $Tl_{10-x-y}Sn_xBi_yTe_6$ for the thermoelectric energy conversion," Journal of Inorganic and General Chemistry, (2014), 774-780.

[114] Guo, Q., Chan, M., Kuropatwa, B. A., & Kleinke, H. "Enhanced Thermoelectric Properties of variants of Tl_9SbTe_6 and Tl_9BiTe_6." Chemistry of Materials, **25**, (2013), 4097-4104.

Chapter # 02

Synthesis Methods and Characterization Technique

2.1 Synthesis Method

2.1.1 SOL-GEL Method

The Sol-Gel method is acting as a bottom-up technique. This method is utilized for the synthesis of nanoparticles. The aforementioned method is done in liquid stage. This process is utilized to manufacture nano-materials through dissimilar procedures for example thin fibers porous formation besides thin films. The procedure is completed in two steps, firstly a reactant solution is made in an appropriate liquid, followed by co-fabrication Gel is developed or it's more likely treated for the creation of Gel if it is not formed. Consequent creation is comprised of shape of films or colloidal powder. A precursor establish mixture deposition ways can as well be utilized for the creation of nano-structure. This technique is valuable for the reason that one can regulate creation of concluding micro-structure via directing chemical reaction limits. The shape of sol-gel invention differs by changing the investigational order for reaction. This technique is not often utilized for the mixture. For mixture procedures, usually ternary procedures are concerned with sol-gel technique, namely hydrolysis, alcohol, and water condensation [1]. Sol is a stabilized suspension of colloidal solid particles keeping diameter of insufficient centenary nano-meters, typically inorganic metallic salts, inside a liquid stage. For sol to happen in hard constituent part, thicker than nearby liquid, necessity minor sufficient for power accountable of spreading to remain superior, aside from gravity [2]. Diagram beneath clarify fine the well-known sol-gel procedures. It was utilized via Brok and Arahchige for the arrangement of metal sulfides [3] that technique is correspondingly able for nano-particle combinations [4]. Nanorods, monoliths besides thin films in mutually organic and organic-inorganic complex constituents [5].

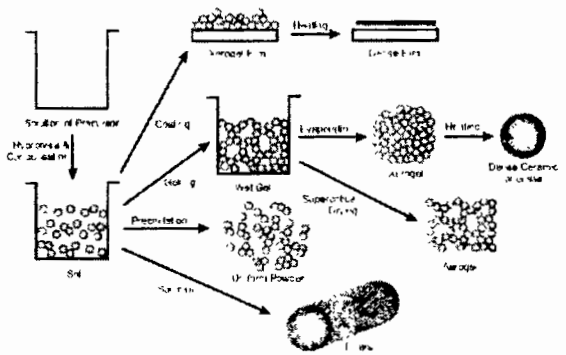

Figure 2.1: Various steps in the sol-gel process to control [6].

2.1.2 Solid State Reaction

The nano-particles like $Tl_9Sb_{1-x}Sn_xTe_6$ are prepared by use of Solid State Process in an evacuated closed silica tube. There is reaction generated which is generally divided into dual stages. Reaction product nucleation along with the growth of the last product polycrystalline powder methods are often used for the fabrication of bulk thermoelectric materials. However, this reaction is always exceedingly sluggish and difficult to complete unless it is accustomed to elevated temperature. Hence that interior atomic construction effortlessly diffuses until the contact grain surface [7].

Generally, the nucleation procedure is highly difficult due to duplicating synthesized lattice reactants that form the product nuclei. Firstly, the nucleation method is complete, and after construction product coatings for rest in reactants for the diffusion state of ions. The area of contact surface as well as progress reaction energies from A to B materials, coating C is produced as a result of the interaction between A and B components. The diffusion atoms or state of ions play an essential characterization in creation of product region at the element C interface, where the continuous chemical action results in additional and heavy production surface. The state of reactivity is gradually decreasing.

Produce coatings thickness degree,

$$\frac{d\Delta x}{dt} \quad \ldots\ldots (2.1)$$

is relative to reactant ion atoms, at that moment growth rate from equations like

$$\frac{dx}{dt} = \frac{k}{x} \quad \ldots\ldots (2.2)$$

In above equation 2, "k" denotes to rate constant, "x" is the resulting production level "C" and "t" denotes the time.

$$\frac{d\Delta x}{dt} = \frac{k}{\Delta x} \quad \text{.....(2.3)}$$

Stochastic variable in the diffusion atom or ion flux "Δx" such as change product layers, thus procedure includes among two materials, for example, A and B correspondingly revealed in Fig.2.2

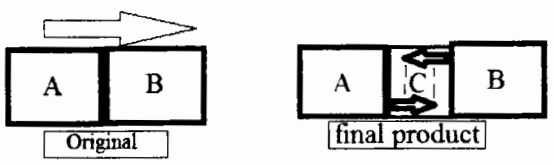

Figure 2.2: Sharing faces between two materials A, and B layers creates new C product layer [3].

The element included among reactants is quantity and interaction surface area which reacts less with particles and causes homogeneity in the model due to its high surface volume ratio. Strong contact between atoms or ions bonding at the lattice site of crystal construction is difficult to transmit to adjacent sites. It is crucial that solid-state reactions occur at temperatures over 2000 ^{0}C and that sufficient energy is provided for atoms or ions to permeate across lattice site [9].

The subsequent process comprised of Solid state reaction for conventional grounding.

I. Obtaining a suitable responding manager who is dehydrated, cleansing and eliminating unwanted oxidation reactions or hydration in the glove box despite the presence of inert argon gas.

II. When considering the stoichiometric ratio of components this will also have done for non-oxide compounds inside the glove box.

III. To obtain a homogeneous reaction mixture, crushing and mixing are recommended.

IV. Previously beaten into a pellet and subjected to heat treatment.

V. Solid-state reaction is an extremely sluggish procedure.

VI. The container carries at very high temperatures throughout the reaction which will be chemically inert to the reactant.

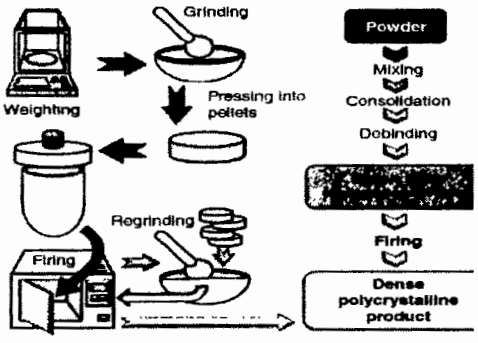

Figure 2.3: Schematic diagram of solid state reaction [9].

2.1.2.1 Evacuated Sealed Silica Tubes

Ahead of heating, the product is a resistive furnace in which the silica tubes are placed in a vacuum line to excrete the argon gas and then closed. For non-oxide substances, closed in the quartz tubes which are the best mutual superior of solid-state reaction. Inside quartz tubes, diametric crucibles are utilized for oxide–base compounds. Proper crucible generally complete of silica tolerated temperature capable of 1400 ^{0}C and extra, for example, alumina as of 1900 ^{0}C.

In tubes, reactant or product reacts and graphite is placed in the tube to coat the interior walls. Due to the fact that the reactant or product is susceptible to water and air [10].

2.1.2.2. Preparation of $Tl_9Sb_{1-x}Sn_xTe_6$ Compounds

The basis of "Sn" doped on thallium telluride model is applied in this technique to obtain thermoelectric goods of complete compounds. Typically, these compounds were used to find new types of ternary and quaternary compounds by starting with Tl^{+1}, Sn^{+3}, $Sb^{+3,}$ and Te^{-2} components. In the meanwhile, because the majority of hypotheses opening compounds for solid-state reactions are irritable to oxygen and moisture where they were evaluating Stoichio-metric chemical substances and moving them to silica tubes which are in glove boxes containing Argon gas to create an inert environment.

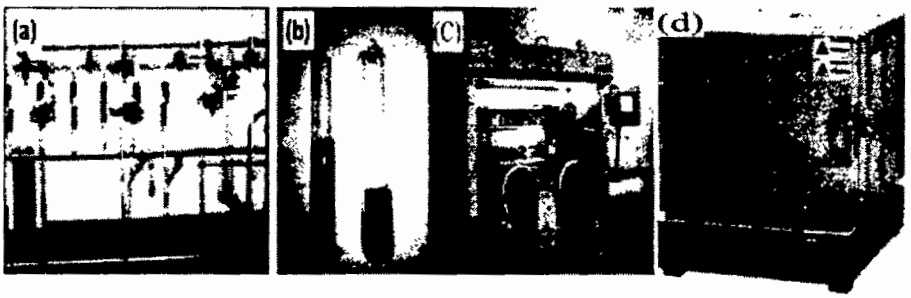

Figure 2.4: (a) Schlenk vacuum line. (b) Vacuum-sealed quartz tube with graphite coating (left) and graphite crucible (right). (C) glove box is filled with organ gas. (d) heating furnace [10].

Earlier pushing these models in resistance furnace to heat them "silica tubes" were arranged in vacuum line to destitute "argon" and then closed where power was heated to the 650 ^{0}C at a pace of no more than 1 k/mint and held there for 24 hours. The model was cooled down bound at a very dilatory pace to evade quenching, dislocations, and crystal deformation. Heating profile for these mixtures is (RT-12h-650C-6h-650C-60h-560C-70h-400C-RT).

Reactions of the manufactured samples through solid-state reaction are as follows.

$\longrightarrow$ $Tl_9Sb_{1-x}Sn_xTe_6$ (unbalanced reaction)

$\longrightarrow$ $Tl_9Sb_{0.99}Sn_{0.01}Te_6$ (balanced reaction)

Atomic weight ratio of precursor is:

(9) Tl: (x)Sn: (1-x) Sb: (6) Te

For x= 0.01

(9) Tl: (0.99) Sb: (0.01) Sn: (6) Te

Tl: Sb: Sn: Te

81: 51: 50: 52

9 x 81: 0.99 x 51: 0.01 x 50: 6 x 52

729: 50.49: 0.5: 312

7.29: 0.50: 0.005: 3.12

7.29 + 0.50 + 0.005 + 3.12

10.91 gm.

Variation in mass of the sample at x=0.01 roughly 10 gm increased the ratio of "x" in the sample by 0.025 and 0.05, resulting in an Atomic weight ratio of precursor values 10.92 and 10.93 correspondingly.

2.1.3 Ball/ Mechanical Milling Method

The process of ball milling is a simple and widely used process as a fabrication of nano-structure, which is similarly recognized as "Mechanical Milling". It is called the top-down method which has been utilized from the start for Nano-science and technology because of its low expenditure and simple procedure [11].

"Nano-grains", "Nano-particles", "Nano-structures", "Nano-alloys", "Nano-composites" and "Nano-quasi crystalline" compounds are often synthesized using this approach in the lab and industry [12]. A compound is settled in the mechanical mill by a becoming milling medium which is constructed of "Stainless Steel". In the procedure of composing Nano-structures in ball mill, the milling medium balls roll down in the chamber and readily fall on the compound from which Nano-structures must be made [13].

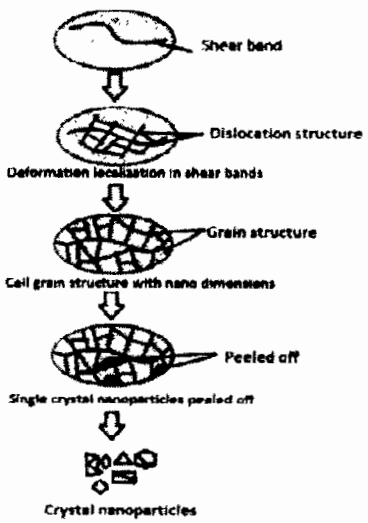

Figure 2.5: Schematic representation of Ball milling mechanism for the formation of crystalline nano-particles.

In this procedure, the fabrication of Nano-structures is dependent on energy. This energy is transferred from the stainless steel balls to the compound. This energy is used to crush the compound [14, 15]. The amount of energy conveyed is determined by a number of factors, including the mill type, the powder used to mechanism the crushing chamber, the size distribution of balls, speed of milling, dry or wet milling, time of milling, and temperature of milling [16].

In the ball mill, kinetic energy (K.E) is determined by the ball's velocity and mass while generally, steel or tungsten balls provide a better-crushed Nano-powder in case of crushing of compound or sample other than ceramic balls [17]. The mean free path for the balls motion reduces as the number of balls in the ball mill increases resulting in an increase in crushing time. Temperature in the ball mill is affected by a number of factors, including the kinetic energy (K.E) of the balls, the milling medium, and properties of the material employed [18]. Higher atomic mobility material is formed with the high temperature otherwise the amorphous phase [19,20] and a Nano-crystalline model are formed [21]. During ball mining, these balls have high energy. Collision of balls with each other increases the energy. Consequently, sample or compound is breakdown to manufacture Nano-structures [22,23]. This process works continuously until nano-structure is a descriptor. At that time, the flak-like configuration or the coagulated powder is defined and at the end, nano-structured powder or nano-particles are made until the process does not stop [24]. In this research effort, for the preparation of Nanoparticles, Fritsch Pulverisette 7 Premium Line ball-miller was used.

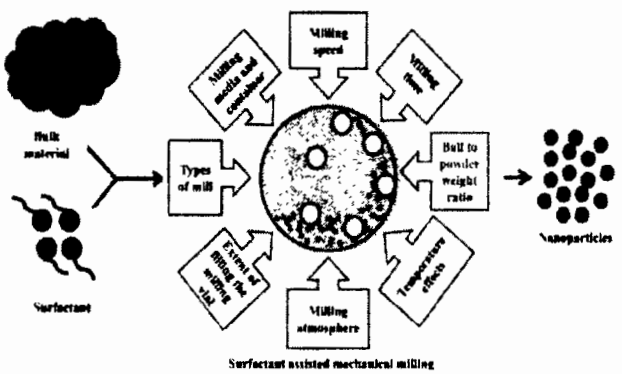

Figure 2.6: Factors influencing the milling process.

To prevent oxidation, all of the substances [Tl, Sb, Sn, Te] are combined according to stoichio-metric ratio in an argon gas in the filled glove box and put in a quartz silica tube, and heated to 900 K using hydrogen-oxygen flame before being progressively cooled to 600 K in a furnace.

After that, the ingot was put with 2mm diameter ZrO_2 marble balls in a high-energy mechanical mill, which was used to crush the sample of $Tl_9Sb_{1-x}Sn_xTe_6$ into fine powder. This substance is agglomeration with an amoral solvent, which is recognized as 2-isopropyle ethanol of 99.8% level of purity used for the absorption of heat.

Then sealed the mechanical mill container and operate for not more than ten minutes at 1000 rpm to protect the apparatus and material from mechanical mill heat. The material is ground for 20 minutes followed by a 10 minutes break and another 5 minutes grind. Use the syringe to push out the material and then dried by evaporation on a hotplate. Normally the powder is about 50-70% softened with ~1 g of each bowl being balanced.

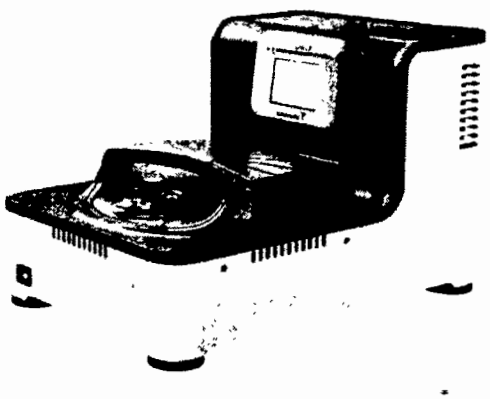

Figure. 2.7: Fritsch Pulverisette 7 Premium Line ball-miller.

2.2 Characterization Technique

2.2.1 X-Ray Diffraction (XRD) Analysis

Wilhelm Roentgen who was a German scientist determined Roentgen rays in 1895 and was given the name X-rays. The X-rays are given of their unknown nature at the time. They have a shorter wavelength and are electromagnetic in nature. X-rays are invisible to the naked eye although they have more penetrating strength than regular light [25]. The discovery of X-rays ushered in a new age of material characterization in a variety of domains. X-rays have a wavelength of about 1Å and are produced when higher energy electrons are assigned to the atom's inner shells [26, 27]. XRD is a method for studying material crystal symmetry. The diffraction pattern will be produced by the interaction of X-rays with crystalline material will generate the diffraction patterns which help in the identification of various materials. These identifications are based on their mono or multi-phase structure. Other identification of various material properties such as stress, stacking faults, impurities in the

structures, phase transition, degree of crystallinity, particle size, and crystal structures are all measured using it [28].

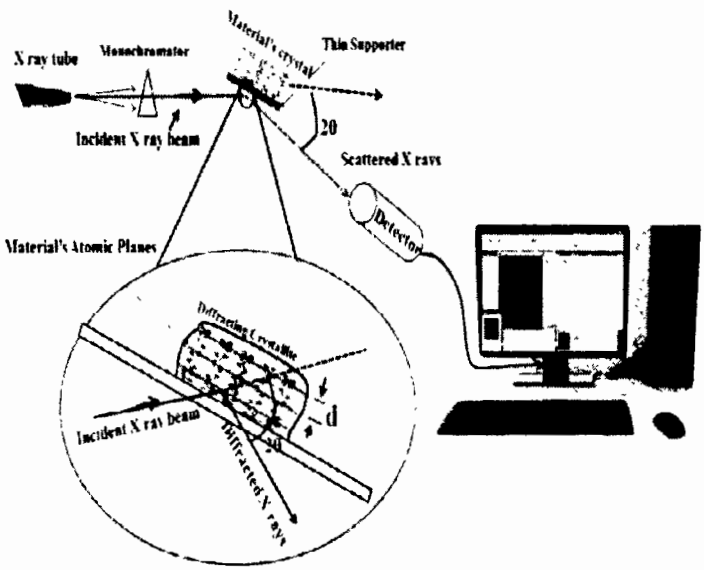

Figure. 2.8: Schematic representations of basic principle of X-ray diffraction (XRD) [29].

"Every substance has possessed their structure and fingerprint, whose can be compared with the XRD rays as (reference) in a database in JCPDS library". Diffraction peaks can be used to identify the purity and impurity levels in a sample. Fig 2.8 depicts the basic idea of XRD. Materials are made up of repeating atomic planes. The atomic planes formed the crystal structure of every given material. Specific tubes are used to create the poly-chromatic cathode rays. These rays are focused onto materials as monochromatic rays. As a result, material patterns are produced through diffracted, absorbed, or transmitted rays. At various atomic planes, the inference of diffracted waves forms a diffraction pattern. Diffraction patterns with prominent interference peaks are produced by arranged or periodic atoms. Bragg's law is followed by XRD [30]

$$m\lambda = 2dsin\theta \quad \ldots\ldots\ldots\ldots\ldots\ldots\ldots\ldots\ldots\ldots\ldots\ldots\ldots\ldots (2.4)$$

where "d" denotes "the distance of lattice planes", "m" denotes "the order of diffraction peak" and "λ" denotes "the wavelength of incident rays". Fig 2.9 depicts a geometrical representation of Bragg's law.

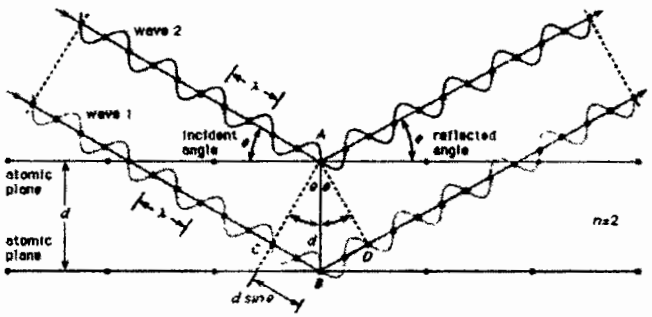

Figure. 2.9: Bragg's law geometrical representations with crystal planes [30].

The following stages are involved in the production of XRD pattern:

- Produce the high-energy electron beam.
- Bombardment of the high-energy electron beam at the target.
- Inter-action of compounds with X-rays.
- Diffracted beams are produced.

Electrons are formed at the cathode node of an X rays tube. These electrons are moved towards the target (anode). They are moved by applying an accelerating voltage between the electrodes. The inner shell transition converts the energy into X-rays because of the aggregation of these electrons. At atomic level, Special information may be collected in the form of diffraction patterns due to the wavelength of X-rays. In case of visible and ultraviolet ranges with long wavelengths are unable to get such kind of information. When monochromatic X-rays having wavelength "λ" impact the substances at an angle "θ", constructive interference occurs only when the distance travelled by the rays reflected from consecutive planes is multifaceted by number of wavelengths "n".

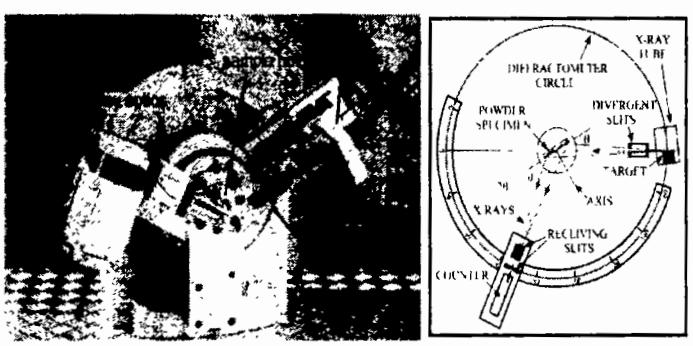

Figure. 2.10: Components of modern X-ray diffraction machine and production of X-rays from X-rays diffractometer [31].

Fig 2.10 depicts the ingredient of a contemporary X-ray diffraction machine as well as the assembly of X-rays from XRD. The spectra of nano-composite materials acquired by XRD are analyzed and indexed using the Computer programmer MDI-jade and Chekcell. Debye Scherer's formula is used to calculate the average crystal size as shown in equation (2.5)

$$t = \frac{k\lambda}{\beta cos\theta} \quad \text{.....(2.5)}$$

as "t" denotes "Crystallite size", "K" shows "Shape factor dependent on material's shape", "β" "indicates Full width at half maximum of material's peak" and "θ" defines "diffraction or Bragg angle" [30,33]. It is utilized in a variety of disciplines to measure various structures. Fig 2.11 shows many applications of XRD in the nano-composite, material science, and medical fields.

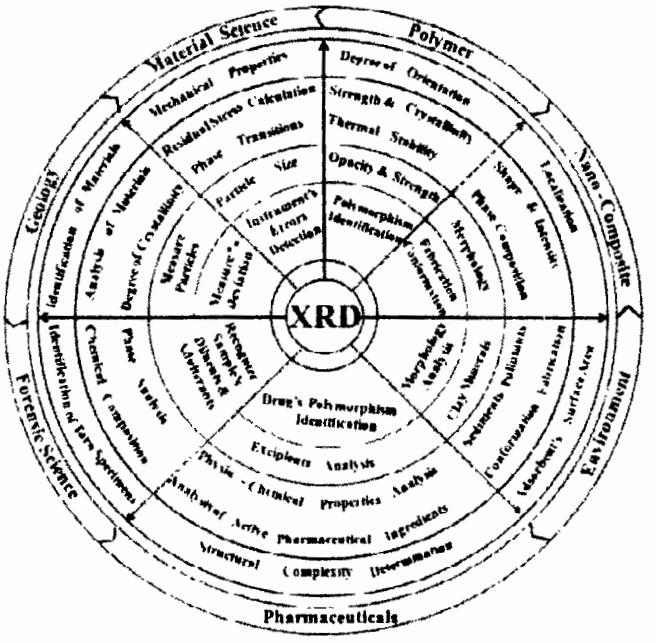

Figure. 2.11: The illustration of different applications of XRD in various fields [31].

2.2.2 Scanning Electron Microscopy (SEM)

The scanning electron microscope (SEM) is the surface probing method. This method is used an intense beam of electrons to analyse the morphology of the prepared material. Instead of using light. The wave nature of electrons is utilized in SEM to enhance image of materials. SEM contains magnetic lenses to focus the electron beam on specimens instead of spherical mirrors in an optical microscope. For

the purpose of material characterization, choose SEM since it has a greater magnification than an optical microscope. Major components of SEM are an anode, electron gun, electron detectors, scanning coils, stage, and magnetic lenses. Fig 2.12 shows a formal SEM. With the use of an electron gun and negative charge beam, material specimens are used to generate the different electrons.

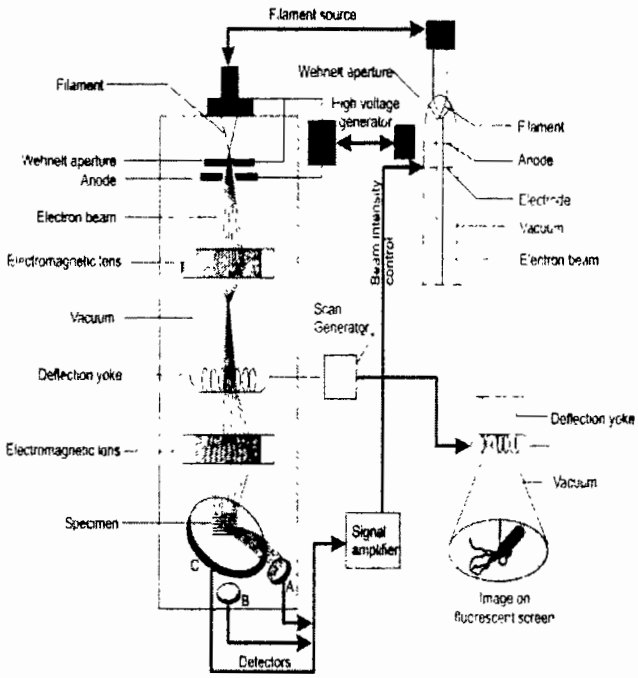

Figure. 2.12: SEM schematic illustration with its different parts [34].

With a beam of electrons, "primary back-scattered electron", "auger electrons", "secondary electrons" and "X-rays" are released from specimen. These emission signals can be used to gather information about chemical compositions and surface morphology created by electron guns from samples. Fig 2.13 shows the electron's Interaction with materials and different types of the electron as well as X-rays emission. The electrons in a scanning electron microscope have a lot of kinetic energy so when they are accelerated they produce a lot of different signals owing to electron interaction with sample. X-rays of a certain kind are produced. The electron removes from the surface when electron beam collides with inner core electrons of materials from the surface. The major sources of information on topography and morphology of the material are characteristic X-rays and secondary negative charge carriers (electrons) [35, 36].

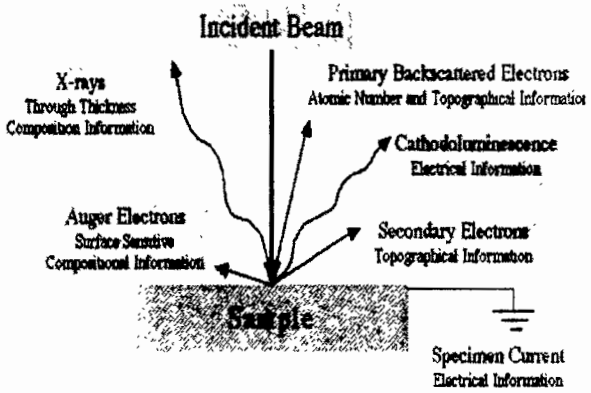

Figure. 2.13: Interaction of incident beam with sample and emission of electrons from surface [33].

A vacuum pump is used in SEM to reduce the disruption and interference caused by electrons with their surroundings. In a sample, various elements of material are assigned allocation through the primary electrons whereas secondary electrons detection provides a greatly enhanced image of around 10 to 500 times the original. There are two basic types of environmental and regular SEMs. These are used in a variety of fields and materials. Environmental SEM is used to examine non-conducting materials, while conductive materials are analyzed through the regular SEM. So, environmental SEM has been done to analyze the materials without conductive coating. The primary goal of applying a coating to non-metallic substances throughout the electron irradiation process is to prevent charge buildup on the plane. As a result, quality and resolution of the image are improved through the coating for the substantial [37].

2.2.3 Energy Dispersive X-rays (EDX) Analysis

Elemental arrangement of the compounds is deliberate by EDX and is used to study the elemental composition of material. It depends on the physical phenomenon between matter and beam of electrons. Its configuration is generally in conjunction with the "SEM" or "TEM X-rays" that originate make the substantial when intense beam of electrons particles collides with substance. During an "EDX" analysis intense amount of beam of electrons is bombarded across the material in a SEM. During that time, high-power electron produces vacancies due to eliminating several electrons from interior shell. Outer shell electrons occupy these vacancies, emitting X-ray photons known as characteristics X-rays. The samples are emitting these X-rays due

to unique energy found in each element according to its characteristic X-ray. Every level of energy in EDX has a unique distinctive spectrum in an atom that reveals the material's elemental analysis. The energy level of each spectrum in EDX reveals essential information about elements with the highest X-rays detected. Every signal sent by an element is analogous to a single peak in an atom. Higher concentration of an element indicates the high intensity of an element of sample in the spectrum. Fig 2.14 shows the EDX's working principle.

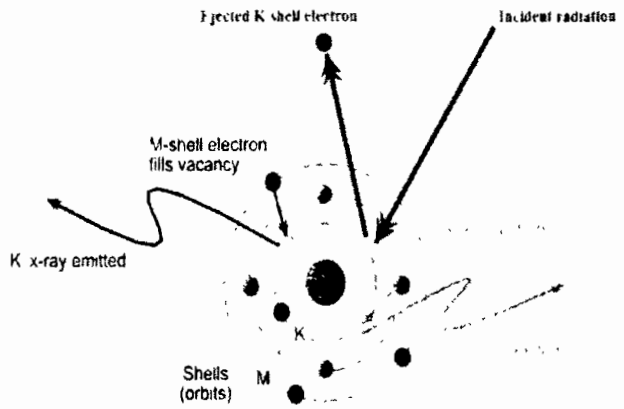

Figure. 2.14: Illustrative diagram of EDX inner shell transitions from an element.

2.2.4 Seebeck Coefficient Measurements

The Seebeck-100 controller constructed by "MMR Technologies Inc." is utilized to measure the Seebeck coefficient. At the constant temperature, [5*1*1 or 6*1*1mm] hot-pressed pellets are utilized as ZEM. Matching is the overall concept for Seebeck measurement, despite its experimental procedure and configuration being slightly different from other measuring device. A thermocouple (Cu: Ni = 55: 45wt-%) is used as a position thermocouple in Fig.2.15 SB-100 Seebeck controller to identify the "Seebeck Coefficient" and "Silver" {"(Leitsilber 200 paint)", "(Ted Pella Inc.)"} guides is also used [38,39].

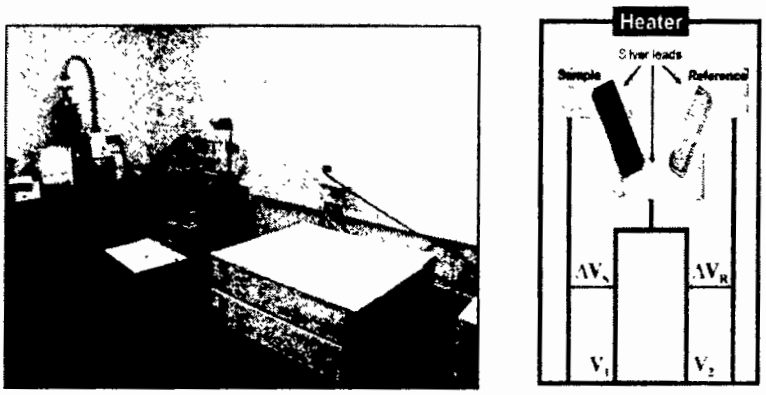

Figure 2.15: Sb-100 Seebeck controller (left) and its Schematic diagram (right).

It is made up of a specimen substantial with silver leads that are settled in the Sb-100 Seebeck controller. A heater is producing the temperature gradient (ΔT) between unidentified along with identified sample of two ends (top along with bottom) as well as a voltages gradient (ΔV) with the assistance of a computer-controlled power function (P). The heater is placed on surface.

Mathematically, the voltage relationship is written as

$$\Delta V_{sample} = S_{sample}\Delta T(P) \quad \text{..... (2.6)}$$

$$\Delta V_{ref} = S_{ref}\Delta T(P) \quad \text{..... (2.7)}$$

while the total Seebeck coefficient is

$$S_{sample} = S_{ref}\frac{\Delta V_{sample}}{\Delta V_{ref}} \quad \text{..... (2.8)}$$

The power function produces the resultant potential difference is rather modest. The measurement of a single point or the thermo-voltage participation (ΔV_{therm}) by the wires and connections might expose a large experimental failure. The measurement is done at two different temperatures ΔT and power settings which reduces ΔV_{therm} by subtracting the combined powers $\frac{P_1}{P_2}$ leading in a [42] more difficult equation (2.6).

$$S_{sample} = S_{ref}\frac{\Delta V_{sample}(P_1)-\Delta V_{sample}(P_2)}{\Delta V_{ref}(P_1)-\Delta V_{ref}(P_2)} \quad \text{..... (2.9)}$$

We can easily and properly analyze the Seebeck values at ordered temperature intervals when the thermal participation is removed and Seebeck rate is measured against a known reference Seebeck value.

2.2.5 Four Probe Method

The electrical conductivity or resistivity of every substance is measured using a four-probe or four-point approach. This approach is shown in Fig. 2.16. 'I' shows an electrical current, which moves in an irregular way, and 'V' is a voltage, which works as the activity of electrical resistivity or conductivity, determined to the other side of flat probe. Maintains constant level *"I"* Done the pellet's region. " V" is measured across physical length between the terminals V_1 and V_2 and resistance of material is evaluated as a result. Using the subsequent equality, the electrical conductivity may easily be found. For resistivity in materials, the major source of electron scattering is lattice vibration and electron-electron vibrations [43].

4.3 (a) Ohm's Law (b) Specific conductivity

$$(a)\ R = \frac{V}{I} \qquad (b)\ \sigma = R^{-1} \cdot \frac{L}{A}$$

Where V= Potential drop, A= Area of pellets, I= Current, and L= length of pellets.

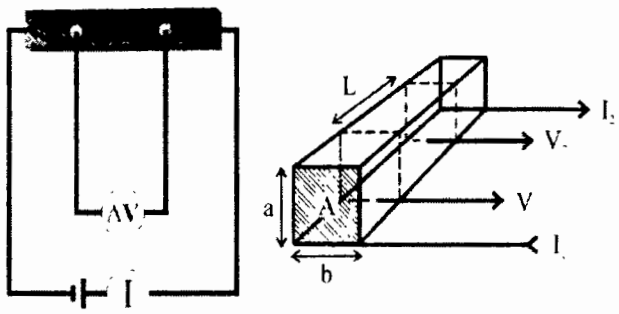

Figure 2.16: Four Probe Resistivity setup.

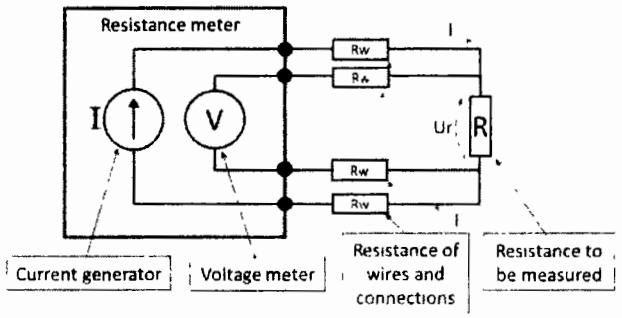

Figure. 2.17: Schematic diagram of R-T measurements of nanoparticles-superconductor composite by four-probe technique.

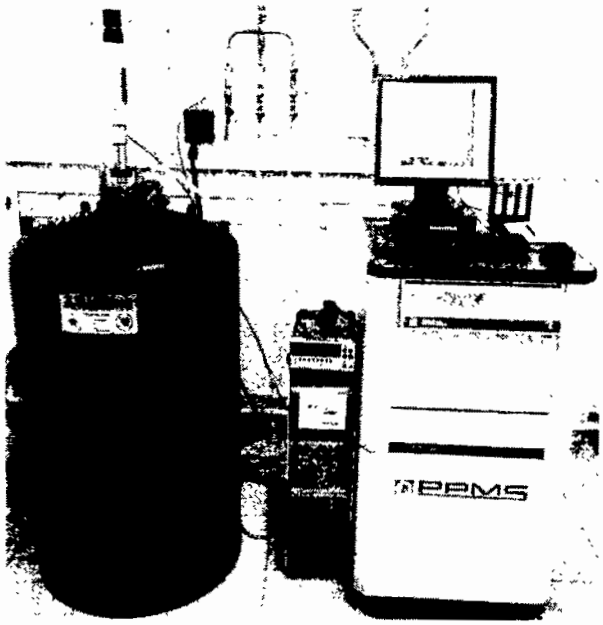

Figure. 2.18: Experimental setup of modern quantum design PPMS [43].

2.2.6 References

[1] F. Branda, "Advances in nanocomposites - synthesis, characterization, and industrial applications", D. B. Reddy, Ed., Shanghai: InTech, (2011).

[2] C. J. Brinker, "Sol-gel science", Wilmington: Academic Press, INC, (1990).

[3] I. U. A. a. S. L. Brock, "Sol-gel methods for the assembly of metal chalcogenide quantum dots," American Chemical Society, (2007), 801–809.

[4] L. Miao, "Preparation of TiO_2 nano-rods by heating-sol-gel template method," Journal of the Ceramic Society of Japan, **112**, (2004), 1329-1331.

[5] A. Sharma, "One-step sol-gel synthesis of hierarchically porous, flow-through carbon/silica monoliths," RSC Advances, **15**, (2016), 12298-12310.

[6] A. L. Hectora, "Materials synthesis using oxide free sol-gel systems," Chemical society reviews, 11, (2007), 1745-1753.

[7] P. Niederberger, "Aqueous and non-aqueous sol-gel chemistry," in Metal Oxide Nano Particles in Organic Solvents, synthesis, Formation, Assembly and Application," Springer, (2009), 7-18.

[8] Elliott, Stephen. "The physics and chemistry of solids" Wiley, (1998), 794.

[9] Schubert, Ulrich, and Husing Nicola. "Synthesis of inorganic materials". John Wiley & Sons, (2012).

[10] Smart, Lesley E., and Elaine A. Moore. "Solid state chemistry: an introduction." CRC Press, (2012), 494.

[11] R. Janot, "Ball-milling in liquid media: applications to the preparation of anodize materials for lithium-ion batteries," Progress in Materials Science," Progress in Materials Science, **50**, (2005), 1-92.

[12] T. P. Yadav, "Mechanical milling, a top-down approach for the synthesis of nano-materials and nano-composites," Nano-science and Nano-technology, **2**, (2012), 22-48.

[13] D. Rowe, "CRC handbook of thermoelectrics," Boca Raton, (1995).

[14] S. Tjong, "Nano-crystalline materials and coatings," Materials Science and Engineering, (2004), 1-88.

[15] J. S. Benjamin, "Mechanical alloying. A perspective," Metal powder Report, **45**, (1990), 122-127.

[16] N. Rajput, "Methods of preparation of nano-particles – a review," international journal of advances in engineering & technology, 7, (2015), 1806-1811.

[17] M. Ullah, "Surfactant-assisted ball milling: a novel route to novel materials with controlled nanostructure- A Review," Rev. Adv. Mat. Sci, **37**, (2014), 1-14.

[18] M. S. El-Eskandarany, "Crystalline-to-amorphous phase transformation in mechanically alloyed Fe50W50 powders," Acta Materialia, **45**, (1997), 1175-1187.

[19] S. Zghal, "Electron microscopy nano-scale characterization of ball milled Cu-Ag powders. Part II: Nano-composites synthesized by elevated temperature milling or annealing," Acta Materialia, **50**, (2002), 4711-4726.

[20] C. Koch, "Synthesis of nanostructured materials by mechanical milling: problems and opportunities," Nanostructured Materials, **9**, (1997), 13-22.

[21] H. Gleiter, "Nano-crystalline materials," Progress in Materials Science, **33**, (1989), 223-315.

[22] A. Chauhan, and P. Chauhan, "Powder XRD technique and its applications in science and technology", J. Anal. Bioanal. Tech. **5**, (2014), 5.

[23] V. Guidi, M. A. Butturi, M. C. Carotta, B. Cavicchi, M. Ferroni, C. Malagu, G. Martinelli, D. Vincenzi, M. Sacerdoti, and M. Zen, "Gas sensing through thick film technology", Sens. Actu. B **84**, (2002), 72.

[24] Y. Waseda, E. Matsubara and K. Shinoda, "X-Ray diffraction crystallography: Introduction, examples and solved problems", Springer (2011).

[25] I. Ivanisevic, R. B. Mcclurg, and P. J. Schields, "Uses of X-ray powder diffraction in the pharmaceutical industry: Pharmaceutical sciences encyclopedia: Drug discovery, development, and manufacturing", John Wiley & Sons, Inc., New Jersey (2010).

[26] A. Dey, A. K. Mukhopadhyay, S. Gangadharan, M. K. Sinha, and D. Basu, "Characterization of micro plasma-sprayed hydroxyapatite coating", J. Therm. Spray Tech. **18**, (2009), 578.

[27] D. Ananias, F. A. A. Paz, L. D. Carlos, and J. Rocha, "Chiral micro-porous rare-earth silico-germanates: Synthesis, structure and photoluminescence properties", Micropor. Mesopor. Mat. **166**, (2013), 50.

[28] M. Nicolae, I. Vilciu, and F. Zaman, "X-ray diffraction analysis of steel slag and blast furnace slag viewing their use for road construction", U. P. B. Sci. Bull., Series B **69**, (2007), 99.

[29] L. J. Chyall, "Current applications of X-ray powder diffraction in the pharmaceutical industry", Amer. Pharmac. Rev. **15**, (2012), 6.

[30] J. Singh, M. Srivastava, A. Roychoudhury, D. W. Lee, S. H. Lee, and B. D. Malhotra, "Bienzyme-functionalized mono-dispersed bio-compatible cuprous oxide/chitosan nano-composite platform for biomedical application", J. Phys. Chem. B **117**, (2013), 141.

[31] R. Das, M. E. Ali, and S. B. A. Hamid, "Current applications of X-rays powder diffraction- A review", Rev. Adv. Mater. Sci. **38**, (2014), 95.

[32] B. D. Cullity, "Elements of X-Ray diffraction", Addison-Wesley, Crop., Massachusetts (1978).

[33] C. Suryanarayana, and M. G. Norton, "X-ray diffraction a practical approach", Springer Science, New York (1998).

[34] R. Jenkins, "X-Ray techniques: Overview", Encycl. Analyt. Chem. (2000).

[35] Y. Leng, "Material characterization", John Wiley & Sons (2008).

[36] Klug, H. Philip, and L. E. Alexander, "X-ray diffraction procedures", New York: Wiley (1954).

[37] M. T. Postek, K. S. Howard, A. H. Johnson, and K. L. Mcmichael, "Scanning electron microscopy", Ladd Res. Ind., Inc. Williston (1980).

[38] D. C. Joy, and C. S. Joy, "Low voltage scanning electron microscopy", Micron **27**, (1996), 247.

[39] J. I. Goldstein, D. E. Newbury, D. C. Joy, C. E. Lyman, P. Echlin, E. Lifshin, L. Sawyer, and J. R. Michael, "Scanning electron microscopy and X-ray micro-analysis" Kluwer Academic/Plenum Publishers, 3rd Ed. New York (2003).

[40] H. Besler, "Scanning electron microscopy", Develop. Sedimen. **59**, (2008), 153.

[41] P. R. Griffiths, "Fourier transform infrared spectroscopy", Plenum Press, New York (1975).

[42] H. Ibach, and H. Luth, "Solid state physics: An introduction to theory and experiment", Spinger Verlag, Berlin (1991).

[43] W. Wang, H. Liu, R. Huang, Y. Zhao, C. Huang, S. Guo, Y. Shan, and L. Li, "Thermal expansion and magnetostriction measurements at cryogenic temperature using the strain gauge method", Front. Chem. **6**, (2018), 72.

Chapter # 03

Optimization of Power Factor in Sn Doped $Tl_{10-X}Sn_XTe_6$ Thermoelectric Chalcogenide Nano-materials

INTRODUCTION

In recent years, the lead (Pb) doped chalcogenides have gotten a lot of interest due to PbTe's high-temperature thermoelectric performance [1]. Thermoelectric materials work to convert the heat into electricity and electricity to heat [2] and have essential uses in waste heat recovery such as industrial processes, as well as "green" energy [3].

At the target operating temperature, greater than 2 values of ZT are required for the widespread application [4]. Biswas et al. lately obtained breakthrough ZT measured as 2.2 by significantly decreasing the intrinsic lattice thermal conductivities of PbX materials by nanostructuring [5]. The chalcogenides also show unique electrical characteristics such as high-temperature band occurrence that wipes extinct rise in the electronic gap with increasing temperature [6–8]. Bandgap such as the electronic structure by in-inebriate (e.g. with Tl) [9] can increase electrical qualities further, whereas chalcogenides alloys, e.g., $PbTe_{1-x}Se_x$ can improve electrical properties and lowering lattice thermal conductivity [7,10]. Many studies have been done to understand these distinctive properties at an essential level in order to increase performance and find a similar better thermoelectric. Various studies of experiments indicate that the lead chalcogenides show high harmonic lattice dynamics [11–13] which is suggested to be a factor in their poor lattice conductivity.

In molecular dynamics measurement [15] thermally induced distortions have been reported to the atomic positions experimentally [11, 13, 14] which would lead to strong phonon-scattering process. Similarly, even at low temperatures, substantial the "Pb" cation will be off-centred in the rock salt lattice observed [11, 13] while the amount of the off-site relocation is still being debated [14].

In this chapter, we will measure the different properties of Sn (Tin) doped thallium telluride ($Tl_9Sn_{1-x}Te_6$) nano-structured scheme. It is synthesized by the ball milling method or mechanical milling. The XRD shows the crystal structure information and phase. The EDX shows the percentage composition in the compound, while SEM shows the morphology of the nanoparticles. Lastly, fixed with "Sn" dopants at dissimilar absorptions and the explanations display that electrical and

thermal possessions are pretentious. Four probe resistivity measurement techniques were calculated for the electrical conductivity and Seebeck effect which had four and two standard probe computation schemes, respectively. Power factor (PF) was calculated from "The Seebeck coefficient" (SB) and "electrical conductivity" (EC). Lastly, the Seebeck (SB) coefficient is raised as the temperature of different concentrations of the compound is increased which is shown in table and figure.

3. Results and Discussions:

3.1 X-Ray Diffraction

Most important technique for measuring the structure of crystals of different materials is X-rays diffraction. Crystallinity, particle size, plane orientation, lattice constant, miller indices, etc. have been determined through this technique. In order to check the purity of the compound, peaks in XRD data are compared with literature and JCPDS cards to evaluate the purity of the chemical, as shown in x-ray diffraction graphs. Fig 3.1 depicts the XRD pattern of sample ($Tl_9Sn_1Te_6$), as well as the literature data given by Kurosaki et al [16]. The XRD spectra XRD $Tl_{10-x}Sn_xTe_6$ (x=1.00, 1.25, 1.50, 1.75, 2.00) of the nano-particles were analyzed by *X'pert High Score Software* with *Reference card: 01-084-2449*. For XRD $Tl_{10-x}Sn_xTe_6$ (x=1.00, 1.25, 1.50, 1.75, 2.00) nano-particles, the diffraction peak at 23.3^0 (121), 29^0 (120), 31^0 (212), 32^0 (130), 34^0 (024), 40^0 (224), 42^0 (006), 46^0 (240), 47^0 (413), 50^0 (044) and 53^0(136) planes recognized the tetragonal crystal structure. The sample corroborated that the XRD structure is well homogeneous with the literature data. The crystal formation of $Tl_9Sn_1Te_6$ with Tl_9BiTe_6 described in the published data [16] is shown in fig 3.1. The crystal structure system has been determined to be isostructural using reference data from Tl_9GdTe_6 and Tl_9BiTe_6 These compounds make the tetragonal structure with space group of i4mcm and a replacement edition of $Tl_{10}Te_6$ (Tl_5Te_3) [16, 17]. $Tl_{10-x}Sn_xTe_6$ has a complicated crystal structure with unit cell volumes ranging from $V = 1005.5056$ for $Tl_9Sn_1Te_6$ to $V = 1022.7177$ for $Tl_8Sn_2Te_6$.

Fig 3.1 shows $Tl_{10-x}Sn_xTe_6$ "$x = 1.00$ 2.00" XRD patterns. The XRD pattern has been clearly found to differ with altering Sn content. When "Sn" is changing from $x = 1$ to $x = 2$ the peak intensity also changes. Sample $Tl_9Sn_1Te_6$ has found highest intensity at $2\theta = 30.69°$ and it decreased as "Sn" concentration increased. While Sample $Tl_{8.25}Sn_{1.75}Te_6$ showed a lower peak in $213, 213$ and 130 planes. On the

opposite side, when "Sn" concentration decreases the peaks increase other than for $Tl_9Sn_1Te_6$ at $\{2\theta = 31.89°$ and $2\theta = 30.47°\}$. It was also analyzed that the peak point varied depending on the "Sn" concentration, ranging from $2\theta = 30.47°$ to $2\theta = 30.69°$ for 213 planes and ranging from $2\theta = 31.89°$ and $2\theta = 32.15°$ for 130 planes. The intensity peak in between the ranging of $2\theta = 23.59°$ and $2\theta = 53.52°$ of remaining planes increases as the "Sn" concentration decreases. The peaks in the XRD pattern fluctuate erratically with modifying "Sn" concentration in $Tl_{10-x}Sn_xTe_6$.

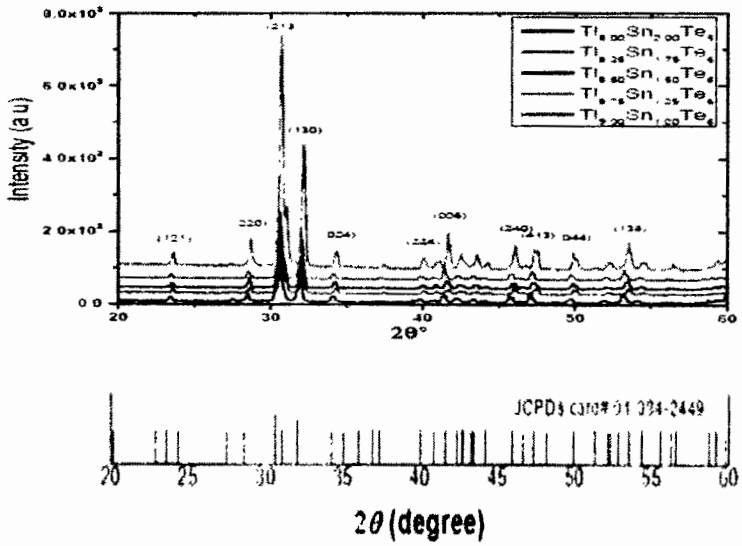

Figure 3.1 XRD $Tl_{10-x}Sn_xTe_6$ (x=1.00, 1.25, 1.50, 1.75, 2.00).

Table 3.1 XRD $Tl_{10-x}Sn_xTe_6$ (x=1.00, 1.25, 1.50, 1.75, 2.00).

	31.972	a = b = 8.8931 c = 13.0032	1004.521
	31.795	a = b = 8.84510 c = 13.07515	1023.925
	31.580	a = b = 8.82510 c = 13.00010	1013.425
	31.323	a = b = 8.81010 c = 13.0010	1009.091
	31.155	a = b = 8.84814 c = 13.16215	1022.712

Although signified through different colors in Fig. 3.1 of compounds in which the compound has different concentrations, different peaks show fluctuating absorptions for Tin (Sn) in model $Tl_{10-x}Sn_{1-x}Te_6$.

3.2 Energy Dispersive X-ray Analysis Energy

The spectrum of "*Sn*" nano-particles doped in $Tl_{10}Te_6$ with Sn= {1, 1.25, 1.50, 1.75 and 2} are shown in Fig 3.2. According to the spectrum, the sample contains 27.26% Te, 65.75% Tl, and 6.99% Sn in $Tl_8Sn_2Te_6$ (Fig. 3.2).

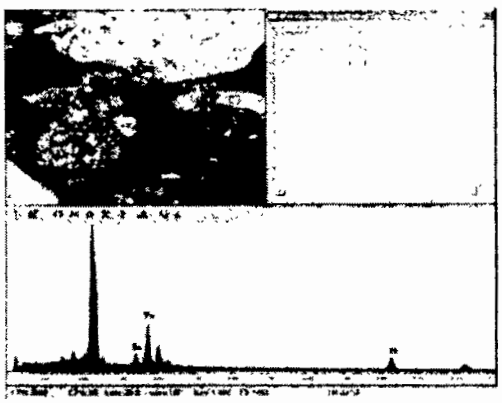

Figure 3.2: Energy Dispersive X-Ray analysis screenshot of ($Tl_9Sn_1Te_6$).

Table 3.2: Energy Dispersive X-Ray analysis screenshot of ($Tl_9Sn_1Te_6$).

Element		At.
Sn	6.99	9.91
Te	27.26	35.95
Tl	65.75	54.24

3.3 Electrical Conductivity Measurements

The sample studied in these experiments belongs to general family of "Sn" doped $Tl_{10}Te_6$, which we have investigated to identify the impact of "Sn" doping in a host composition on electrical and thermal characteristics.

In this study, it has been observed that the outcomes of "Sn" are inebriated in the pure compound on a semiconductor and metallic boundary. A commercial oxford instrument cryostat was used for the experiment that helped to control and improved the temperature by 0.5 K. Modern 4-probe was used to construct with good quality silver points. At room temperature, the resistance of the connection was evaluated and studies were only carried out if it was found to be acceptable. The normal current used was 0.1 mA.

The conductivity in Fig. 3.3 diminishes with temperature rise, displaying the degenerate semiconductor doings due to positive temperature co-efficient caused by

charge carrier phones scattering and grain boundary effects [18]. It is hypothesized that increasing the "*x*" value, which represents the increasing the "Sn" dopants will increase the number of holes, which has been observed experimentally. More gain boundary scattering might explain the lower temperature dependency. The fluctuation of electrical resistivity for $Tl_{10-x}Sn_xTe_6$ (x=1.00, 1.25, 1.50, 1.75, 2.00) with "Sn" concentration showed no consistent pattern. The grain boundary of oxide phase and causes to reduce the electrical conductivity by the grain boundary which has less pressure sintered sample [18-22]. According to band simulation [23], $Tl_8Sn_2Te_6$ was severely inebriated p-type semi-conductor with a mostly empty valence band, whereas the "Fermi-level" in $Tl_8Sn_2Te_6$ is positioned in the band gap [23]. The less sintered compound shows the low electrical conductivity [18-22] may be caused by the oxide impurity phase in the grain boundary and the number of the grain boundary. The band structure computation for $Tl_9Sb_1Te_6$ and $Tl_8Sn_2Te_6$ proposes that $Tl_8Sn_2Te_6$ is a to a great extent inebriate p-type semiconductor with a partly empty valence band, while the "Fermi-level" in $Tl_8Sn_2Te_6$ is situated in the band gap [23]. In concordance with these computations, both thermal and electrical conductivity are acceptable showing that increasing "Sn" contents result in taking down calculation.

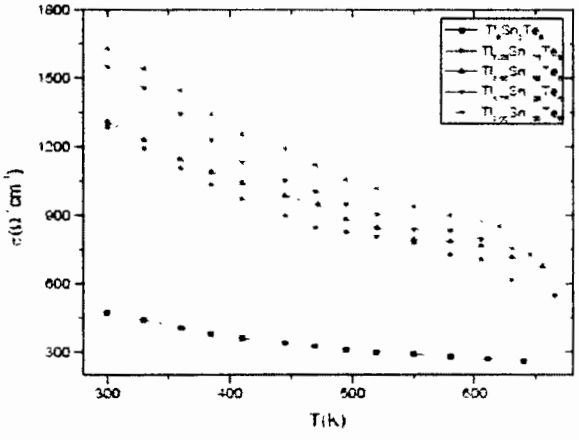

Figure 3.3: Electrical conductivity of $Tl_9Sb_{1-x}Sn_xTe_6$ at 300 K, 400 K, and 550 K.

Table 3.3: Electrical conductivity of $Tl_9Sb_{1-x}Sn_xTe_6$ at 300 K, 400 K, and 550 K.

Sample	Electrical conductivity ($\Omega^{-1}cm^{-1}$) at 300	Electrical conductivity ($\Omega^{-1}cm^{-1}$) at 350	Electrical conductivity ($\Omega^{-1}cm^{-1}$) at 400	Electrical conductivity ($\Omega^{-1}cm^{-1}$) at 450	Electrical conductivity ($\Omega^{-1}cm^{-1}$) at 500	Electrical conductivity ($\Omega^{-1}cm^{-1}$) at 550
	1650	1500	1200	1110	1000	900
	1545	1350	1175	1000	975	760
	1350	1200	1050	975	91	620
	1320	1050	975	850	800	590
	450	450	420	350	325	295

The sample with x=1.00 i.e. Tl_9SbTe_6 displays the highest value of electrical conductivity i.e. 1711 $(\Omega\text{-cm})^{-1}$ at 295 K, and $Tl_8Sb_2Te_6$ reveals the lowest with 445 $(\Omega\text{-cm})^{-1}$ and the samples with x= 1.25 and 1.50 almost have very close values of about 1315 $(\Omega\text{-cm})^{-1}$ and 1325 $(\Omega\text{-cm})^{-1}$ respectively. The conductivity differences at room temperature between the hot pressed pellet and the ingot were observed to a little change from 1315 $(\Omega\text{-cm})^{-1}$ to 1355 $(\Omega\text{-cm})^{-1}$ respectively for the $Tl_{8.5}Sb_{1.5}Te_6$ compound.

3.4 Seebeck Coefficient (S) Measurements

The temperature fluctuation for the $Tl_{10-x}Sn_xTe_6$ (x=1.00, 1.25, 1.50, 1.75, 2.00) compounds as a function of the Seebeck coefficient (S) is given in Fig. 3.4. it was calculated in the temperature varied by the 1K. The increase in temperature from 300-500 K, indicates the positive Seebeck coefficient. The rising temperature is due to the high charge carrier which shows a high Seebeck Coefficient. All of the samples have a positive Seebeck coefficient contains all of the samples have p-type semiconductors, which leads the thermoelectric transport. The carrier's density rises when increased the quality of 'Sn' is from 1.00 to 2.00. However, Sn doping produces smaller grains having the ability to enhance the scattering of electrons, resulting in an alteration of the Seebeck coefficient and effective mass [24-28]. It was analyzed that Seebeck coefficient increases with the little quality of "Sn" doping in this particular system. It means that the doping reduces the Seebeck co-efficient from the optimum "Sn" concentration. Another enhancement could be taken by (i) using the melting spinning as a rapid fabrication method to decrease the size of grain in a large amount, (ii) adjusting the doping elements and their corresponding quantities to

improve charge mobility and carrier density at the same time in order to improve the Seebeck co-efficient at same time [27].

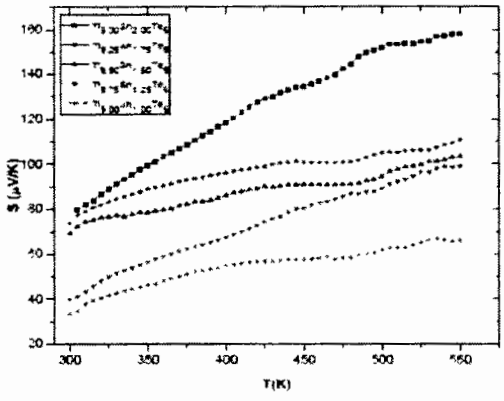

Figure 3.4: Seebeck Coefficient of $Tl_{10-x}Sn_xTe_6$ at 300 K, 400 K, and 550 K.

Table 3.4: Seebeck Coefficient of $Tl_{10-x}Sn_1Te_6$ at 300 K, 400 K, and 550 K.

	30	48	52	60	64	80
	38	58	70	80	83	90
	66	80	90	92	98	98
	72	90	100	101	105	110
	78	100	118	130	150	158

3.5 Power Factor

The power factor (PF) increases with temperature, as seen by the rising behavior of the Seebeck coefficient. As we know the power factor which is described in the first chapter is shown as directly proportional to the Seebeck coefficient square, while the electrical conductivity is also directly related to temperature. The lowest power factor at the temperature of 300 K of Sn=1 was 1.9 $\mu W cm^{-2}K^{-2}$ while the highest S=1 power factor was 7.579 $\mu W cm^{-2}K^{-2}$ observed while in case of "Sn" = 2 the power factor increases with respect to temperature which is 3.639 $\mu Wcm^{-2}K^{-2}$ this low power factor was investigated because of $Tl_8Sn_2Te_6$ exceptionally, which played a key role in the power factor analysis.

For enhancement of PF in "$Tl_{10-x}Sn_xTe_6$ (x=1, 1.25, 1.5, 1.75 and 2) compound, electrical conductivity and Seebeck coefficient product is strongly recommended. Seebeck coefficient hold a deep effect upon PF. We capability "σ"

besides with Seebeck coefficient "S" for determination of proving the enhancement of power factor "PF" and data was organized in Fig. 3.5. Power factor is increasing concerning temperature [29]. The experimental data have given extremely informed about the power factor where in "$Tl_{10-x}Sn_xTe_6$ (x=1, 1.25, 1.5, 1.75 and 2) doping absorption of "Sn" in compound.

The $Tl_8Sn_2Te_6$ compound displayed the highest value of 9.56 μWtt-cm^{-1}-K^{-2} of PF at 550 K and 7.25 μWtt-cm^{-1}-K^{-2} at 290 K. The lowest PF factors were observed for $Tl_9Sb_1Te_6$ compound which has values of 4.13 μWtt-cm^{-1}-K^{-2} at 550 K and 1.75 μWtt-cm^{-1}-K^{-2} at 290 K. As discussed before, a rising "Sn" conductor is rising the number of holes, the controlling charges carrier.

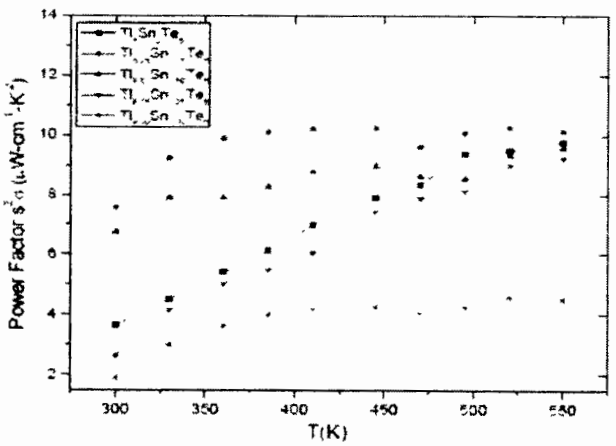

Figure 3.5: Power Factor of $Tl_{10-x}S_{-x}Te_6$ at 300 K, 400 K, and 550 K.

Table 3.5: Power Factor of $Tl_{10-x}Sn_xTe_6$ at 300 K, 400 K, and 550 K.

	1.5	3.5	4	4.6	4.8	4.9
	2.4	4.8	5.3	7	8	8.4
	6.5	8	8.4	9	9.5	9.8
	7.5	9	10	10.1	10.2	10.3
	3.3	5.2	7	7.8	8.1	9.5

3.6 Conclusion

It is analyzed that $Tl_{10-x}Sn_xTe_6$ is a single phase, there are no superfluous peaks and all peaks match their respective elements. This demonstrates that our

design materials have the required structure and that the sample is free of impurities and dislocations. EDS study confirms the percentage of elements present in the sample. The parent compounds have electrical characterization demonstrated as a semiconductor, but as the "Sn" concentration increases, the nano-materials begin to take on metallic properties indicating that as the temperature rises the electrical conductivity falls.

The thermo-power is positive across the temperature range tested and it increases as the temperature rises, indicating that the nano-particles under research are dominated by hole conduction. The Seebeck coefficient of the doped tellurium telluride decreases as the "Sn" concentration increases owing to increased hole concentration, which will cause the rising electron scattering. On the other hand, the smaller grain will be increasing the scattering of electrons resulting in thermos-power which is increasing. Consequently, the highest 10.3 $\mu Wtt\text{-}cm^{-1}\text{-}K^{-2}$ was found for $Tl_{8.25}Sn_{1.75}Te_6$. with high "Sn" denseness risen to {Sn=1.75}. The thermoelectric efficiency will be increased as a result of this improved power factor and results from good thermo-electric implementation which is the main purpose of this research work.

3.7 References

[1] J. R. Sootsman, D. Y. Chung, and M. G. Kanatzidis, "New and old concepts in thermoelectric materials." Angew. Chem. Int. Ed.**48**, (2009), 8616.

[2] J. R. Sootsman, H. Kong, C. Uher, J. J. D'Angelo, C. I. Wu,T. P. Hogan, T. Caillat, and M. G. Kanatzidis, "Effect of Ag or Sb addition on the thermoelectric properties of PbTe" Angew. Chem. Int. Ed. 47, 8618 (2008).

[3] G. J. Snyder and E. S. Toberer, "Complex thermoelectric materials." Nat. Mater. 7, 105 (2008).

[4] J. F. Li, W. S. Liu, L. D. Zhao, and M. Zhou, "High-performance nanostructured thermoelectric materials" NPG Asia Mater.2, 152 (2010).

[5] K. Biswas, J. Q. He, I. D. Blum, C. I. Wu, T. P. Hogan, D. N.Seidman, V. P. Dravid, and M. G. Kanatzidis, "High-performance bulk thermo-electrics with all-scale hierarchical architectures." Nature (London) 489, 414 (2012).

[6] R. N. Tauber, A. A. Machonis, and I. B. Cadoff, "Thermal and Optical Energy Gaps in PbTe" J. Appl. Phys.37, 4855 (1966).

[7] Y. Z. Pei, X. Y. Shi, A. LaLonde, H. Wang, L. D. Chen, and G. J. Snyder, "Convergence of electronic bands for high performance bulk thermoelectrics" Nature (London),473, 66 (2011).

[8] Z. M. Gibbs, H. Kim, H. Wang, R. L. White, F. Drymiotis, M. Kaviany and G. Jeffrey Snyder, "Temperature-dependent band gap in PbX (X = S, Se, Te)" Appl. Phys. Lett.103, 262109 (2013).

[9] J. P. Heremans, V. Jovovic, E. S. Toberer, A. Saramat,K. Kuro saki, A. Charoenphakdee, S. Yamanakaand G. J. Snyder, "Enhancement of thermoelectric efficiency in PbTe by distortion of the electronic density of states. "Science 321, 554 (2008).

[10] Z. Tian, J. Garg, K. Esfarjani, T. Shiga, J. Shiomi and G.Chen, "Phonon conduction in PbSe, PbTe, and $PbTe_{1-x}Se_x$ from first-principles calculations." Phys. Rev. B 85, 184303 (2012).

[11] E. S. Bozin, C. D. Malliakas, P. Souvatzis, T. Proffen, N. A.Spaldin, M. G. Kanatzidis, and S. J. L. Billinge, "Entropically stabilized local dipole formation in lead chalcogenides" Science 330,1660 (2010).

[12] O. Delaire, J. Ma, K. Marty, A. F. May, M. A. McGuire, M.-H.Du, D. J. Singh, A. Podlesnyak, G. Ehlers, M. D. Lumsden, and B. C. Sales, "Giant a harmonic phonon scattering in PbTe" Nat. Mater. 10, 614 (2011).

[13] S. Kastbjerg, N. Bindzus, M. Sondergaard, S. Johnsen, N. Lock,M. Christensen, M. Takata, M. A. Spackman, and B. B. Iversen, "Carrier concentration dependence of structural disorder in thermoelectric $Sn_{1-x}Te$." Adv. Func. Mater. 23, 5477 (2013).

[14] T. Keiber, F. Bridges, and B. C. Sales, "Lead is not off center in PbTe: the importance of r-space phase information in extended x-ray absorption fine structure spectroscopy" Phys. Rev. Lett. 111, 095504 (2013).

[15] H. Kim and M. Kaviany, "Effect of thermal disorder on high figure of merit in PbTe." Phys. Rev. B **86**, (2012), 045213.

[16] Y. K. Kurosaki, "Thermoelectric properties of Tl_9BiTe_6," Journal of Alloys and Compounds, (2003), 275–278.

[17] H. K. Cheriyedath Raj Sankar, "Thermoelectric Properties of $TlGdQ_2$(Q = Se, Te) and Tl_9GdTe_6," Journal of Electronic Materials, **41**, (2012), 1662-1666.

[18] H. Unuma, N. Shigetsuka, M. Takahashi, "Synthesis and characterization of polythiophene/Bi_2Te_3 nano-composite thermoelectric material." J. Mater. Sci. Lett. **17**, (1998), 1055.

[19] H.J. Goldsmid, J.W. Sharp, "Estimation of the thermal band gap of a semiconductor from Seebeck measurements." J. Electron. Mater.**28**, (1999), 869-872.

[20] K.F. Hsu, S. Loo, F. Guo, W Chen, J.S. Dyck, C. Uher, T. Hogan, E.K. Polychroniadis, M.g. Kanatzidis, "Thermoelectric properties of Zn_4Sb_3 composites with incomplete reaction."Nature **489**, (2012), 414.

[21] Y. K. Kurosaki, "Thermoelectric properties of Tl_9BiTe_6," Journal of Alloys and Compounds, (2003), 275–278.

[22] S. Bangarigadu-Sansay, C.R. Sankar, P. Schlender, H. Klienke, J. Alloys and compounds **594**, (2013), 126.

[23] B.A. Kuropaatawa, A. Assoud, H. Kleinke, J. Alloys and Compounds **509**, (2011), 6768.

[24] Y. K. Kurosaki, "Thermoelectric properties of Tl_9BiTe_6," Journal of Alloys and Compounds. (2003), 275.

[25] S.Y. Wang, G.J. Tan, W.j. Xie, G. Zheng, H. Li, J.H. Yang, and X.F. Tang, "Enhanced thermoelectric properties of $Bi_2(Te_{1-x}Se_x)_3$-based compounds as n-type legs for low-temperature power generation." J. Mater. Chem. **22**, (2012), 20943.

[26] H. Wang, A.D. Lalonde, Y. Pie, and G.J Synder, "The criteria for beneficial disorder in thermoelectric solid solutions."Adv. Funct. Mater.**23**, (2013), 1586.

[27] Z. Cai, L. Guo, X. Xu, Y. Yan, K. Peng, G. Wang, and X Zhou, "Effect of Sn doping in $(Bi_{0.25}Sb_{0.75})_{2-x}$ Sn_x Te_3 $(0 \leq x \leq 0.1)$ on thermoelectric performance." J. Electronic Mater. **45**, (2016), 1441.

[28] K.T. Kim, T.S. Lim, G.H. Ha, "Enhanced thermoelectric figure-of-merit in Bi-Sb-Te nanocomposites with homogenously dispersed oxide ceramic ZrO_2 nanoparticles" Rev. on Advanced Materials Science **28**, (2011), 196.

[29] Wiqar H Shah, Aqeel Khan, Waqas Khan, Waqar Adil Syed, "Optimization of power factor in Sn doped Tl_{10-x} Sn_xTe_6 thermoelectric chalcogenide nano-materials." Chalcogenide Lett. **14**, (2017), 61.

Chapter # 04

Enhancement of Power Factor by Sb Doped $Tl_{10-x}Sb_xTe_6$ in Chalcogenide System

INTRODUCTION

Recent issues on rising temperature due to global warming emphasize the inhibition of carbon discharge and change in energy direction which determines the better effects of climate [1-2]. Therefore, research on renewable energy sources such as wind, solar and geothermal has pulled much attention for the last two decades. Especially, geothermal energy is the internal heat generated in the Earth's interior near-room-temperature regime (150-400^{0}C), which can be widely used to recover waste heat and utilize it for power generation [3-4]. However, the extensive use of thermoelectric materials is limited by low conversion thermoelectric efficiency. It is related to dimensionless quantity i.e. $ZT = S_b^2\sigma$ where S, σ, κ and T are the Seebeck Coefficient, electrical conductivity, thermal conductivity, and absolute temperature, respectively [5].

Interestingly, the efficient way to increase the ZT value is determined by a combination of two major factors; electrical transport should be high, characterized by power factor (S and glass-like thermal transport. Some of the compounds ($S_b^2\sigma$) which demonstrate high ZT at mid-range temperature have been achieved in lead chalcogenide, which not only contains toxic lead (Pb) but also encompasses less abundant tellurium (Te) [6]. The scarcity of Te implies to search for new earth-abundant elements that could lead to large ZT [7], near-room-temperature through innovative approaches such as defect structure engineering [8], band convergence [9], nano-structuring [10], and phonon glass electron-crystal [11].

In this chapter, we will measure the different properties of Sn (Tin) doped thallium Telluride ($Tl_{10-x}Sb_xTe_6$) nanostructured scheme. It is synthesized by the ball milling method or mechanical milling. The XRD shows the crystal construction information and phase origin. The EDX shows the percentage components in the compound. The SEM shows the morphology of the nanoparticles of the compounds. Lastly, fixed with "Sn" dopants at dissimilar absorptions and the explanations display that electrical and thermal possessions are pretentious. Seebeck coefficient and electrical conductivity were measured from the four probes resistivity investigational method which had two standard probe computation schemes, respectively. Power

factor (PF) was calculated from Seebeck coefficient and electrical conductivity. So that the Seebeck coefficient is raised as the temperature of different concentrations of the compound is increased which is shown in table and figure.

4. Results and Discussions:

4.1 X-Ray Diffraction

Most valuable method for characterizing structural features such as size of particle, the interatomic distance, and inter-planer spacing. XRD data used through Debye Scherrer's formula determined the size of particle of $Tl_{10-x}Sb_xTe_6$ nano-particle.

$$D = k\lambda/\beta\cos\theta \quad \text{..... (4.1)}$$

Where, size of particle or crystalline size is represented by "D", shape factor is represented by k = 0.9, λ shows the incoming X-ray wavelength {(λ=1.54056 Å)}, denotes the angle of peak in radian is represented by θ and β represents full width at half maximum (FWHM) of the primary peak. The following mathematical formula may be used to compute FWHM:

$$B = \frac{1}{2}(2\theta_2 - 2\theta_1)$$

$$B=(\theta_2 - \theta_1) \quad \text{..... (4.2)}$$

As a result, the crystallite size was observed between 25 nm and 19 nm. 8.84 Å shows the value of the lattice constant. The average particle size was found to be 21 nm, with various diffraction angles as indicated in Table 4.1. The XRD spectra XRD $Tl_{10-x}Sb_xTe_6$ (x=1.00, 1.25, 1.50, 1.75, 2.00) of the nano-particles were analyzed by *X'pert High Score Software* with *Reference card: 01-084-2449.* For XRD $Tl_{10-x}Sb_xTe_6$ (x=1.00, 1.25, 1.50, 1.75, 2.00) nano-particles, the diffraction peak at 23.3^0 (121), 29^0 (120), 31^0 (212), 32^0 (130), 34^0 (024), 40^0 (224), 42^0 (006), 46^0 (240), 47^0 (413), 50^0 (044) and 53^0(136) planes recognized the tetragonal crystal structure.

$Tl_{10-x}Sb_xTe_6$ nano-particles were integrated in the following ratios: (x= 1, 1.25, 1.50, 1.75, 2). The crystallite size reduces as the ratio 'x' grows owing to the contraction of radii $(Tl^+)_9\,Sb^{3+}(Te^{2-})_6$. The x-ray diffraction patterns of $Tl_{10-x}Sb_xTe_6$ are shown in Fig 4.1. These patterns show that each of the peaks is comparable to those of $Tl_{10-x}Bi_xTe_6$, with no other impurity diffraction peaks found [12]. As a result, all peaks are measured in accordance with other materials' intensities. That is, dependent on input elements, the volume of the unit cell reveals appropriate shifts. These data

reveal a satisfactory reaction outcome and do not show any impurity in sample therefore no additional peaks are visible.

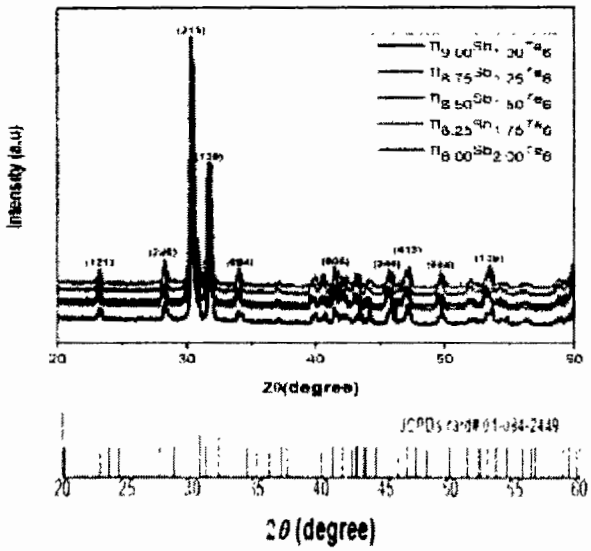

Figure 4.1: XRD $Tl_{10-x}Sb_xTe_6$ (x=1.00, 1.25, 1.50, 1.75, 2.00).

Table 4.1: XRD $Tl_{10-x}Sb_xTe_6$ (x=1.00, 1.25, 1.50, 1.75, 2.00).

24.247	A=b=8.8931 C=13.0052	1004.521
21.795	A=b=8.84510 C=13.07515	1023.925
21.180	A=b=8.82510 C=13.0010	1013.425
21.128	A=b=8.81010 C=13.0010	1009.091
20.455	A=b=8.84814 C=13.16215	1022.712

4.2 Scanning Electron Microscope

This tool is studying the shapes and surfaces of nano-materials and bulk materials. It's also utilized to figure out how to determine nano-particles "surface morphology", "size of particle" and "shape". SEM operates primarily in the reflection mode with resolution ranging from ~100 nm to ~1000 nm [13]. SEM images of Tl_9SbTe_6 bulk compound are shown in Fig 4.2. The average size of particle decreases with increasing "Sb" content as seen by the SEM image in which the structure is crystal has a size of 20 μm.

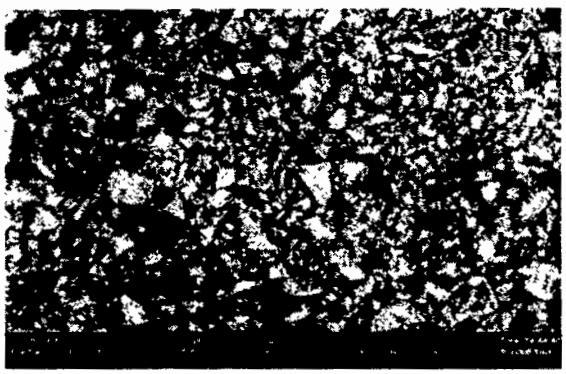

Figure 4.2: SEM image of $Tl_9Sb_1Te_6$ compound at 20 μm scale and 220X magnification.

4.3 Energy Dispersive X-Ray Analysis

This technique is incapable of determining the precise ratio of components in the last product individually, any encouraging elemental investigation is performed to supplement the diffraction determination methods. When it comes to determining composition in solid state material. This technique is a useful method that performs similarly to scanning electron microscopy. In general, it is an elemental analysis technique for elaborating a compound composition that provides an exact measurement. It may also provide quantitative, percentages or ratios of the elements included within those elements in compounds. The Tl_9SbTe_6 sample contains an unidentified thallium rich (25.8 % Te, 69.9 % Tl, and 4.2 % Sb). The atomic percent at various places of numerous crystals for a particular specimen has been normal and linked to the nominated atomic percent of the relevant compound for every element.

It is noted that "Sb" concentration with the Tl: Te ratio appears to be slightly similar in the spectra (by a few percent) as shown in Fig. 4.3. Another set of spectra can be visible in this region, which demonstrates the collection from scan region of other information in the sample which can be pieces of glass or the carbon tape. Tl_9SbTe_6 has lately been studied using a full-changing vacuum created by an extremist bladed polymer window with carbon. For peak fitting, in order to analyze the spectrum, the computer software (EDAX) generation along with a modular less ZAF fit purpose. The electron beam is in the energy scope of 20 to 25 eV and the mean collection collected time is 30 seconds within the specific region of compound and at least three scan points per sample. The EDX system used by the University of Waterloo is an EDAX Pegasus 120 detector in an advanced dynamic vacuum.

Each sample is subjected to a minimum of one afloat region scan and up to six incomplete area or elemental scans using an electron beam with an energy between 20 and 25 eV during the analysis process and on average data is collected in 30-second intervals.

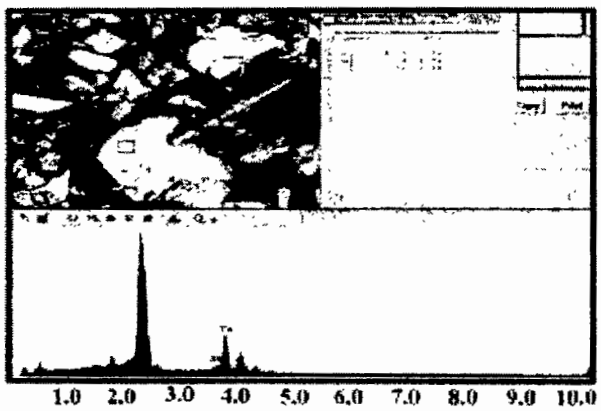

Figure 4.3: Energy Dispersive X-Ray analysis screenshot of ($Tl_{10-x}Sb_xTe_6$).

Table 4.2: Energy Dispersive X-Ray analysis screenshot of ($Tl_{10-x}Sb_xTe_6$)

Element	Wt %	At %
Sb	8.26	5.96
Te	58.22	65.95
Tl	49.96	59.99

4.4 Thermal analysis of Tl_9SbTe_6

Tl_9SbTe_6 has been amalgamate in axenic phase for thermal investigation. Differential Scanning Calorimeter (DSC) measurement has been carried out at slower rate of 2 °/min (instead of the usual 10°/min) from 300 K to 673 K in an effort to determine whether the has any developmental deficiencies as the temperature rises.

The DSC result of Tl_9SbTe_6 shows that is a large exothermic peak at 500 K which indicates that the bismuth did not show phase transition in the existing solid state. Fig. 4.4 shows a very small peak for Tl_9BiTe_6 type compound observed in DSC studies by the Kleinke research group. Examples included $Tl_{8.0}Sn_{0.5}Bi_{1.5}Te_6$ a 533 K showed an exothermic peak less than 10% as intense as its melting peak at 553 K and around Tl_9BiTe_6 at (593 K) indicating a minor fluctuation. This is same thing that happens in certain Tl_9LnTe_6 experiments. According to previous research, a solid-solid phase transition is a reasonable hypothesis and has been found in other ternary system such as $TlSbTe_2$ at low temperatures [14].

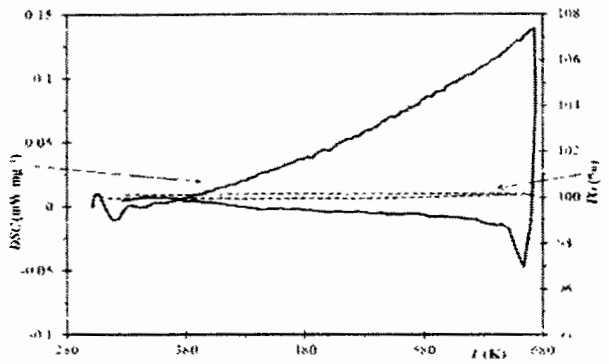

Figure 4.4: Thermal analysis of Tl_9BiTe_6

Tl_9SbTe_6 compound has a peak in both heating and cooling cycles. It was found at 510 k with $^1/_4$ intensity in the heating cycle and the change appears to be fully reversible as shown in Fig. 4.5. Peak is caused by excess noise from the furnace and oxidation of the sample, but no additional data could be generated. Quenching experiments are currently being carried out to freeze the samples in order to demonstrate that the "Sb" compound has high-temperature phase.

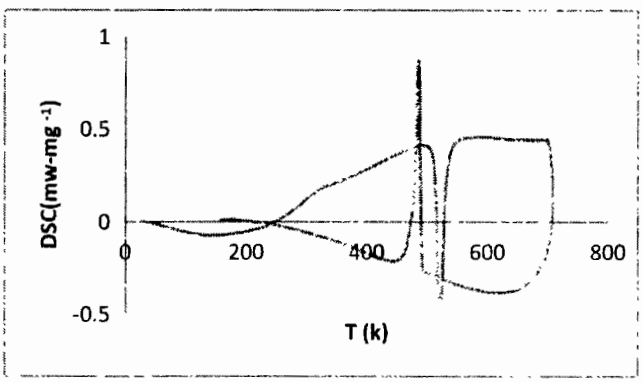

Figure 4.5: Thermal analysis of Tl_9SbTe_6

4.5 Electrical Conductivity Measurements

The sample studied in these experiments belongs to the general family of "Sb" doped $Tl_{10}Te_6$, which we have investigated from the point of determining the consequence of "Sb" doping in a parent compound which determines the electrical and thermal properties.

As a part of this study, we investigated the outcomes of "Sb" doping in parent samples on the semiconductor and metallic boundary. The experiment was carried out in a commercial oxford instrument cryostat capable of temperature control to

within 0.5 K. Silver points were used to make the standard 4-probe contacts that were tested at room temperature and only experiments were conducted only when the resistance was low enough. The typical current used was 0.1 mA . A four-probe resistivity method was used to analyze the electrical properties of tin-doped thallium telluride nano structural system low the influence of temperature variations ranging from 300 K to 650 K. The electrical conductivity "**σ**" for $Tl_{10-x}Sb_xTe_6$ samples ($1.0 \leq x \leq 2.0$) between 300 K and 550 K as shown in Fig. 4.6. $Tl_{10-x}Sb_xTe_6$ samples and $Tl_9Bi_xTe_6$ system demonstrated the similar trend were decreasing the electrical conductivity with increasing temperature. Similarly, the activity of "Sb" doped system is accurate both for intrinsic semiconductors with x= 1 up to 2 such as the sample $Tl_{10-x}Sn_xTe_6$ and $Tl_{10-x}Bi_xTe_6$ [15-17]. The p-type conductivity is indicated by electrical conductivity decreasing with temperature. According to Fig. 4.6 at 300 K the electrical conductivity of $Tl_9Sb_1Te_6$ reaches its maximum value of 700 $\Omega^{-1}cm^{-1}$. It then gradually lower, until it reaches 500 K temperature, where it is 661 $\Omega^{-1}cm^{-1}$. The electrical conductivity of $Tl_{10-x}Sb_xTe_6$ decreases as x concentration increases. At a temperature of 300K, the electrical conductivity dropped from 700 $\Omega^{-1}cm^{-1}$ to 656 $\Omega^{-1}cm^{-1}$ as x concentrations varied from 1 to 2. It reduced from 661 $\Omega^{-1}cm^{-1}$ with x = 1 to 615 $\Omega^{-1}cm^{-1}$ with x = 2 in the identical way at 550 K.

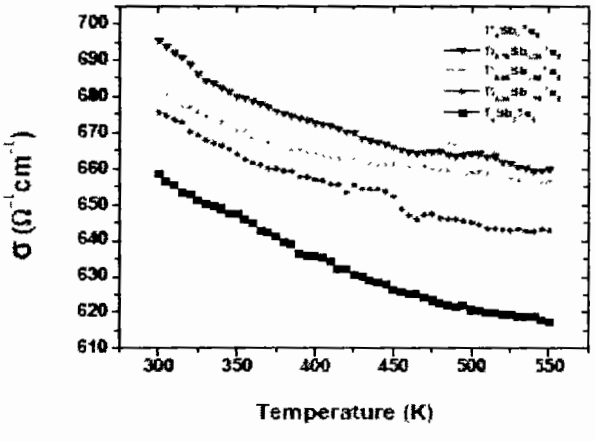

Figure 4.6: Electrical conductivity of $Tl_{10-x}Sb_xTe_6$ at 300 K, 400 K, and 550 K.

Table 4.3: Electrical conductivity of $Tl_{10-x}Sb_xTe_6$ at 300 K, 400 K, and 550 K.

	Electrical conductivity ($\Omega^{-1}cm^{-1}$) At 300	Electrical conductivity ($\Omega^{-1}cm^{-1}$) At 350	Electrical conductivity ($\Omega^{-1}cm^{-1}$) At 400	Electrical conductivity ($\Omega^{-1}cm^{-1}$) At 450	Electrical conductivity ($\Omega^{-1}cm^{-1}$) At 500	Electrical conductivity ($\Omega^{-1}cm^{-1}$) At 550
$Tl_8Sb_2Te_6$	700	685	675	670	665	661
$Tl_{8.75}Sb_{1.25}Te_6$	693	680	673	669	663	657
$Tl_{8.5}Sb_{1.5}Te_6$	679	670	665	660	653	653
$Tl_{8.25}Sb_{1.75}Te_6$	672	660	658	648	640	640
$Tl_8Sb_2Te_6$	656	650	635	625	620	615

4.6 Seebeck Coefficient (S) Measurements

The Seebeck coefficient is a critical method for determining the absolute properties of two materials. Seebeck coefficient expresses the relationship between an applied temperature gradient and the resulting electric field gradient. In another way, the temperature fluctuated constantly which helped to Seebeck coefficient curve [18] can be derived from the slope of the voltage vs. temperature difference. However, the Seebeck coefficient always rises with temperature in presence of nano inclusion radius. The results of $Tl_{10-x}Sb_xTe_6$ nanomaterial were compared to those of other thermoelectric materials using a different ratio of 'x'.

Thermoelectric properties of $Tl_{10-x}Sb_xTe_6$ nanoparticles at various Sb concentrations (x=1, 1.25, 1.50, 1.75, 2) are depicted in Fig. 4.6. Temperature range from 315 K to 550 K and doping concentration (Ti: Sb) both increase the Seebeck coefficient. All the same, $Tl_8Sb_2Te_6$ sample exhibited the highest Seebeck coefficient, S = 80.95 μVK^{-1} at 300 K, indicating that sample contains intermediate carriers. Additionally, the "Sb" deficiency and the number of P-type charge carriers increase, leading to an overall decrease in the Seebeck coefficient (81 μVK^{-1} when x = 2 down to 67 μVK^{-1} for x = 1). Even with a 3 % of margin of error, the Seebeck values are different from the other sample x = 1 & 1.25 (at 82 vs 82.9 μVK^{-1}). Overall composition, temperature has a linear effect on the Seebeck coefficient. Because of a lack of the P-type such heavy metal tellurides, as well as $Tl_{10-x}Ln_xTe_6$ series and Tl_9BiTe_6, have a lot of charge carriers (> 10^{19} cm^{-3}). Seebeck coefficient of $Tl_{10-x}Ln_xTe_6$ series (Ln = La, Ce, Pr, Nd, Sm, Gd, Tb) is about the same as $Tl_{10-x}Sb_xTe_6$ [19], which increases with temperature due to this activity of smaller energy band gaps (E_g), which form it simple for electrons to move from the valance band to the

conduction band, which is beneficial for increasing electrical conductivity (σ) [20]. In this case, the Seebeck has same kind of gap.

Generally, higher electrical conductivity samples have a lower Seebeck coefficient. All samples of $Tl_{10-x}Sb_xTe_6$ are analyzed to improve the thermoelectric properties. Using the dominant carrier in the holes or compound has resulted in a positive 'S' value for all samples. So that the Seebeck coefficient (S) increases as the temperature rises.

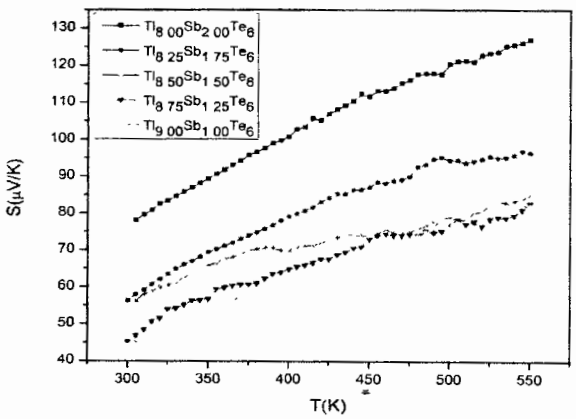

Figure 4.7: Seebeck coefficient of $Tl_{10-x}Sb_xTe_6$ with x varying between 1 and 2.

Table 4.4: Seebeck Coefficient of $Tl_{10-x}Sb_xTe_6$ at 300 K, 400 K, and 550 K.

	46	55	60	65	70	82
	50	58	65	68	72	83
	58	65	70	72	75	85
	60	70	80	90	92	96
	80	90	100	110	115	127

4.7 Power Factor

A power factor reveals that it rises due to the Seebeck coefficient rising with temperature. As discussed in chapter 1, the power factor is directly related to the square of the Seebeck coefficient; in addition, the electrical conductivity also changes with temperature. The lowest power factor is 1.9 $\mu W cm^{-2}K^{-2}$ was found for "Sn" = 1 and the highest power factor 7.579 $\mu W cm^{-2}K^{-2}$ was found for "Sb" = 1.75 at temperature 300 K, whereas the power factor for "Sb" = 2 is 3.639 $\mu W cm^{-2}K^{-2}$ which improves with temperature. This low power factor is due to $Tl_8Sb_2Te_6$

extremely low electrical conductivity which is important in power factor research. Material that contains "Sb" indicates a clear high value between 1.29 $\mu W\text{-}cm^{-1}K^{-2}$ and 9.78 $\mu W\text{-}cm^{-1}K^{-2}$ respectively than un-doped sample at 300 K and 550 K. As shown in Fig 4.8, the specimen with x = 1.0,1.25 and 1.50 exhibit an infinitesimal increase as decreasing the temperature dependence and collective at same point at 4.2 $\mu W\text{-}cm^{-1}K^{-2}$. All "Sb" samples examined in this study demonstrated improved power factor performance. The Tl_9LnTe_6 series has been reported to show a range of power factor values between 2.9 and 4.7 $\mu Wcm^{-1}K^{-2}$at 550K due to the doping of various elements namely (Ce, Pr). The power factor at "x"= 2.05 for ternary group ($Tl_{10}SbTe_6$) substitute of "Sb" is 3.8-4.97 $\mu Wcm^{-1}K^{-2}$ at 320 K to 685 K respectively [21] whither, it is a relatively small value which differentiates to the one reported in the current research, i.e. for $Tl_8Sb_2Te_6$ power factor is 8.98 $\mu Wcm^{-1}K^{-2}$ at 550 K.

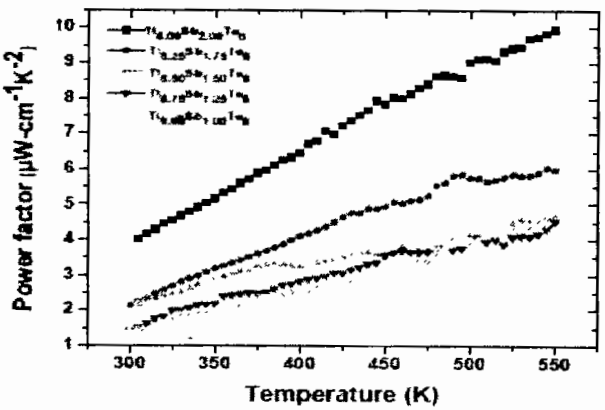

Figure 4.8: Power Factor of $Tl_{10-x}Sb_xTe_6$ at 300 K, 400 K and 550 K.

Table 4.5: Power Factor of $Tl_{10-x}Sb_xTe_6$ at 300 K, 400 K and 550 K.

	1.3	2.2	2.5	3.6	4.1	4.3
	1.5	2 5	3.2	3 5	3 8	4 5
	2.2	3.1	3.25	3.45	3.5	5.1
	2.2	3.25	4.3	4.5	5.5	6.2
	4.3	5.2	6.5	7.3	8.5	10.2

4.8 Conclusion

$Tl_{10-x}Sb_xTe_6$ compound, doped with p-type antimony (Sb) constituent on binary Thallium Telluride group was studied for thermoelectric properties. Ball milling techniques were used to prepare Thallium Antimony Telluride nano-crystals, which is then hot-pressed to make a dense pellet to determine its thermoelectric property at various concentration of x = 1, 1.25, 1.50, 1.75, 2. Scanning electron microscopy (SEM), X-Rays diffraction (XRD), and energy Dispersive X-rays Spectroscope are used to characterize the structure of ($Tl_{10-x}Sb_xTe_6$), with the beat results obtained for the 'Sb' sample. XRD pattern shows tetragonal structure of thallium antimony telluride nano-crystal with space group (*I4/mcm*).

As shown by XRD peaks, it is observed that the particle size decreases as the ratio 'x' is increased. SEM image results resemble crystal structure and the weight and atomic percent of $Tl_{10-x}Sb_xTe_6$ are shown in EDX result. Differential scanning calorimeter (DSC) whether a compound has any developmental deficiency as 300 K to 673 K.

The 'Sb' system on the cold-pressed and hot-pressed $Tl_{10-x}Sb_xTe_6$, i.e. at 300 K has achieved a significant increase in the Seebeck coefficient (S). $Tl_8Sb_2Te_6$ had an 'S' value of 81 μVK^{-1} while 126 μVK^{-1} at 500 K was observed for it at the same temperature. As a result, as the 'Sb' value increases, the electrical conductivity decreases, and Seebeck coefficient rises. All of these compounds indicate a positive Seebeck coefficient due to the p-type behavior. We have noticed that the value of 'S' in 'Sb' based compounds rise. The amount of 'Sb' contents in the parent compound increases. We have concluded that a high efficiency thermoelectric generator could be made with the help of "Sb" based compounds because their values were higher than those of other compounds.

4.9 References

[1] Lon E Bell. "Cooling, heating, generating power, and recovering waste heat with thermoelectric systems." Science **321**, (2008), 1457-1461.

[2] T Kajikawa. "Thermoelectric power generation system recovering industrial waste heat." Thermoelectric Handbook: Macro to Nano. CRC/Taylor & Francis., DM Rowe (2006), 1-50.

[3] W. Zhao, Z. Liu, Z. Sun, Q. Zhang, P. Wei, X. Mu, H. Zhou "Superparamagnetic enhancement of thermoelectric performance." Nature **549**, (2017), 247-251.

[4] Wenyu Zhao, Zhiyuan Liu, Ping Wei, Qingjie Zhang, Wanting Zhu, Xianli Su, Xinfeng Tang, et al. "Magneto electric interaction and transport behaviors in magnetic nanocomposite thermoelectric materials." Nature Nanotechnology **12**, (2017), 55-60.

[5] Goldsmid, H. J. "Conversion efficiency and figure-of-merit. Handbook of thermoelectric." Rowe, D. M., Ed.; CRC Press: Boca Raton, (1995), 19–26.

[6] Pei, Yanzhong, Aaron Lalonde, Shiho Iwanaga, and G. Jeffrey Snyder. "High thermoelectric figure of merit in heavy hole dominated PbTe." Energy & Environmental Science **4**, (2011), 2085-2089.

[7] Saneyuki Ohno, Umut Aydemir, Maximilian Amsler, Jan-Hendrik Pöhls, Sevan Chanakian, Alex Zevalkink, Mary Anne White, Sabah K. Bux, Chris Wolverton, and G. Jeffrey Snyder. "Achieving zT> 1 in inexpensive Zintl Phase $Ca_9Zn_{4+x}Sb_9$ by phase boundary mapping." Advanced Functional Materials **27**, (2017), 1606361.

[8] Z. Li, C. Xiao, H. Zhu, and Y. Xie, "Defect chemistry for thermoelectric materials." J. Am. Chem. Soc., (2016), 14810–14819.

[9] Y. Pei, H. Wang, and G. J. Snyder, "Band engineering of thermoelectric materials." Adv. Mater.,**24**, (2012), 6125–6135.

[10] Y. Lan, A. J. Minnich, G. Chen, and Z. F. Ren, "Enhancement of thermoelectric figure of merit by a bulk nanostructuring approach." Adv. Funct. Mater,**20**, (2010), 357–376.

[11] D. M. Rowe, "CRC Handbook of thermoelectric." CRC Press, New York, (1995).

[12] R. Chen, A. I. Hochbaum, R. D. Delgado, W. Liang, E. C. Garnett, M. Najarian, A. Majumdar, P. Yang, "Enhanced thermoelectric performance in rough silicon nanowires." (2008).

[13] Holger. K. Quansheng Guo, "Thermoelectric properties of hot-pressed Tl_9LnTe_6 (Ln = La, Ce, Pr, Nd)," Journal of Alloys and Compounds, **630**, (2015), 37–42.

[14] H. Czichos, T. Saito, and L. R. Smith, "Springer handbook of materials measurement methods." (Springer Science & Business Media), (2006).

[15] Lin, H. Markiewicz, R. S. Wray, L. A. Fu, L.; Hasan, M. Z. Bansil, "Single Dirac cone topological surface states in the $tlbise_2$ class of the topological semiconductor." A., Phys. Rev. Lett. (2010), 036401-036404.

[16] A. I. Boukai, Y. Bunimovich, J. Tahir-Kheli, J. Yu, W. A. I. Goddard, J. R. Heath, "Silicon nanowires as efficient thermoelectric materials." Nature **451**, (2008), 168.

[17] R. Venkatasubramanian, E. Siivola, T. Colpitts, B. O'Quinn, "Thin-film thermoelectric devices with high room-temperature figures of merit." Nature **413**, (2001), 597.

[18] B. Poudel, Q. Hao, Y. Ma, A. Minnich, A. Muto, Y.C. Lan, B. Yu, X. Yan, D. Z. Wang, D. Vashaee, "High-Thermoelectric Performance of Nanostructured Bismuth Antimony Telluride Bulk Alloys." Science **320**, (2008), 634.

[19] A. Shakouri, C. Labounty, P. Abraham, J. Piprek, J. E. Bowers, "Enhanced thermionic emission cooling in high barrier super lattice heterostructures." Materials Research Society Proceedings **545**, (1999), 449.

[20] D. Vashaee, A. Shakouri, "Improved thermoelectric power factor in metal-based superlattices." Phys. Rev. Lett. **92**, (2004), 106103.

[21] G. J. Snyder, E. S. Toberer, "Complex thermoelectric materials." Nat. Mater. **7**, (2008), 105.

[22] H. K. Cheriyedath Raj Sankar, "Thermoelectric properties of $TlGdQ_2$ (Q = Se, Te) and Tl_9GdTe_6," Journal of Electronic Materials, **41**, (1012), 1662-1666.

[23] Bangarigadu-S., Savitree, et al. "Thermoelectric Properties of $Tl_{10-x}Ln_xTe_6$, with Ln= Ce, Pr, Nd, Sm, Gd, Tb, Dy, Ho and Er, and $0.25 \leqslant x \leqslant 1.32$." Journal of Alloys and Compounds, vol. **549**, (2013), 126-134.

Chapter # 05

Effect of Pb Doping on Seebeck co-efficient and Transport Properties OF $Tl_{8.67}Pb_XSb_{1.33-X}Te_6$ Chalcogenide System

INTRODUCTION

At the moment, entropy engineering has emerged as innovative and creative management to decrease thermal conductivity through manipulating configurational entropies. When multiple components share the same atomic sites in the crystal, increases the configuration entropy. Multicomponent chalcogenide like $(SnTe)_{1-2x}(SnSe)_x(SnS)_x$, $(GeTe)_{1-2x}(GeSe)_x(GeS)_x$ and $(PbTe)_{1-2x}(PbSe)_x(PbS)_x$ are very well renowned pseudo ternary systems which exhibit low lattice thermal conductivity. It occurs because its increases in the entropy arise from point defect phonon scattering, mass fluctuation of different elements and strain-induced resulting from atomic size mismatch [1-5]. Additionally, the large atomic size is different between the essential atoms that can be locally synthesised in every laboratory easily. Moreover, the large size mismatch of Te and S atoms would generate an off-centring of S atoms which introduces dipole moment and soft phonon modes in the crystal. As a result, the soft phonons effectively scatter heat-carrying acoustics phonons and reduces the lattice thermal conductivity significantly [6]. Along with entropy engineering, the Rashba effect has an additional effect in the fields of thermoelectricity through the spin-orbit coupling (SOC) mechanism in the charge carrier transport phenomenon [7]. The Rashba spin splitting leads to a distinctive feature in the electronic density of states (DOS) due to the unique Fermi surface topology [8]. Consequently, the power factor is found ($S^2\sigma$) to be large because of the sharp peak in DOS [9]. Thus, the Rashba spin splitting can potentially be a very effective mechanism for thermoelectricity.
Chalcogenide families such as PbTe and its solid solution with PbSe and PbS are well-known semiconductors to show excellent thermoelectric efficiency [10].

In this chapter, we will analyze different properties of Pb (Lead) doped thallium telluride ($Tl_{8\,67}\ Pb_xSb_{1\,33-x}Te_6$) nano-structured scheme, synthesized by ball milling techniques. The XRD data depicts the crystal structure and phase of the understudy nano-system. The EDX data shows the percentage composition as well as the elemental analysis of the sample, whereas the SEM depicts the morphology of the nanoparticles. Lastly, fixed with "Pb" dopants at dissimilar absorptions and the explanations display that electrical and thermal possessions are pretentious. Electrical

conductivity was calculated from the four probe resistivity investigational method. Seebeck was calculated by the two probe resistivity method. Seebeck coefficient and electrical conductivity can help to measure the power factor. As a result, the Seebeck coefficient is increased as the temperature increases for different compositions.

5. Results and Discussions:

5.1 X-Ray Diffraction

Most valuable tool to look at the structural properties of a material. It can be used for determining the phase structure, crystallite size, plane orientation, and more. It details the grain's sizes, their position, and the miller indices in detail. Additionally, it also shows atomic spacing. This entire set of information is vital when studying the structure of the materials [11]. By using Debye Scherer's formula is used to figure out crystallite size of $Tl_{8\,67}Pb_xSb_{1\,33-x}Te_6$ compound as follows:

$$D = k\lambda/\beta cos\theta_B \quad (5.1)$$

Where "D" indicates the crystallite size, 'k' indicates a constant with a 0.91 value,"λ" indicates the wavelength and "θ" indicates Bragg's angle and 'β' indicates measuring the full width half maximum (FWHM). The particle Crystallite size is approximately 63 nm on average for the compound studied. $Tl_{8\,67}Pb_xSb_{1\,33-x}Te_6$ nanoparticles have a concentration ratio of X=0.61, 0.63, 0.65, 0.67, 0.68, 0.70.

The pattern of peaks in the XRD can be used to confirm the purity of samples that appear exactly like the peaks in the XRD graph (121, 220,213,130,024). The material appears to be single crystalline with tetragonal shape.

The physical properties of the "Pb" doped $Tl_{8\,67}Pb_xSb_{1\,33-x}Te_6$ compounds series were analyzed for x=0.61, 0.63, 0.65, 0.67, 0.68, 0.70 for the variety of concentration. The powder x-rays diffraction pattern for all these compounds obtained at room temperature is illustrated in Fig. 5.1. The present study obtains the tetragonal single phase $Tl_{8\,67}Pb_xSb_{1\,33-x}Te_6$. At room temperature, observed tetragonal lattice parameters are a = 0.866 nm and c= 1.305 nm and have the same space group 14/mcm as the literature data [12].

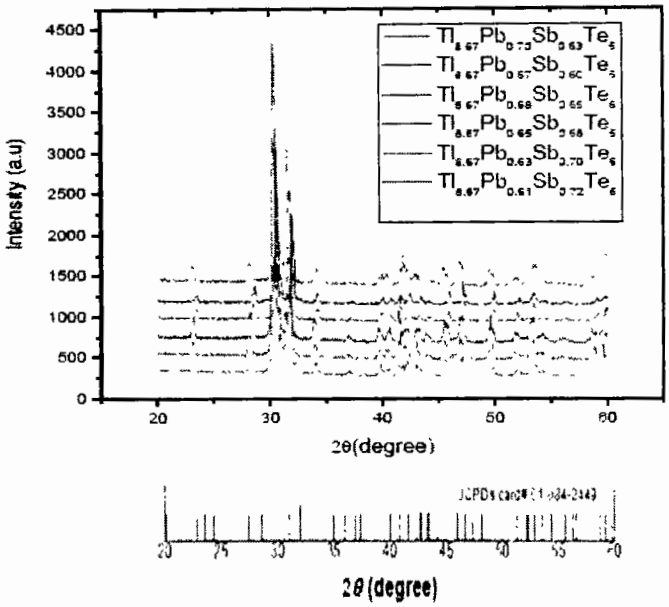

Figure 5.1 XRD $Tl_{8\,67}Pb_xSb_{1\,33-x}Te_6$ (x=1.00, 1.25, 1.50, 1.75, 2.00)

At room temperature, the EDX data collected for $Tl_{8\,67}Pb_{0\,63}Sb_{0\,70}Te_6$, are shown in Fig.5.2 to analyze the elemental and compositional in the "Pb" doped chalcogenide system, with same stoichiometric ratio as designed to all other compounds.

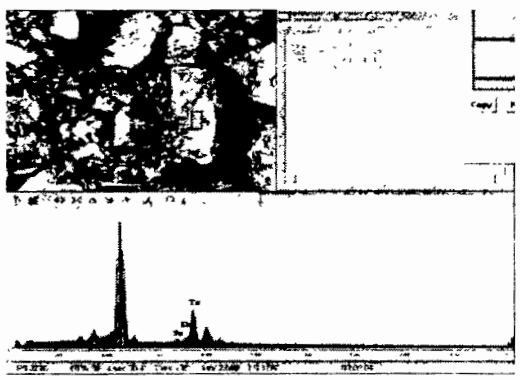

Figure 5.2: Energy Dispersive X-Ray analysis screenshot of $(Tl_{8\,67}Pb_xSb_{1\,33-x}Te_6)$.

5.2 Electrical Conductivity Measurements

In this study, overall sample has electrical conductivity decreases with temperature rises. This is because the positive coefficient of temperature demonstrates the degenerate semiconductor behavior, caused by charge carrier phonons scattering and grains boundaries effects [13].

Particularly, there is no systematic trend found of electrical conductivity variation in "Pb" doped chalcogenide system for the $Tl_{8.67}Pb_xSb_{1.33-x}Te_6$ with "Pb" concentration. The impurity in phase by oxide in the grain boundary may be responsible for decreasing the electrical conductivity in the pressure-less sintered chalcogenide system [13-16]. The electrical conductivity of the chalcogenide system is influenced by the concentration of lead doping and the grain boundary mechanism in the system.

$Tl_{8.67}Pb_xSb_{1.33-x}Te_6$ compounds with $0.61 \leq x \leq 0.70$ electrical conductivity "σ" is decreasing with a change in temperature across the total temperature reach as shown in Fig 5.3. These results are declarative of metallic conduct, indicating a high carrier concentration. As expected, an increase in doping concentration also increases the Seebeck counterpart whereas decrease in σ. At 290 K, the $Tl_{8.67}Pb_{0.70}Sb_{0.60}Te_6$ has highest value of 1650 $(\Omega\text{-cm})^{-1}$ whereas $Tl_{8.67}Pb_{0.65}Sb_{0.65}Te_6$ has the lowest with 545 $(\Omega\text{-cm})^{-1}$. The samples having x= 0.61 and 0.63 have values close to 850 and 900 $(\Omega\text{-cm})^{-1}$ respectively. For the $Tl_{8.67}Pb_{0.63}Sb_{0.70}Te_6$ compound, variations of conductivity between the hot pressed pellet and the ingot were slightly different ranging from 850 to 855 $(\Omega\text{-cm})^{-1}$ respectively at room temperature.

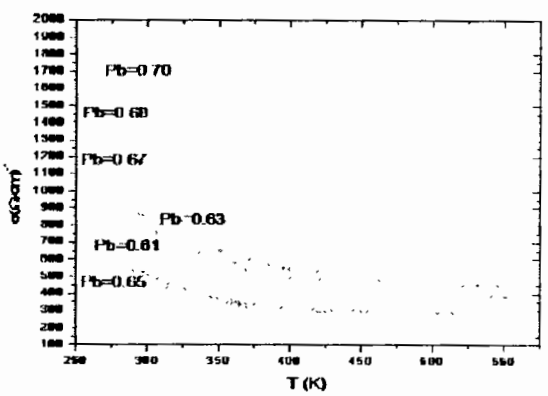

Figure 5.3: Electrical conductivity of $Tl_{8.67}Pb_xSb_{1.33-x}Te_6$ at 300 K, 400 K, and 550 K.

5.3 Seebeck Coefficient (S) Measurements

The temperature variation with the Seebeck coefficient (S) for the $Tl_{8.67}Pb_xSb_{1.33-x}Te_6$ X=0.61, 0.63, 0.65, 0.67, 0.68, 0.70 compounds showing in Fig. 5.4. for each element in compounds especially for p-type semiconductors, enhance in the positive Seebeck coefficient smoothly as the temperature increases from 300-500 K. These semiconductors have high concentration of carrier charges. The positive

thermos power of this chalcogenide system across the entire temperature range indicates that the p-type (hole) carrier's conduction dominates the thermoelectric transport in these compounds. When the amount of "Pb" increased from 0.61 to 0.65 concentration of "Pb" electron scattering is decreasing with increasing the effect of hole concentration. As a result, the thermos power is reduced. However, electron scattering in chalcogenides is enhanced due to the smaller grains created by *Pb* doping which increases thermos power and effective mass in the system [17, 18]. Seebeck coefficient, temperature, and injected charge carrier concentration can be correlated to the temperature and doping concentration "x" as shown below [19]:

$$S=\frac{8\pi^2 k_B^2 m^*}{3eh^2}.T\left(\frac{\pi}{3n}\right)^{2/3} \quad \text{..... (5.2)}$$

Where "k_B" denotes Boltzmann constant, "*e" donates* electronic charge, "*h*" denotes the Plank's constant, "m^*" denotes effective mass, and "*n*" denotes charge carrier concentration. The Seebeck coefficient is affected by two parameters such as effective mass and carrier concentration. As a result, the lower concentration of the samples (small *x, and high n*), will show a linear increase in thermos power as the temperature rises. Increasing the temperature of small *n* and large x, causes Seebeck coefficient to drop down when enough charge carriers can cross the band gap of the compound being studied. Using $E_{gap}=2eS_{max}T_{max}$ [24], a gap of 0.23 eV has to figure out for $Tl_{8.67}Pb_{0.70}Sb_{0.63}Te_6$ system.

In this research, it is found that Seebeck coefficient could be improved musing the high concentration of "Pb" in this system. Temperature affects the Seebeck coefficient which ranges from 80 to 130 $\mu V/K$. in this case, the decreasing carrier density causes a lower Fermi energy level which causes the Seebeck coefficient to increase [20].

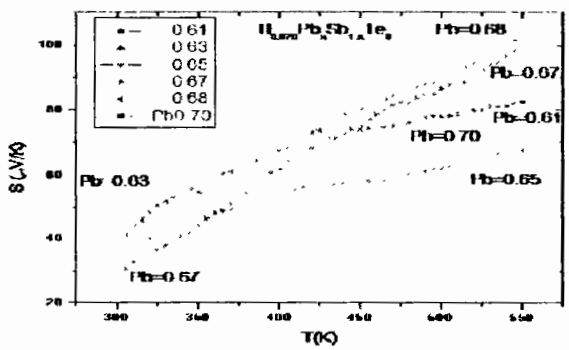

Figure 5.4: Seebeck Coefficient of $Tl_{8.67}Pb_xSb_{1.33-x}Te_6$ at 300 K, 400 K, and 550 K.

5.4 Power Factor

The electrical conductivity and Seebeck coefficient play an important role for improving the power factor (PF= $S^2\sigma$) in $Tl_{8\,67}Pb_xSb_{1\,33-x}Te_6$ (x=061, 0.63, 0.65, 0.67, 0.68 and 0.70) compound. The power factor exhibits highly irregular behavior in the presence of doping of "Pb" concentrations.

Dis connectivity between electrical conductivity and Seebeck coefficient is directly affected to improve the power factor of these compounds which defines the inversely proportional each other of these two factors. The Seebeck coefficient S can have a significant impact on power factor. Thus we must increase Seebeck S for improving the power factor (PF). We calculated the power factor using electrical conductivity and the Seebeck coefficient and the results are shown in Fig. 5.5. The power factor rises as the temperature rises. So a very complicated relationship is observed between the power factor and doping concentration of Pb. So it observed that $Tl_{8\,67}Pb_{0\,60}Sb_{0\,70}Te_6$ has the highest value at 8.56 $\mu W\text{-}cm^{-1}K^{-2}$ at 550 K and 3.525 $\mu W\text{-}cm^{-1}K^{-2}$ at 290 K whereas $Tl_{8\,67}Pb_{0\,70}Sb_{0\,60}Te_6$ has the lowest values at 1.66 $\mu W\text{-}cm^{-1}K^{-2}$, 56 $\mu W\text{-}cm^{-1}K^{-2}$ at 550 K and 1.0156 $\mu W\text{-}cm^{-1}K^{-2}$ values at 290 K among all the compounds. As previously stated, it is analyzed that lead concentration rise, resulting in the number of holes also increasing. This is supported by the current experimental trend. The Seebeck coefficient decreases and increases as the concentration x increases until the lead concentration reaches an ideal level. Seebeck coefficient rises as a result of this. The $Tl_{8\,67}Pb_{0\,70}Sb_{0\,60}Te_6$ compound is slightly temperature dependent due to large number of grain boundary scattering. The power factor increase for various dopant Agents. The following table illustrates the variation in power factor, indicating that 0.61 is 3.7 $\mu W\text{-}cm\text{-}1\text{-}K^{-2}$ dopant concentration is increased the power factor and that 0.65 is 1.27 $\mu W\text{-}cm^{-1}\text{-}K^{-2}$ dopant concentrations are decreased due to grain boundaries scattering phenomena and increase hole conduction. Lead concentration and power factor optimization have increased the complicated behavior of power factor in comparison to Temperature. The lead dopant concentration is increased the thermoelectric properties of the sample which is dependent on high Seebeck coefficient and high electrical conductivity and low thermal conductivity. The power factor PF is determined by the relationship between the Seebeck coefficient and electrical conductivity, both of which are interdependent. Because of analyzable action of power factor verse temperature, it is difficult to

determine the effective property of the thermo-electric characterizations within total system. As a result, these system exhibits random solid state phenology and show imperfectness in the crystalline materials. According to various levels of temperature of semiconductor materials, electronic behavior is another factor are various energy band gaps.

The highest value of power factor was 8.56 $\mu W\text{-}cm^{-1}\text{-}K^{-2}$ of PF at 550 K and 3.5256 $\mu Wtt\text{-}cm^{-1}\text{-}K^{-2}$ at 290 K for $Tl_{8\ 67}Pb_{0\ 60}Sb_{0\ 70}Te_6$ compound. $Tl_{8\ 67}Pb_{0\ 70}Sb_{0\ 60}Te_6$ compound had the lowest power factor with values of 1.66 56 $\mu W\text{-}cm^{-1}\text{-}K^{-2}$ at 550 K and 1.01 56 $\mu W\text{-}cm^{-1}\text{-}K^{-2}$ at 290 K. The low-temperature dependence $Tl_{8\ 67}Pb_{0\ 70}Sb_{0\ 60}Te_6$ compound is caused by a high number of grain boundary scattering [21].

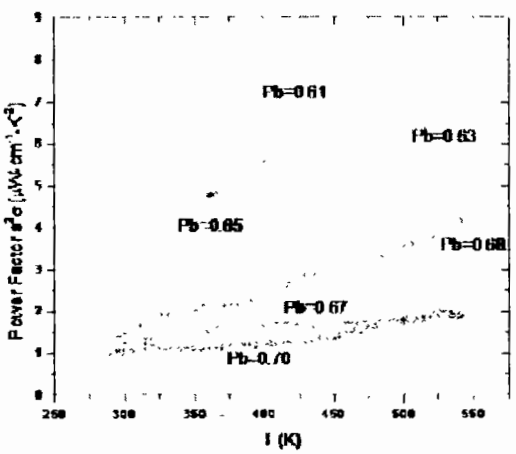

Figure 5.5: Power Factor of $Tl_{8.67}\ Pb_xSb_{1\ 33-x}Te_6$ at 300 K, 400 K, and 550 K.

.5.5 Conclusion

We synthesized various concentrations and studied the physical properties of "*Pb*" doped $Tl_{8\ 67}Pb_xSb_{1\ 33-x}Te_6$ compound series with x=0.61, 0.63, 0.65, 0.67, 0.68, 0.70. The crystal structure of $Tl_8Sb_2Te_6$ investigated by XRD confirmed that these materials are single phase which was observed with the data-based and having the identical space group the 14/mcm same asTl_5Te_3.

The thermoelectric properties were calculated between room temperature and about 550 K of polycrystalline $Tl_{8\ 67}Pb_xSb_{1\ 33-x}Te_6$ compounds. Increased hole concentration also increases the electron scattering by the Pb doped in chalcogenide system but the Seebeck coefficient is decreased by the doped tellurium telluride for higher concentrations of "Pb". However, the carrier's density will increase by the

value found above 0.65. On the other hand, the smaller grains will improve the electron scattering with high Pb concentrations. As a result, the thermos power increases. PbTe has shown that further improvements can be made to the best materials on both the micro and nano scales in different studies [21, 22].

5.6 References

[1] Subhajit Roychowdhury, Raju K. Biswas, Moinak Dutta, Swapan K. Pati, and Kanishka Biswas. "Phonon localization and entropy-driven point defects lead to ultralow thermal conductivity and enhanced thermoelectric performance in $(SnTe)_{1-2x}(SnSe)_x(SnS)_x$." ACS Energy Letters **4**, (2019), 1658-1662.

[2] Rachel J. Korkosz, Thomas C. Chasapis, Shih-han Lo, Jeff W. Doak, Yoon Jun Kim, Chun-I. Wu, Euripides Hatzikraniotis et al. "High ZT in p-type $(PbTe)_{1-2x}(PbSe)_x(PbS)_x$ thermoelectric materials." Journal of the American Chemical Society **136**, (2014), 3225-3237.

[3] Dianta Ginting, Chan-Chieh Lin, R. Lydia, Hyeon Seob So, Hosun Lee, Junpil Hwang, Woochul Kim, Rabih Al Rahal Al Orabi, and Jong-Soo Rhyee. "High thermoelectric performance in pseudo quaternary compounds of $(PbTe)_{0.95-x}(PbSe)_x(PbS)_{0.05}$ by simultaneous band convergence and nano precipitation." Acta Materialia. **131,** (2017), 98-109.

[4] Andrew Manettas, Rafael Santos, Xavier Reales Ferreres, and Sima Aminorroaya Yamini. "Thermoelectric performance of single phase p-type quaternary $(PbTe)_{0.65-x}(PbSe)_{0.35}(PbS)_x$ alloys." ACS Applied Energy Materials **1**, (2018), 1898-1903.

[5] Manisha Samanta, and Kanishka Biswas. "Low thermal conductivity and high thermoelectric performance in $(GeTe)_{1-2x}(GeSe)_x(GeS)_x$: competition between solid solution and phase separation." Journal of the American Chemical Society **139**, (2017), 9382-9391.

[6] Jeff W. Doak, Christopher Wolverton, and Vidvuds Ozoliņš. "Vibrational contributions to the phase stability of PbS-PbTe alloys." Physical Review B **92**, (2015), 174306.

[7] Wu, L.; Yang, J.; Wang, S.; Wei, P.; Yang, J.; Zhang, W.; Chen, L. "Two-dimensional thermoelectric with Rashba spin-split bands in bulk BiTeI." Physical Review B. **90**, (2014), 195210.

[8] Cappelluti, E.; Grimaldi, C.; Marsiglio, F. "Topological change of the Fermi surface in low-density Rashba gases: application to superconductivity." Physical review letters.**98**, (2007), 167002.

[9] Singh, D.J. "Electronic structure of $NaCo_2O_4$." Physical Review B. **61**, (2000), 13397.

[10] Kanishka Biswas, Jiaqing He, Ivan D. Blum, Chun-I. Wu, Timothy P. Hogan, David N. Seidman, Vinayak P. Dravid, and Mercouri G. Kanatzidis. "High-performance bulk thermoelectrics with all-scale hierarchical architectures." Nature **489**, (2012), 414-418.

[11] Glusker, Jenny Pickworth, and Kenneth N. Trueblood, "Crystal structure analysis: a primer" Oxford University Press, **14**, (2010).

[12] Chan-Chieh Lin, Dianta Ginting, R-Lydia, Min Ho Lee, Tong-Soo Rhyee, "Dataset on the electronic and thermal transport properties of quaternary compounds of $(PbTe)_{0.95-x}(PbSe)_x(PbS)_{0.05}$." J. Alloys and Compounds. **67**, (2017), 538.

[13] K. Kurosaki, A. Kosuge, H. Muta, M. Uno, and S. Yamanaka, "Ag_9TlTe_5 A high-performance thermoelectric bulk material with extremely low thermal conductivity." Applied Phys. Letts. **87**, (2005), 061919.

[14] A. Pradel, J.C Tedenac, D. Coquillat, G. Burn, Rev. Chim. Miner. **19**, (1982), 43.

[15] S.Y. Wang, G.J. Tan, W.j. Xie, G. Zheng, H. Li, J.H. Yang, X.F. Tang, "Enhanced thermoelectric properties of $Bi_2(Te_{1-x}Se_x)_3$-based compounds as n-type legs for low-temperature power generation." J. Mater. Chem. **22,** (2012), 20943.

[16] H. Wang, A.D. Lalonde, Y. Pie, G.J Synder, "The Criteria for beneficial disorder in thermoelectric solid solutions."Adv. Funct. Mater. **23**, (2013), 1586.

[17] Z. Cai, L. Guo, X. Xu, Y. Yan, K. Peng, G. Wang, X Zhou, "Effect of Sn doping in $(Bi_{0.25}Sb_{0.75})_{2-x}Sn_xTe_3$ $(0 \leq x \leq 0.1)$ on thermoelectric performance." J. Electronic Mater.**45**, (2016), 1441.

[18] K.T. Kim, T.S. Lim, G. H. Ha, "Improvement in thermoelectric properties of n-type bismuth telluride nano-powders by hydrogen reduction treatment" Rev. on Advanced Materials Science **28**, (2011),196.

[19] H. Unuma, N. Shigetsuka, M. Takahashi, "Synthesis and thermoelectric properties of the $PbSe_{1-x}Te_x$ Alloys."J. Mater. Sci. Lett. **17**, (1998), 1055.

[20] H.J. Goldsmid, J.W. Sharp, "Estimation of the thermal band gap of a semiconductor from Seebeck measurements." J. Electron. Mater. **28**, (1999), 869.

[21] K.F. Hsu, S. Loo, F. Guo, W Chen, J.S. Dyck, C. Uher, T. Hogan, E.K. Polychroniadis, M.g. Kanatzidis, "Cubic $AgPb_mSbTe_{2+m}$: Bulk thermoelectric materials with high figure of merit." Nature **489**, (2012), 414.

[22] S. Bangarigadu-Sansay, C.R. Sankar, P. Schlender, H. Klienke, J. Alloys and compounds,**594**, (2013),126.

Chapter # 06

Enhancement of Power Factor by Sn Doping IN $Tl_8Sb_{2-x}Sn_xTe_6$ Nano-Chalcogenide System

INTRODUCTION

PbTe and its solid solution having PbSe and PbS are well-known thermoelectric semiconductors [1]. However, due to the presence of Pb, PbTe-based materials are not eco-friendly because of the presence of "Pb" and as a result, the use of PbTe remains unsuitable for mass-market applications.

Various other thermoelectric materials such as SiGe [2], skutterudites [3], half-Heusler compounds [4], colusites [5], SnSe [6], SnS [7], Cu_2Se [8], exhibit high ZT (1.5-2.5) values exclusively above 500 K. Interestingly, none of the above materials show ZT above 1.0 at room temperature except the only compound Bi_2Te_3 [ZT~1.3-1.7]. Although the performance of Bi_2Te_3 has been strategically improved via various mechanisms, it is indeed coming out to be p-type [7]. In Contrast, the n-type Bi_2Te_3 remains below ZT~1.0 at room temperature [8]. Meanwhile, it has become imperative to explore new n-type thermoelectric materials that exhibit ZT above unity near room temperature as maximum energy wastage in line with geothermal power generation occurs approximately in this temperature range [9].

The current materials with high TE performance working in near-room-temperature range mainly include Bi_2Te_3-based systems, Mg_3Sb_2, MgAgSb, Mg_2 (Si, Sn), $AgSbTe_2$ and β-Ag_2Q (Q=Se, Te) [10]. Recently, there has been numerous research for a long time where β-Ag_2Q has been studied extensively for thermoelectric materials because of its intrinsic metal-like electrical conductivity and inherently glass-like thermal conductivity at room temperature [11]. Experimentally, Silver selenide specimens were prepared by a direct reaction of the source elements (6N purity) in evacuated ($\approx 10^{-4}$ Torr) quartz tubes, and X-ray diffraction analysis confirmed the formation of β-Ag_2Se [12]. However, this material shows discrepancies in ZT at the temperature range of 300-400K, which have been reported in the literature [13]. Subsequent efforts were attempted towards increasing the figure of merits of thermoelectric materials [14]. Finally, the achievement of a high ZT > 1.0 at temperature range (300-375 K) is demonstrated by improving charge carrier mobility along with tuning the carrier concentration via the addition of minute anion excess

[14]. In due course, the synthesis of solid solution $Ag_2Se_{1-x}Te_x$ has been confirmed by X-ray diffraction data and Rietveld refinement [15]. Drymiotis *et. al.* showed Ag_2Se-As_2Te phase diagram at different compositions doped the Sulphur atom in the ternary phase and examine the thermoelectric performance of the pseudo ternary phase, Ag_2Se-Ag_2Te-Ag_2S. Furthermore, we will also discuss an increment of power factor due to the Rashba type of spin splitting and as a result, we achieve a very high value of $ZT \sim 2.1$ at 400 K in $Ag_2Se_{0.5}Te_{0.25}S_{0.25}$.

In this research chapter, we will analyze the different properties of Sn (Tin) doped thallium Telluride ($Tl_8 Sn_xSb_{2-x}Te_6$) nano-structured scheme. It is synthesized by the ball milling method or mechanical milling. The XRD shows the crystal construction information and phase origin. The EDX shows the percentage components in the compound. The SEM shows the morphology of the nano-particles of the compounds. Lastly, fixed with "Sn" dopants at dissimilar absorptions and the explanations display that electrical and thermal possessions are pretentious. The two measurements such as electrical conductivity (σ) and Seebeck coefficient (S) with their physical properties have been measured with four probe resistivity setups. We used Seebeck coefficient and electrical conductivity to calculate Power factor (PF). As a result, the Seebeck coefficient is raised as the temperature of different concentrations of the compound is increased.

6. Results and Discussions:

6.1 X-Ray Diffraction

X-ray diffraction is a helpful method for examining the structural analysis of material. It can show the phase structure, crystallite size, and full width half maximum (FWHM). It also provides information on grains sizes, their position, atomic spacing, and the miller indices in detail. This entire set in the analysis of construction of the substantial [16]. Debye Scherer's formula is used to figure out the crystallite size of $Tl_8 Sb_{2-x} Pb_xTe_6$ material as given below,

$$D = k\lambda/\beta cos\theta_B \quad \text{..... (6.1)}$$

where "D" stands for the crystallite size, 'k' shows a constant with value "0.91", "λ" stands for wavelength and "θ" stands for Bragg's angle and 'β' stands for the value of full width half maximum (FWHM). The average compound crystallite size is around 63.50 nm. $Tl_8Sb_{2-x}Sn_xTe_6$ nano-particles have a concentration ratio of X=1.96, 1.97, 1.98, 1.99, 2.00.

The XRD pattern has been shifted vertically as shown. The purity of sample can be confirmed using XRD peaks pattern, which is similar to the JCPDS#84-2449 (Joint Committee on Powder Diffraction Standards) cards. The XRD peaks have hkl values of (121, 220,213,130,024). One can have observed that the material appears to be single crystalline and has a tetragonal shape.

Fig. 6.1 shows the XRD pattern for the samples at the temperature of 650 ^{0}C of the thallium antimony tin telluride's nano-particles, $Tl_8Sb_{2-x}Sn_xTe_6$ whose doping concentration is (x = 1.96, 1.97, 1.98, 1.99, 2.00) and calculated the crystal structure of the $Tl_8Sb_{2-x}Sn_xTe_6$. The highest intensity peak is at 31.800 with (213) plane orientation. The crystallographic planes are observed at (130), (121), (220), 024), (006), (240), (413), (044) and (136) orientations. The XRD diffractometer result shows that the nano-particle $Tl_8Sb_{2-x}Sn_xTe_6$ is a single phase.

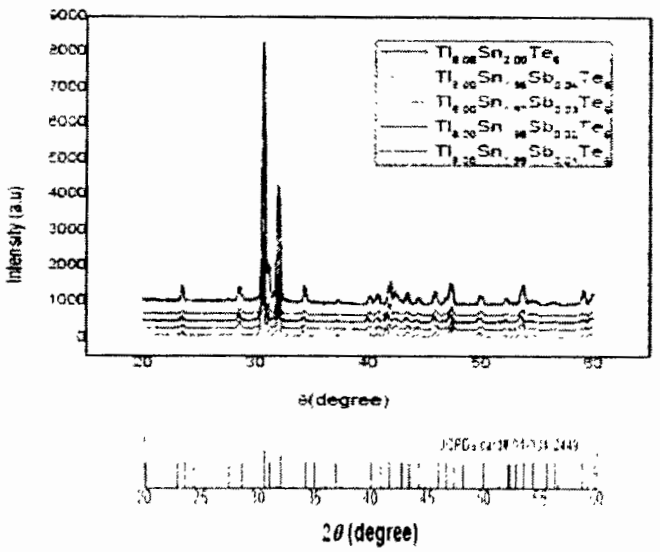

Figure 6.1 XRD ($Tl_8Sn_xSb_{2-x}Te_6$) (x=1.96, 1.97, 1.98, 1.99, 2.00).

Table 6.1 XRD ($Tl_8Sn_xSb_{2-x}Te_6$) (x=1.96, 1.97, 1.98, 1.99, 2.00).

$Tl_{8.00}Sb_{0.04}Sn_{1.96}Te_6$	25.248	a = b = 8.8931 c = 13.0050	1004.52
$Tl_{8.00}Sb_{0.03}Sn_{1.97}Te_6$	21.794	a = b = 8.8452 c = 13.0756	1023.97
$Tl_{8.00}Sb_{0.02}Sn_{1.98}Te_6$	21.171	a = b = 8.8245 c = 13.000	1013.47
$Tl_{8.00}Sb_{0.01}Sn_{1.99}Te_6$	21.119	a = b = 8.8101 c = 13.0012	1009.07
$Tl_{8.00}SbSn_2Te_6$	21.456	a = b = 8.8485 c = 13.1627	1022.73

6.2 Energy Dispersive X-ray Analysis

The EDX spectroscopy shows the ratio or quantitative percentage of the elements present in the nanoparticles. In Fig. 6.2 for nano-particles, $Tl_8Sb_{0.04}Sn_{1.96}Te_6$ has a single phase that is highly rich in thallium (69.9 % Tl, 25.8 % Te, 3 % Sn, and 1.2% Sb) for every element in the nano-particles. The atomic percent (% At) of nano-particles at numerous points have different crystals. The nominated atomic percent of the corresponding nano-particles has been related and average.

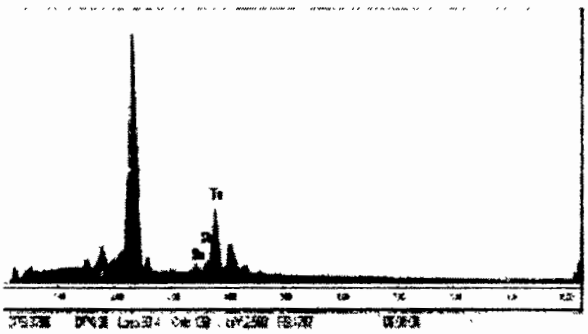

Figure 6.2: Energy Dispersive X-Ray analysis screenshot of XRD (*$Tl_8Sn_xSb_{2-x}Te_6$*).

Table 6.2: Energy Dispersive X-Ray analysis screenshot of XRD (*$Tl_8Sn_xSb_{2-x}Te_6$*).

Element	Wt %	At%
Sn	2.58	3.73
Sb	2.82	3.97
Te	25.60	34.41
Tl	69.00	57.98

6.3 Scanning Electron Microscopy

SEM is used to examine the $Tl_9Sb_1Te_6$ morphology and its properties. With the help of a scanning electron microscope, images with nanometer-level resolution can be obtained (SEM). By increasing the concentration of "Pb" doped with $Tl_8Sb_{2-x}Pb_xTe_6$ compounds, miner-sized grains are produced and provided a large scattering electron path. The material is examined under the micron and nanometer scale for better results. "Pb" concentrations increase in the grains will also increase the electron scattering which leads to an increase in thermos-power [19]. The nanostructure of $Tl_8Sb_{2-x}Sn_xTe_6$, is x=1.96, 1.97, and 1.98 at 100nm scale are shown in the image. In

Fig. 6.3 spectra show the morphology of nanoparticles of $Tl_8Sb_{2-x}Sn_xTe_6$ which are in the range of 100 nm.

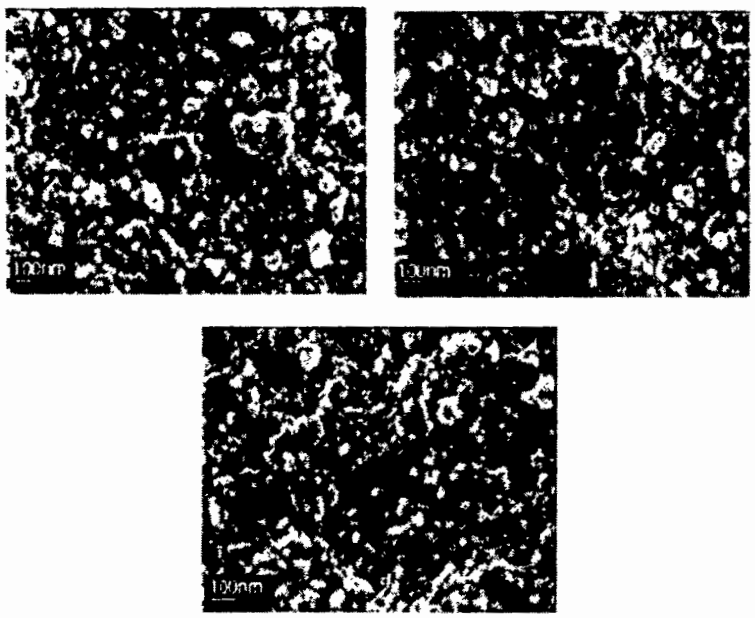

Figure 6.3 SEM (*$Tl_8Sn_xSb_{2-x}Te_6$*) (x=1.96, 1.97, 1.98, 1.99)

6.4 Electrical Conductivity Measurement

The thermal dependence of electrical conductivity for the Nano-particles $Tl_8Sn_xSb_{2-x}Te_6$ for composition (where x=1.96-1.99) has been studied in the range of 300-550 K. We have observed that electrical conductivity "**σ**" decreases as temperature increases, behave like metal doped semiconducting system as expected. The behavior of "Sn" doped in $Tl_8Sn_xSb_{2-x}Te_6$ system is true in case of intrinsic semiconductors with concentration of x=*1.96* as well as for doped semiconductors with *x* up to 1.99. Fig. 6.4 shows that the nano-particles of $Tl_8Sb_{0.04}Sn_{1.96}Te_6$ has the highest value of electrical conductivity i.e. 755.05 $\Omega^{-1}cm^{-1}$ at 300 K, which decreases as increasing the temperature, till to 454.61 $\Omega^{-1}cm^{-1}$ at 550 K. The electrical conductivity of $Tl_8Sn_xSb_{2-x}Te_6$ also decreases with increasing doping concentration of *x*. For example, the concentration of the nano-particle changed from x=1.96 to 1.99, and the electrical conductivity of the nano-particle decreased from 755.05 $\Omega^{-1}cm^{-1}$ to 566.06 $\Omega^{-1}cm^{1}$ at 300 K. Similarly, at 550 K, it decreased from 454.61 $\Omega^{-1}cm^{-1}$ to 303.75$\Omega^{-1}cm^{-1}$.

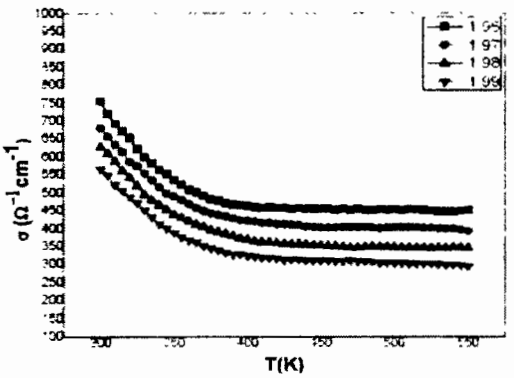

Figure 6.4: Electrical conductivity of XRD ($Tl_8Sn_xSb_{2-x}Te_6$) at 300 K, 400 K, and 550 K.

Table 6.3: Electrical conductivity of XRD ($Tl_8Sn_xSb_{2-x}Te_6$) at 300 K, 400 K, and 550 K.

Samples	Electrical conductivity ($\Omega^{-1}cm^{-1}$) At 350	Electrical conductivity ($\Omega^{-1}cm^{-1}$) At 350	Electrical conductivity ($\Omega^{-1}cm^{-1}$) At 400	Electrical conductivity ($\Omega^{-1}cm^{-1}$) At 450	Electrical conductivity ($\Omega^{-1}cm^{-1}$)	Electrical conductivity ($\Omega^{-1}cm^{-1}$) At 550
$Tl_8Sb_{0.04}Sn_{1.96}Te_6$	755.05	550.56	500.63	475.65	465.63	454.61
$Tl_8Sb_{0.03}Sn_{1.97}Te_6$	681.22	580.32	520.23	480.23	440.25	403.30
$Tl_8Sb_{0.02}Sn_{1.98}Te_6$	628.51	570.25	520.36	460.25	497.32	348.32
$Tl_8Sb_{0.01}Sn_{1.99}Te_6$	566.06	510.65	460.32	410.65	362.47	303.75

6.5 Seebeck Coefficient Measurements

The thermal dependency of the Seebeck coefficient calculated the $Tl_8Sn_xSb_{2-x}Te_6$ nano-systems have various concentrations of Sn (x=1.96, 1.97, 1.98, 1.99) has been shown in Fig. 6.5. In a previous study, heavy metals which show the deficiency in the p-type semiconductor, is determined in Tellurides system, this is also same as in $Tl_{10-x}Ln_xTe_6$ series and Tl_9BiTe_6, which is rising the number of carrier charges ($> 10^{19}$ cm^{-3}). Due to this, the trend is same as $Tl_{10-x}Ln_xTe_6$ series [17]. We have observed that the temperature increase and the Seebeck coefficient is increasing. The values of Seebeck co-efficient for $Tl_8Sb_{0.04}Sn_{1.96}Te_6$ increased from S = 297.18 μVK^{-1} at 300 K to S = 566.06 μVK^{-1} at 550 K, similarly for $Tl_8Sb_{0.03}Sn_{1.97}Te_6$ the values of "S" vary as 347.58 μVK^{-1} to 628.51 μVK^{-1} at 300-550 K. For $Tl_8Sb_{0.02}Sn_{1.98}Te_6$ the Seebeck coefficient is increased from S = 395.64 μVK^{-1} to 681.22 μVK^{-1} at 300-550 K and for $Tl_8Sb_{0.01}Sn_{1.99}Te_6$, 433.28 μVK^{-1} at 300 K to 725.76 μVK^{-1} at 550 K. It shows that the

Seebeck Coefficient gradually increased as "Sn" concentration increases in Tl_8 $Sn_xSb_{2-x}Te_6$ nano-system. The Seebeck is increase at 300 K, it is increased from 297.18 μVK^{-1} at x = 1.96 to 433.28 μVK^{-1} *at* x =1.99. Likewise, by concentration of "Sn" from x = 1.96 to 1.99, S increased from 566.06 μVK^{-1} to 725.76 μVK^{-1} at 550 K. The Seebeck coefficient depends on the temperature. The doping of the P-type materials in the nano-materials increases the Seebeck coefficient. This implies that the major carrier in the nano-materials is the holes.

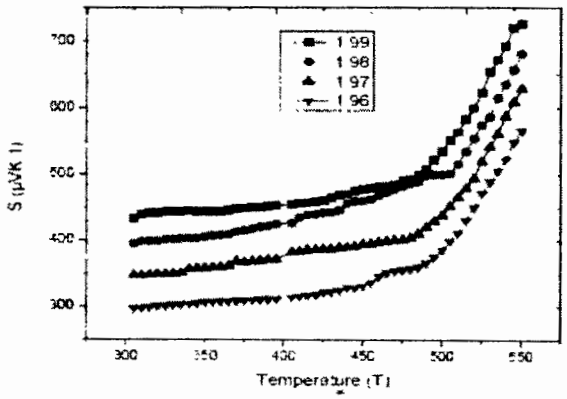

Figure 6.5: Seebeck Coefficient of $Tl_9Sb_{1-x}Sn_xTe_6$ at 300 K, 400 K, and 550 K.

Table 6.4: Seebeck Coefficient of $Tl_9Sb_{1-x}Sn_xTe_6$ at 300 K, 400 K, and 550 K.

Sample	See-beck coefficient (μK^{-1}) At 300	See-beck coefficient (μK^{-1}) At 350	See-beck coefficient (μK^{-1}) At 400	See-beck coefficient (μK^{-1}) At 450	See-beck coefficient (μK^{-1}) At 500	See-beck coefficient (μK^{-1}) At 550
$Tl_9Sb_{0.04}Sn_{1.96}Te_6$	297.18	312.23	355.28	401.94	475.56	566.06
$Tl_9Sb_{0.03}Sn_{1.97}Te_6$	347.58	380.25	421.25	498.65	561.33	628.23
$Tl_9Sb_{0.02}Sn_{1.98}Te_6$	395.64	440.52	498.32	540.23	598.23	681.29
$Tl_9Sb_{0.01}Sn_{1.99}Te_6$	433.23	490.36	565.36	640.29	692.35	725.32

6.6 Power Factor

The power factor (S^2 σ) demonstrates overall thermoelectric performance of thallium tin-antimony telluride Tl_8 $Sn_xSb_{2-x}Te_6$ nano-particles. The "Sn" doped system shows power factor values ranging from 2.21 to 8.9 $\mu W\text{-}cm^{-1}K^{-2}$ at 300 K and 550 K respectively. As shown in fig 6.6 the samples with (x =1.96, 1.97, 1.98, and 1.99) show a slight increase with less dependence on temperature and summation at same significance at 4.0 $\mu W\text{-}cm^{-1}K^{-2}$. According to previous studies, the value of power

factor at "x"=1.96 for ternary group ($Tl_{10}SnTe_6$) substitute of "Sn" is 3.6-4.9 $\mu Wcm^{-1}K^{-2}$ at temperature range from 320- 550 K respectively [18-19] whither is relatively reduced the value when compared to the one i.e. for Nano-particles. The power factor of $Tl_8Sb_{0.04}Sn_{1.96}Te_6$ system is 8.9 $\mu Wcm^{-1}K^{-2}$ at 550 K. This was the destination of this research project to amend the power factor.

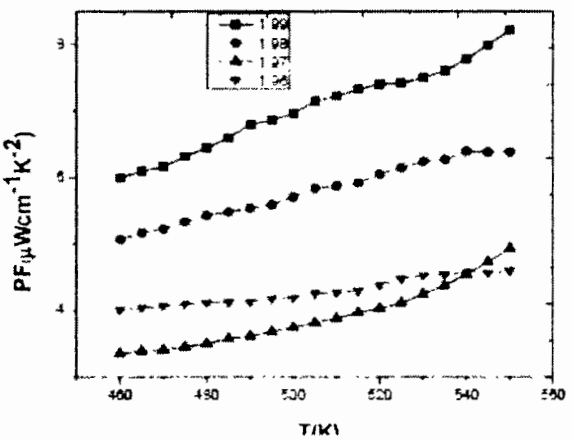

Figure 6.6: Power Factor of $Tl_9Sb_{1-x}Sn_xTe_6$ at 300 K, 400 K, and 550 K.

Table 6.5: Power Factor of $Tl_9Sb_{1-x}Sn_xTe_6$ at 300 K, 400 K, and 550 K.

Sample	Power Factor ($\mu Wcm^{-1}K^{-2}$) at 460	Power Factor ($\mu Wcm^{-1}K^{-2}$) at 480	Power Factor ($\mu Wcm^{-1}K^{-2}$) at 500	Power Factor ($\mu Wcm^{-1}K^{-2}$) at 520	Power Factor ($\mu Wcm^{-1}K^{-2}$) at	Power Factor ($\mu Wcm^{-1}K^{-2}$) at 550
$Tl_9Sb_{0.96}Sn_{0.04}Te_6$	3.25	3.5	3.75	4.25	4.52	5.01
$Tl_9Sb_{0.75}Sn_{0.25}Te_6$	4.02	4.12	4.26	5.44	5.54	5.75
$Tl_9Sb_{0.50}Sn_{0.50}Te_6$	5.35	5.54	6.28	6.25	6.56	6.75
$Tl_9Sb_{0.25}Sn_{0.75}Te_6$	6.12	6.55	7.01	7.25	7.72	8.25

6.7 Conclusion

Various concentrations of "Sn" and "Pb" doped in $Tl_8Sb_{2-x}A_xTe_6$ had a series of compounds were produced and investigated their physical properties for x has different concentrations in the compound.

These nano-materials are single phase as confirmed by x-rays diffractometry and the crystal structure of $Tl_8Sb_{2-x}A_xTe_6$ was observed with the data-based, which has the same space group 14/mcm as $Tl Te_3$. The thermoelectric properties of polycrystalline

$Tl_8Sb_{2-x}A_xTe_6$ compounds were calculated from 300-500 K. When the amount of A (Sn, Pb) doping is more the "A" doping will increase the carrier's density. In contrast, when "A" concentrations are high enough the smaller grains increase electron scattering which leads to an increase in thermos-power. The micro- and nano-optimization of materials appear to hold the promise of even more advancements. Because of the increasing hole concentration in this "A" doped chalcogenide nano-system, the Seebeck coefficient of the doped tellurium telluride decreases with increasing "A" concentration. This decrease in Seebeck coefficient is due to the increased electron scattering. However, the smaller grains present in high "A" concentrations will increase electron scattering, as a result, the thermos-power will also increase. It appears that further improvements are achievable by optimal and physical on both the micro and nano scales as revealed in various research works on PbTe [20].

6.8 Reference

[1] G. J. Snyder, E. S. Toberer, "Complex thermoelectric materials." Nat. Mater. **7**, (2008), 105.

[2] S. Bag, O. Gunawan, T. Gokmen, Y. Zhu, D. B. Mitzi, "Hydrazine-processed Ge substituted CZTSe Solar Cells." Chem. Mater. **24**, (2012), 4588.

[3] H. Dittrich, A. Bieniok, U. Brendel, M. Grodzicki, D. Topa, "Proceedings of sympodium o on thin film chalcogenide photovoltaic materials, EMRS 2006 Conference." Thin Solid Films, **515**, (2007), 5745.

[4] P. Jackson, D. Hariskos, E. Lotter, S. Paetel, R. Wuerz, R. Menner, W. Wischmann,M. Powalla, "New World Record Efficiency for Cu(In, Ga)Se_2 Thin-film solar cells beyond 20%." Prog. In Photovoltaics **19**, (2011), 894.

[5] S. C. Riha, B. A. Parkinson, A. L. Prieto, "Solution-based synthesis and characterization of Cu_2ZnSnS_4 Nanocrystals."J. Am. Chem. Soc. 131, 12054 (2009).

[6] T. K. Todorov, K. B. Reuter, D. B. Mitzi, "High-efficiency solar cell with the earth-abundant liquid processed absorber." Adv. Mater. **22**, (2010).

[7] J. Androulakis, S. C. Peter, H. Li, C. D. Malliakas, J. A. Peters, Z. Liu, B. W. Wessels, J.-H. Song, H. Jin, A. J. Freeman, M. G. Kanatzidis, "Dimensional reduction: a design tool for new radiation detection materials." Adv. Mater. **23**, (2011), 4163.

[8] S. Johnsen, Z. Liu, J. A. Peters, J.-H. Song, S. C. Peter, C. D. Malliakas, N. K. Cho, H. Jin, A. J. Freeman, B. W. Wessels, M. G. Kanatzidis, "Thallium chalcogenide based wide band gap semiconductor $TlGaSe_2$ for radiation detectors." Chem. Mater. **23**, (2011), 3120.

[9] P. L. Wang, Z. F. Liu, P. Chen, J. A. Peters, G. J. Tan, J. Im, W. W. Lin, A. J. Freeman, B. W. Wessels, M. G. Kanatzidis, "Two-dimensional mineral Pb_2BiS_3 $AuTe_2$: High-mobility charge carriers in single-atom-thick layers." Adv. Funct. Mater. **25**, (2013), 4874.

[10] H. Chen, J. Jiang, L. Zhang, H. Wan, T. Qi, D. Xia, "highly conductive Nico 2 s 4 urchin-like nanostructures for high-rate pseudo capacitors." Nanoscale **5**, (2013), 8879.

[11] W. Du, Z. Zhu, Y. Wang, J. Liu, W. Yang, X. Qian, H. Pang, "One-Step Synthesis of $CoNi_2S_4$ Nanoparticles for Supercapacitor Electrodes."RSC Adv. **4**, (2014), 6998.

[12] S. Peng, L. Li, C. Li, H. Tan, R. Cai, H. Yu, S. Mhaisalkar, M. Srinivasan, S. Ramakrishna, Q. Yan, "*In situ* growth of $NiCo_2S_4$ nanosheets on graphene for high-performance supercapacitors." Chem. Comm. **49**, (2013), 10178.

[13] G. Wang, L. Zhang, J. Zhang, "A review of electrode materials for electrochemical supercapacitors" Chem. Soc. Rev., **41**, (2012), 797-828.

[14] Kanishka Biswas, Jiaqing He, Ivan D. Blum, Chun-I. Wu, Timothy P. Hogan, David N. Seidman, Vinayak P. Dravid, and Mercouri G. Kanatzidis. "High-performance bulk thermoelectrics with all-scale hierarchical architectures." Nature **489**, (2012), 414-418.

[15] A. J. Minnich, M. S. Dresselhaus, Z. F. Ren, and G. Chen, "Bulk nanostructured thermoelectric materials: current research and future prospects, Energy Environ. Sci., **2**, (2009), 466–479.

[16] X. Shi, J. Yang, L. Wu, J. R. Salvador, C. Zhang, W. L. Villaire, D. Haddad, J. Yang, Y. Zhu, and Q. Li, "Band Structure Engineering and Thermoelectric Properties of Charge- Compensated Filled Skutterudites", Sci. Rep.,**5**, (2015), 14641.

[17] Y. Liu, H. Xie, C. Fu, G. J. Snyder, X. Zhao, and T. Zhu, "Demonstration of a phonon-glass electron-crystal strategy in (Hf, Zr)NiSn half-Heusler thermoelectric materials by alloying," J. Mater. Chem. A, **3**, (2015), 22716–22722.

[18] C. Bourg`es, Y. Bouyrie, A. R. Supka, R. Al Rahal Al Orabi, P. Lemoine, O. I. Lebedev, M. Ohta, K. Suekuni, V. Nassif, V. Hardy, R. Daou, Y. Miyazaki, M.

Fornari and E. Guilmeau," High-performance thermoelectric bulk colusite by process controlled structural disordering," J. Am. Chem. Soc.,**140**, (2018), 2186–2195.

[19] Z.-G. Chen, X. Shi, L. D. Zhao, and J. Zou, High-performance SnSe thermoelectric materials: progress and future challenge, Prog. Mater. Sci., **97**, (2018), 283–346.

[20] W. He, D. Wang, H. Wu, Y. Xiao, Y. Zhang, D. He, Y. Feng, Y. J. Hao, J. F. Dong, R. Chetty, L. Hao, D. Chen, J. Qin, Q. Yang, X. Li, J.-M. Song, Y. Zhu, W. Xu, C. Niu, X. Li, G. Wang, C. Liu, M. Ohta, S. J. Pennycook, J. He, J.-F. Li and L.-D. Zhao, "High thermoelectric performance in low-cost $SnS_{0.91}Se_{0.09}$ crystals," Science, **365**, (2019), 1418–1424.

Chapter # 07

Enhancement of the Figure of Merit by the Quaternary Compound $Tl_8Sb_xPb_{1-x}Te_6$ by Doping of Pb & Sb Co-Doped Nanostructured

INTRODUCTION

As a future generation, the actual global energy deficiency and the environmental pollution issues that lie leading pose a serious threat. The deterioration of the ozone layer as a result of global warming and pollution has had far-reaching consequences. In order to meet the enormous demand for energy in both the domestic and industrial sectors, it is necessary to conduct extensive research in the energy sector using a variety of nano-scale materials and technologies [1]. A significant amount of effort has also been put forth in order to achieve control over the energy crisis and temperature of global is increasing due to losses of different energy sources in several industrial sectors. There are two problems with energy firstly energy sources problems and secondly, management of wasted energy are two of the most pressing issues facing the world in the twenty-first century [2]. Bio-fuel, wind, solar, etc. are just some of the sources of energy. People and businesses use heat energy to do things and make things. At that point, any wasted heat energy has been used up and there has been no change in energy [3].

The first thermoelectric effect was discovered more than a century ago by Thomas Johanne Seebeck [4, 5] and Jean Charles Athanase Peltier [6, 7]. This effect is based on the principle of producing electrical energy through the use of a temperature gradient. Bi_2Te_3 has demonstrated notable performance as an efficient thermoelectric (TE) material. It is worth noting that high-temperature thermodynamic ally stable materials are preferred for thermoelectric applications [5, 8]. As a result of their thermal stability and good thermoelectric properties, such materials are promising for new next-generation engineering science that utilizes waste heat and converts it into useful electrical energy [9]. Approximately, 40% of energy is used and consumed in industrial processes with the rest discarded as waste heat. Possibly, Thermal power conversion (thermoelectric generators) can capture a portion of this waste heat and turn it into recyclable electricity [11]. The electronic and thermoelectric characterization of pure and doped bulk Tl_5Te_3 crystal structures (designated as $Tl_{10-x-y}Pb_xSb_yTe_6$ with x= [0:2] and y= [0:2]) were studying by using the DFT method [12] with Plane-Wave (PW) basis enforced in the Quantum Espresso

(QE) code [13]. For the electronic exchange-correlation energy functional, we used the Perdew, Burke, and Ernzerh (PBE) generalize gradient approximation (GGA) [14, 15]. The ultra-soft pseudo potential of A. Dal Corso inside the PBE signifier was used [16], in which only the outer-most electrons were considered.

Various measurement devices owned by the three participating evaluation laboratories were used to determine the transport properties of the pressed pellets. To ensure the reliability and reproducibility of the data obtained, a standardization and round-robin testing program has been initiated to test self-built measurement facilities. The theoretical portion of this article is devoted to predicting the best Te, Sb, and combined Te-Pb doping levels based on the power factor. The electronic figure of merit ZT is used to estimate the resulting improvement in the total figure of merit. In the constant relaxation time approximation, electronic transport properties are calculated using semi-classical Boltzmann transport theory. According to this theory, the electronic transport properties of a material are derived solely from its electronic structure which is calculated using ab-initio electronic structure calculations using the density functional theory DFT Approach.

In this chapter, we will measure different properties of the "Pb" (Lead) doped thallium Telluride ($Tl_8Sb_xPb_{1-y}Te_6$) nanostructured scheme. It is synthesized by the ball milling method or mechanical milling. The XRD shows the crystal construction information and phase origin. The EDX shows the percentage components in the sample. The SEM shows the morphology of the nanoparticles of the sample. Lastly, fixed with "Sb" dopants at dissimilar absorptions and the explanations display that electrical and thermal possessions are pretentious. Electrical conductivity and Seebeck coefficient were calculated from the four probes resistivity investigational methods which had two standard probe computation schemes, respectively. Power factor (PF) was calculated from Seebeck coefficient and electrical conductivity. As a result, the Seebeck coefficient is enhanced as the temperature of the nano-system increases, which is explained in the section below.

7. Results and Discussions:

7.1 X-ray Diffraction

XRD shows the crystalline scheme through which demonstrated the lattice constant, miller indices, arrangement of grain, inter planner, and interatomic size [17].

Pure phase of $Tl_8Sb_xPb_{1-x}Te_6$ of the nano-particles by showing the XRD spectra. The XRD spectra of $Tl_8Sb_xPb_{1-x}Te_6$ (x=1.96, 1.97, 1.98, and 1.99) the nano-particles were analyzed with *Reference card: 01-084-2449.* For XRD $Tl_8Sb_xPb_{1-x}Te_6$ (x=1.96, 1.97, 1.98, and 1.99). nano-particles, the diffraction peak at 23.3^0 (121),29^0 (120),31^0 (212),32^0 (130),34^0 (024),40^0 (224),42^0 (006),46^0 (240),47^0 (413),50^0 (044) and 53^0(136) planes recognized the tetragonal crystal structure.

These peaks show XRD information and are compared with the previous study with JCPDS (Joint Committee on Powder Diffraction Standards) cards with *Reference card: 01-084-2449* as shown in x-ray diffraction diagrams. At room temperature, we used the main source such as the Intel powder diffractometer equipped with a positional-sensitive detector and CuKα. At last, we had expanded forty-eight (48) peaks in XRD diagram, originating in model. X-ray powder diffraction showed that our compound is the single-phase with a different concentration. Ourselves introduce XRD pattern got for $Tl_8Sb_xPb_{1-x}Te_6$ and associate it with that of $Tl_8Sb_xPb_{1-x}Te_6$ as shown below in Fig. 7.1.

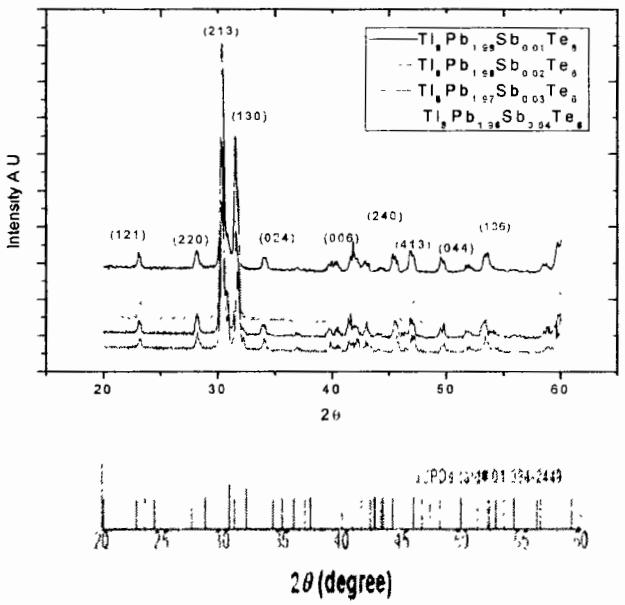

Figure 7.1: XRD $Tl_8Sb_xPb_{1-x}Te_6$ (x=1.96, 1.97, 1.98, and 1.99).

7.1.1 Crystal Structure

The structural characterizations of Tl_5Te_3 in Fig. 7.2 before discussing substitutional doping in the crystal structure. There are 20 Tl-atoms and 12 Te-atoms in a primitive unit cell depicted in Fig. 7.2(a)–(b), each occupying one of four

different crystal positions. There are two Tl atoms in the crystallographic positions 4c and 16l, and two Te atoms in the crystallographic positions 4a and 8h (Wyckoff positions 4a and 8h). Because of the space group I4/mcm, the crystal structure of Tl_5Te_3 equilibrium crystals is tetragonal, similar to that of Br_3Cr_3. Fig. 7.2(b) shows the Tl_5Te_3 crystal structure's PBE-GGA optimized volume of $(1080.9A^0)^3$. Bond length "b" Tl-Te is calculated to be 2.44 Angstroms which is larger than the experimentally measured bond length of 2.51 Angstroms (a=8.92 and 12.62) [17]. In most cases, this is because GGA overestimates the optimized volume or lattice parameters [18]. In spite of this, previous research on Tl_5Te_3 [19, 20] found these results to be consistent. To investigate the electronic and thermoelectric characterizations of the Tl_5Te_3 with sub-situational doping and co-doping "Pb" and "Sb" atoms at the Tl-sites were introduced.

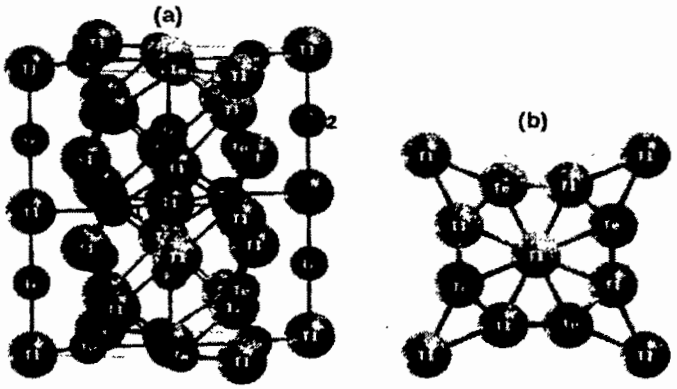

Figure 7.2: (a) Schematic side view, (b) top view of unit cell of the Tl_5Te_3 crystal structure used for DFT Calculation. The green ball represents Tl and the red ball represents the Te atoms.

7.2 Energy Dispersive X-ray

This method is incapable of determining the precise ratio of elements in the last compounds individually, any encouraging elemental investigation is performed to supplement the diffraction determination method. When it comes to determining composition in solid-state materials by the EDX. It is a useful method that performs similarly to SEM. Mostly elemental investigation is a method for elaborating on a specimen's constitution by providing an exact value. It may also provide quantitative, percentages or ratios of the elements included within those samples.

EDX spectrums of "Pb" nano-particles doped in the $Tl_8Sb_xPb_{1-x}Te_6$ (x=1.96, 1.97, 1.98, and 1.99). From the above spectrum in EDX Model, it has given

information that the compound is consist of wt% of 14.38% Pb, 25.53% Te, 27.78% Sb, and 57.69% Tl content in $Tl_8Sb_xPb_{1-x}Te_6$.

In Fig. 7.3, the EDX shows the weight percentages (wt%) which helped the precise stoichio metric amount of every element which is present within compound. Ourselves get to establish that "Pb" doped with dissimilar absorptions variations the degree of top shown through EDX Fig.7.3. Consequently, Atomic percentages (At%) of elements are 14.51% *Pb*, 27.22% Te, 0.12% Sb, and 58.13% Tl in $Tl_8Sb_xPb_{1-x}Te_6$. It is noted that the "Sb" concentration with the Tl: Te ratio appears to be slightly similar in the spectra (by a few percent) as shown in Fig 7.3. Another set of spectra can be visible in this region, which demonstrates the collection of the data. Each sample is subjected to a minimum area using an electron beam with an energy between 20 and 25 eV during the analysis process and on average, data is collected in 30-second intervals.

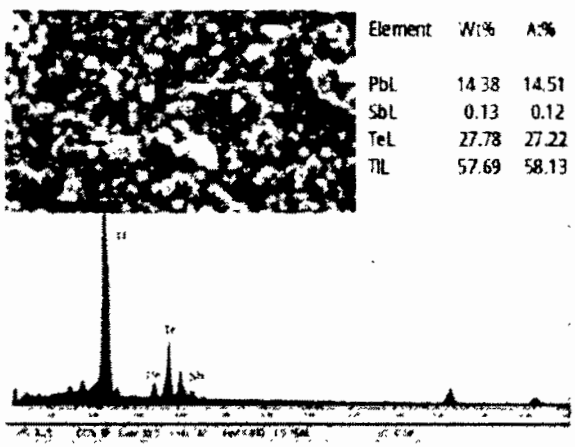

Figure 7.3: Energy Dispersive X-Ray analysis screenshot of $Tl_8Sb_xPb_{1-x}Te_6$ (x=1.96, 1.97, 1.98, and 1.99).

7.3 Scanning Electron Microscope

An electron microscope (SEM) and an x-ray spectrometer (EDX) have been used to look at the nano-structured $Tl_9Sb_1Te_6$ morphology and composition. By increasing the concentration of "Pb" doped with $Tl_8Sb_{2-x}Pb_xTe_6$ compounds, miner-sized grains are produced and provided a large scattering electron path. "Pb" concentrations increase in the grains will also increase the electron scattering which leads to an increase in thermos-power [21]. The nanostructure of Tl_8Sb_{2-x} Sn_xTe_6, at 100nm scale is shown in the image.

EDX was used to analyze the composition qualitatively and quantitatively. Fig 7.2 illustrates the EDX of $Tl_8Pb_{1.97}Sb_{0.03}Te_6$ nanoparticle. Pb, Sb, Te, and Tl are identified in this method and their weight percentages (14.38 percent for Pb, 0.13 percent for Sb, 27.78 percent for Te, and 57.69 percent for Tl) are calculated. This percentage indicates the concentration of all substances in the method. While "Pb" (14.51%), Sb (0.12%), Te (27.22%), Tl (58.13%) are all at percentage rang. It demonstrated no additional peak investigated in the chemical composition. The thallium (Tl) concentration is highest at the peak than others.

7.4 Electronic Band Structure Calculation

We will examine the most critical case in terms of interpreting the PDOS. P DOS-based conductance analysis doesn't appear to have well-established roots because MO is arbitrarily identified. At Fermi energy, the most significant PDOS was precisely the one associated with the MO exhibiting the highest degree of localization on the molecule bond MLWF (i.e., the LUMO). Without the latter, we would have missed this critical MO from the zero-bias conductance analysis.

The electronic structure of Tl_5Te_3 is computed by the electronic band structure and Partial density of states as shown in Fig 7.4(a)–(d) at optimized lattice parameters. As shown in Fig. 7.4 (a), the behavior of Tl_5Te_3 is non-magnetic and metallic in accordance with the early abstraction and research results [22].

Further examination of the structure of electronic reveals an idea of narrow band gap which is from higher than Fermi energy, accordant with the consequence obtained by Nor-dell et al. In the Tl_5Te_3 structure shown in Fig 7.4 (a)–(d)), Pb substitutional doping led to a 0.25eV rise in the Fermi level. This confirmed that Tl_5Te_3 has a concentration-dependent semiconducting nature. The crystal structure of "Bi or Sb" doped Tl_5Te_3 was previously predicted to be semiconducting [23]. Its tunable semiconducting nature makes it suitable for doping with other heavy elements to improve its electronic properties [24].

The orbital characteristics of the PDOS as shown in Fig. 7.4 (b)–(d). It displayed that in axenic Tl_5Te_3 nano-particle, valance band maximum (VBM) primarily contributed by Tl2 atoms-orbitals and Te1 atom p-orbitals, which partially interbred with d-orbital of Tl atoms Fig. 7.4 (d). Additionally, as a result of strong hybridization, the conduction band minimum is predominately populated by Tl orbital

states with a minor contribution from Te orbital states (P orbitals). The PDOS calculation was performed on "Pb" doped at Tl-site in Tl_5Te_3 crystal composition, as illustrated in Fig. 7.4 (b)–(d). It reveals that "Pb" doping generates pureness conditions in the conduction band and cut down the repulsion in bonding and anti-bonding states. As a result, the pseudo-band gap in the conduction band decreases by 0.12 eV. This means that p-orbital states of the dopant "Pb" atoms in Fig. 7.4 (b)–(d) contribute most of CBM.

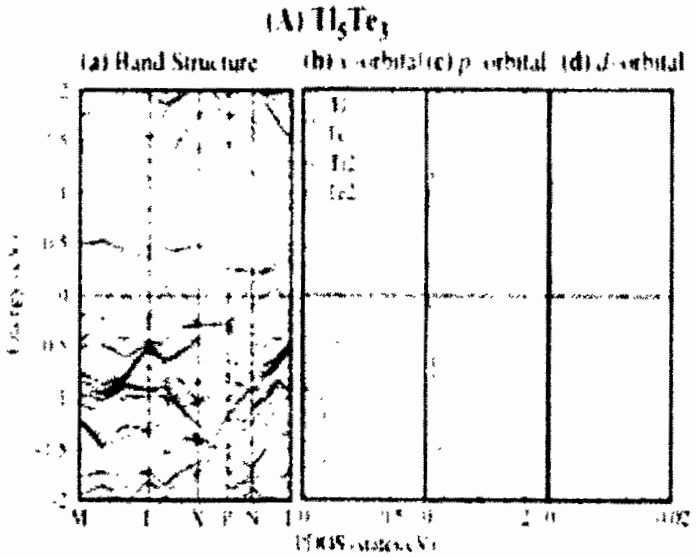

Figure 7.4: (a) Band structure (b) PDOS s-Orbital (c) PDOS p-Orbital (d) PDOS d-Orbital of respective compound.

Thermoelectric properties were studied using both experimental and DFT measurements on axenic, "Pb" or "Sb" treated and co-doped nano-structured Tl_5Te_3. The efficient and effective method was doping to attain the desired electrical and thermal properties [25]. The TDOS shown in black line in Fig 7.4(a), demonstrates the performance of conducting and non-magnetic Tl_5Te_3 crystal structure. The TDOS (see Fig. 7.4 (a)) confirmed these findings, showing that the band-gap in "Pb' doped CBM is moved down than in the pure Tl_5Te_3 crystal structure. According to Fig. 7.5, TDOS has two valance bands and one conduction band at Fermi level. In the Tl_5Te_3 crystal structure, the pointed TDOS peaks near Fermi behave like p-type doping. But it also controls n-type doping in Tl_5Te_3 crystal composition, a pointed peak above the EF in conduction bands. With "Pb and Sb" doping or co-doping at Tl-site, the TDOS of pure Tl_5Te_3 nano-particles decreases. The pure Tl_5Te_3 nano-particle has a highest TDOS at EF, With "Pb and Sb" doping or co-doping at Tl-site, the TDOS of pure

Tl_5Te_3 nano-particles decreases of all the compounds studied. The lowering of TDOS at EF may improve the Seebeck coefficient. The Seebeck coefficient and electronic conductivity are both proportional to the total density of states and they serve as important tests for the materials' electronic and thermoelectric properties.

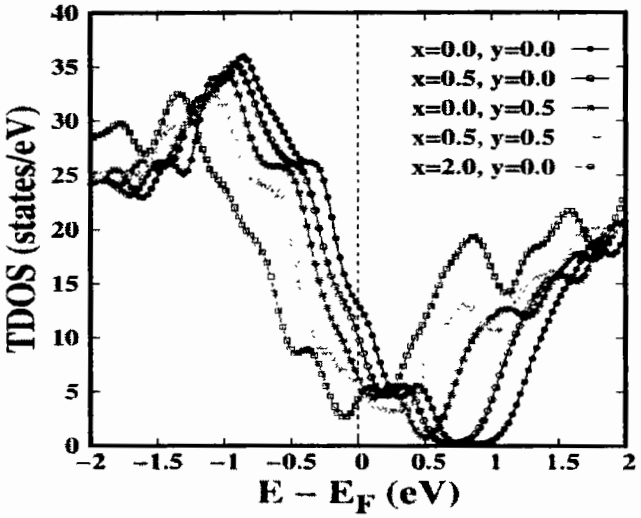

Figure 7.5: The black, blue, pink, and green lines indicate the total density of states (TDOS) crystal structure of equilibrium lattice constant. The Fermi Level is denoted by dashed line.

7.5 Thermoelectric Properties

7.5.1 Experimental Data

A decrease in electrical conductivity as temperature rises can be seen in Fig. 7.6(a) for all the compositions studied in this study. $Tl_8Pb_{1.96}Sb_{0.04}Te_6$ nano-particle has produced a slightly flat line. The valance p states of "Pb" or "Sb" atoms have one or two electrons than the valance p states of "Tl" atoms. Dopants increased electrical conductivity by supplying extra electrons to charge carriers.

Fig. 7.6(b) represents the Seebeck coefficient as it changes with temperature or concentration, with a rising or downing way for all total mixtures. The concentration of "Pb" and "Sb" doping is critical in order to improve electrical conductivity. The electrical conductivity decreases as the dopant concentration increases as a result of electron scattering with defective states. Power factor of n-type nano-materials is greatly improved by increasing electrical conductivity and Seebeck coefficient. At temperature 550 K, the perfect PF (738.84 $\mu WK^{-2}m^{-1}$) for $Tl_8Pb_{1.96}Sb_{0.04}Te_6$ nano-structure was calculated. All the nano-particles in Fig. 7.5(c)

show a linear increase in PF with increasing temperature, in a manner similar to the Seebeck coefficient.

The final strategy was to reduce thermal conductivity ($\kappa=\kappa_e+\kappa_{lattice}$) of $Tl_8Pb_xSb_{2-x}Te_6$ nano-structure to increase ZT. Each of these considerable samples exhibits the performance of metal. The thermal and electrical conductivity with degenerate semiconductors are linked by the Weidman Franz Law, which is expressed as $\kappa_e=L\sigma T$, where 'L' stands for Lorentz number, which has a value of 2.45×10^{-8} $W\Omega K^{-2}$ and T stands for temperature. As shown in fig. 7.6(c), the amount of κ rises when temperature rises and decreases when the "Sb" dopants concentration increases. At temperature of 300 K, the lowest value of The $Tl_8Sb_{0.04}Pb_{1.96}Te_6$ nano-particles is 1.13 $Wm^{-1}K^{-2}$ at 300 K, which increases to 1.35 Wm^{-1} K^{-2} at 550 K.

At a temperature of 500 K (300 K), $Tl_8Pb_{1.96}Sb_{0.04}Te_6$ nano-particle has maximum and minimum PF quantity is 861.39 $\mu WK^{-2}m^{-1}$ (205.50 $\mu WK^{-2}m^{-1}$). According to A. F. Ioffe [26], maximum thermoelectric efficiency and low thermal conductivity are projected in narrow electronic band gap semiconductors which are produced through the 5p and 6p electrons, predicted in the middle nineteenth century. Because the heavy elements in their crystal structures make up their composition.

The first thermoelectric material with a value of 0.8 of thermoelectric figure of merit at 300 K was composed using Pb (lead), Sb (antimony), doped Bi (Bismuth), and Te (telluride). Fig. 7.6(e) shows the indirect relationship between the Pb and ZT but directly proportional ZT and Sb, where increase in Pb dopant concentration, decreases the ZT but increases the ZT with enhanced Sb co-dopant distribution. Variation of concentration of Sb co dopant with the nano-particles of $Tl_8Pb_{1.96}Sb_{0.04}Te_6$ compound has a ZT value of 0.05 at 300 K and a ZT value of 0.35 at 550 K.

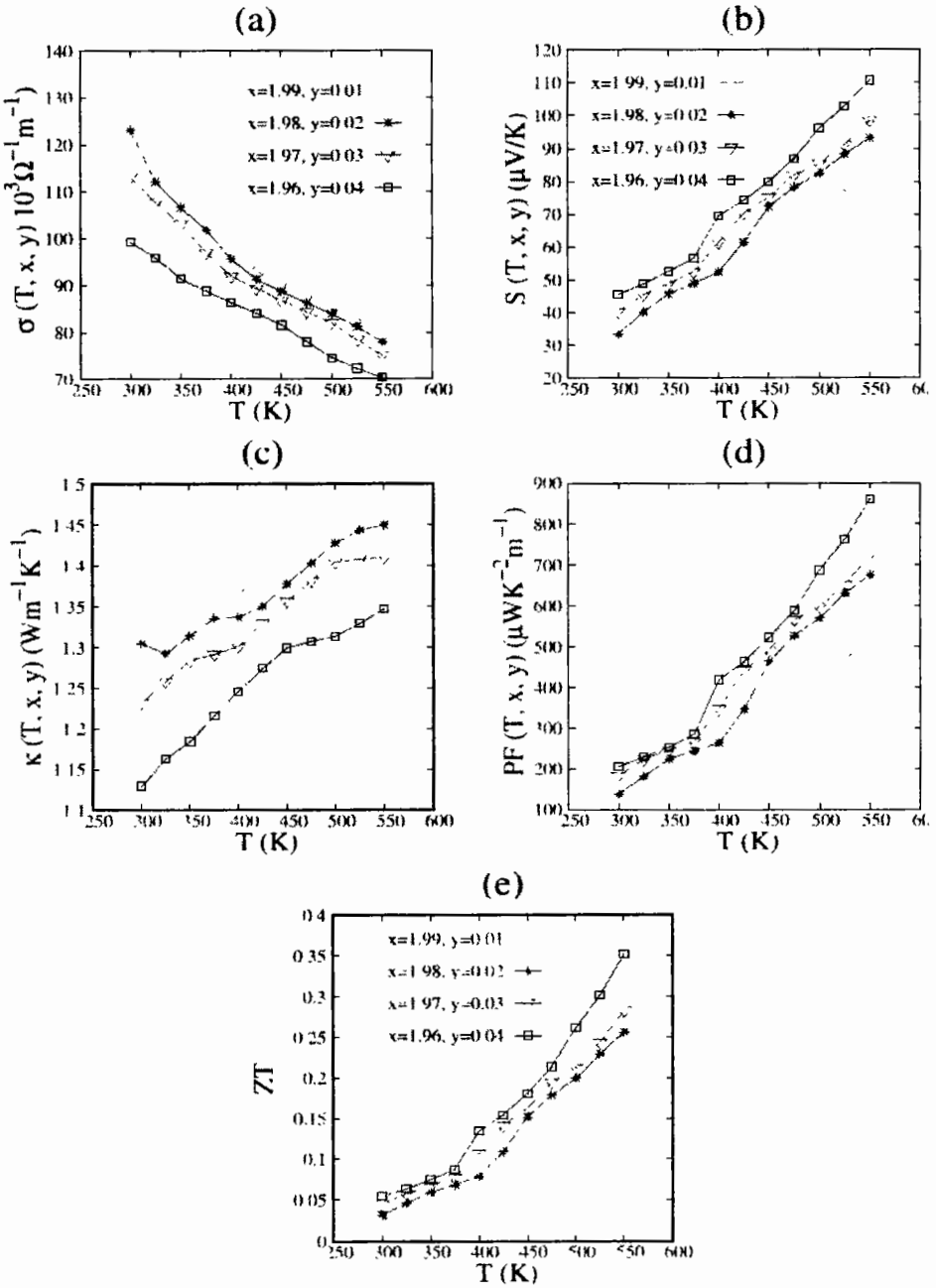

Figure 7.6: Experimentally measured (a) Electrical conductivity (b)Seebeck Coefficient (c) Thermal conductivity (d) Power factor (e)Figure of Merit.

7.5.2 Theoretical Measurement

As shown in Fig. 7.7(a), the electrical conductivity (σ) increases initially with Pb-doping before decreasing with addition of "Pb" atoms or "Sb" as a co-dopant replacement. The σ exhibits a similar pattern throughout the entire temperature range. Fig. 7.7(a) depicts that the σ of the un-doped Tl_5Te_6 and doped $Tl_{9.5}Pb_{0.5}Te_6$

compounds, having electrical conductivity are extremely high at the normal temperature with the values of $160\times10^3\,\Omega^{-1}\,m^{-1}$ and $158\times10^3\,\Omega^{-1}\,m^{-1}$, respectively.

The electrical conductivity is inversely proportional to the temperature where temperature increases of temperature, electrical conductivity decreases. It is indicated the performance of metal in accordance with the calculated electronic band structure in this study. In case of un-doped crystal, the electrical conductivity (σ) shows the highest values as compared to the small value of Seebeck except at the high concentration of "Pb". The experimental results show, the electrical conductivity decreased as enlarge the Sb co-dopants distribution, and also increase the Seebeck. In the sample $Tl_{9.5}Sb_{0.5}Te_6$ shows that the electrical conductivity is slightly decreased while the Seebeck coefficient increased significantly, resulting in a high PF in the 0-800 K temperature reach. It is clear that crystal structure depends on the electron and holes are doping in the Tl_5Te_6 crystal structure as shown by the variations in electrical conductivity reason by "Pb" and "Sb" dopants. Similarly, donor-doped and acceptor-doped $SrTiO_3$ support this conclusion [19]. Furthermore, the valance band would be filled with a hole (electron) created by substitutional dopants as evidenced by the positive sign. However, in our study, every dopant act as a hole in the Tl_5Te_6 crystal structure, and their thermoelectric properties are equal to Fermi energy. As a result, holes are the dominant transfer in all of the substances examined using DFT.

However, increases the temperature of the given sample the Seebeck coefficient shows a positive value, with the exception of the axenic and intemperately "Pb" doped Tl_5Te_6 crystal structure, which remained constant throughout shown in Fig. 7.7(b). The Seebeck coefficient is measured as positive in all cases, which allows for an excitable examination of substantial-close nearness to the Fermi energy to be performed. Seebeck coefficient required large values for the operation of efficient thermoelectric devices. Seebeck coefficient tuning is shown in Fig. 7.7(b) as a result of the "Pb" and "Sb" atoms.

At 800 K, $Tl_{9.5}Sb_{0.5}Te_6$ and $Tl_{9.0}Pb_{0.5}Sb_{0.5}Te_6$ compounds had increased Seebeck 60 μV/K. Further study reveals that the Seebeck coefficient decreases beyond these concentration values, as demonstrated by the the$Tl_{8.0}Pb_{2.0}Te_6$ compound. As a result, at mediate distribution values, such as "Pb" and "Sb" co-doping (x=0.5 and y=0.5), we can expect a good thermoelectric response of the Tl_5Te_6 crystal structure. As shown in Fig. 7.7(b), substitutional doping concentration has a similar effect on theoretical and experimental Seebeck values. The variation in the value of

theoretically calculated and experimentally measured values is found due to these compounds with the improvement at their lowest state in DFT at 0 K but thermoelectric properties are not obtained from the ground state experimentally [24]. As a result, The DFT method has both advantages and disadvantages [25, 26].

Heat is carried by lattice vibrations and electrons in materials. In semiconductors, heat is mostly conducted by lattice vibration, while in metals, it is mostly conducted by free electrons. The lattice thermal conductivity is safe to ignore in conductors it is less than 2% of whole thermal conductivity. It is desirable to use good thermoelectric materials with low thermal conductivity are preferred in thermoelectric generators to carry the changing of temperature in compounds as in Fig. 7.7(d)). The interaction of different electrical properties determines thermoelectric PF. If a TE generator has a high Seebeck coefficient, high electrical conductivity, and low thermal conductivity, its figure of merit (ZT) will be large. Both Fig. 7.6(e) and 7.7(e) observed that the figure of merit increases due to measuring the data of experimental and theoretical, respectively. The doping of Pb and co-doping of the "Sb" crystal structure have the highest value of ZT by experimental is 0.35 and theoretical ZT is 0.12 values of all the studied crystal structures, as can be seen from the graphs. Fig. 7.7 (b) shows that the Seebeck coefficient increases due to co-doping such as Sb in the sample. It gives same result as the experimental data. so that the increases of Seebeck coefficient by the Sb so that value of the figure of Merit is also high. So experimental and theoretical show that the Figure of Merit increases as the dopant of "Sb" increases. The value of ZT is high so it is of good use for thermoelectric materials. For the high value of ZT, we will be increasing the value of phonon for reducing the thermal conductivity by the doping of "Sb" or "Pb" [26] there is large number of phonon scattering is produced which causes the production of the mean free path. Our experimental and theoretical data shows doping of "Sb" causes the increases in ZT, which is interesting. A previous study found that bulk silicon had a ZT of 0.003, but that nano-structured "Si" with an increased ZT of two orders of magnitude [26, 27] is in line with this new finding.

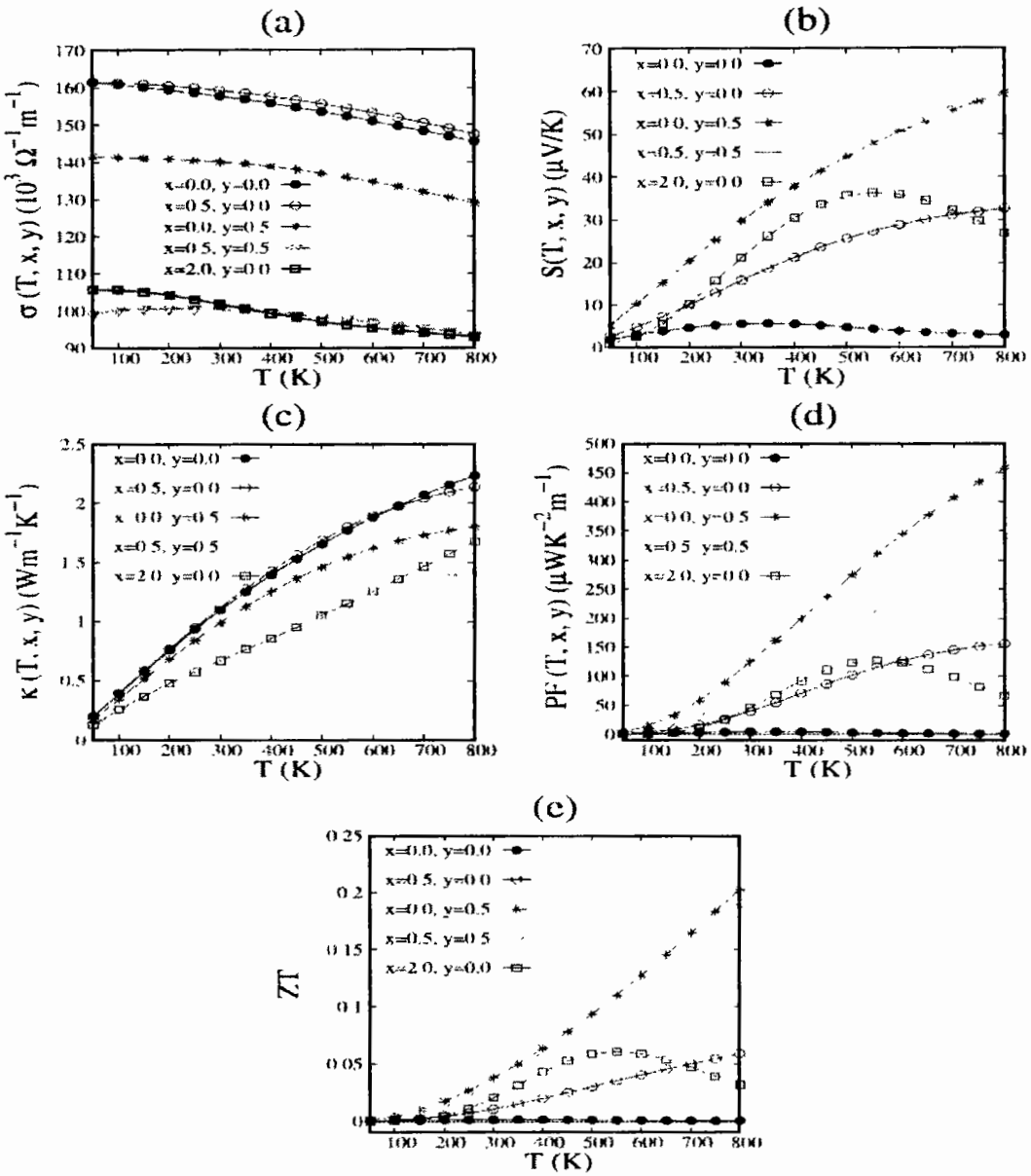

Figure 7.7: Theoretically calculated (a) Electrical conductivity (b)Seebeck Coefficient (c) Thermal conductivity (d) Power factor (e)Figure of Merit

7.6 Conclusion

The quaternary nano-particles $Tl_8Pb_xSb_{2-x}Te_6$ was fabricated by the co-precipitation method and had different concentration of "Pb" and "Sb" dopants (x=1.96, 1.97, 1.98, 1.99). . The experimental formula was used to determine the $Tl_8Sb_{2-x}Sn_xTe_6$ crystal structure with 14/mcm space group same as Tl_5Te_3 and x-rays diffractometer method proved its single phase. XRD analysis of the Tl_5Te_3 nano-particles revealed that they were in an iso-structural phase. The DFT calculations

predict the same thing as well. In this study, the results show that concentration of "Pb" increases, when high electrical conductivity than the Seebeck coefficient is low over the temperature range. As a result, the "Pb" concentration has a negative result on the power factor, indicating that an increase in electrical conductivity does not compensate for a drop-off in the Seebeck coefficient across all compositions. Nano-particles of $Tl_8Pb_{1.96}Sb_{0.04}Te_6$ exhibits the lowest electrical conductivity (602.9 $W\Omega^{-1}m^{-1}$). $Tl_8Pb_xSb_{2-x}Te_6$ nano-structured semiconductor is a degenerative semiconductor, as confirmed by electrical conductivity determination. The electrical conductivity of the entire composition decreases as the temperature range expands. At different temperatures, it shows the positive characteristic of the Seebeck coefficient that holes conduction is the most important contributor. The decrease in the Seebeck coefficient is caused by increase in the concentration of "Pb" because of increase in electron scattering behavior. Nonetheless, a power factor of 738.85 $\mu Wm^{-1}K^{-2}$ was achieved by improving electrical conductivity and Seebeck coefficient carefully contained "Sb" concentration doping. When the concentration of dopants "Pb" and "Sb" was increased in the Tl_5Te_3, the DFT calculations proved that there was a sudden decrease in the electronic thermal conductivity was reduced dramatically, which was accompanied by a rise in the Seebeck coefficient and electrical conductivity. Tl_5Te_3 energy dispersion calculations based on ab-initio electronic structure results overestimate electrical conductivity while underestimating thermopower at room temperature. This is due to the fact that the temperature dependence of density of states cannot be taken into account when computing the chemical potential in ab-initio electronic structure results. For a given "n" and temperature "T" this raises the chemical potential values. This has the effect of increasing electrical conductivity while simultaneously decreasing thermopower. Consequently, the ab-initio density functional theory (DFT) cannot correctly describe the transport properties of Tl_5Te_3 at zero temperature, even though it is known that m_d and E_g are highly dependent on temperature. The thermoelectric efficiency of Tl_5Te_3 nano-particles has increased the concentration of dopants "Pb or Sb". The compounds containing the dopants like "Pb" is doping and "Sb" is co-doping to ZT=0.35 experimentally and ZT=0.18 as theoretically. As a result, Tl_5Te_3 nano-particles with improved thermoelectric properties have been revealed in a contained mode and this has the possible to be used in the design and makes sufficient thermoelectric products for use in harvesting of

energy with a new dimension of nano-structured compounds as demonstrated in this study.

7.7 References

[1] MinnichA J, Dresselhaus MS, Ren Z F, and Chen G, "Bulk nanostructured thermoelectric materials: current research and future prospects."2009 Cambridge: Energy Environ. Sci. **2,** (2009) 466–479.

[2] Alama H. and Ramakrishnab S., "A review on the enhancement of figure of merit from bulk to nano-thermoelectric materials." Nano Energy **2,** (2013), 190–212.

[3] Polozinea A., Sirotinskayab S. and Schaeffera L, "History of development of thermoelectric materials for electric power generation and criteria of their quality." Materials Research, Brasil **17**, (2014), 1260.

[4] Rahman G. and Rahman A.U., "Thermoelectric properties of n and p-type cubic and tetragonal $XTiO_3$ (X= Ba, Pb): A density functional theory study." Physica B **526,** (2017), 122.

[5] Seebeck T J. "Magnetic polarization of metals and ores by temperature differences." (1822) 289–340.

[6] Peltier JCA. "Annales De Chimie Et. De Physique (in French)." **56,** (1834) 371–86

[7] Thomson W. Proc. of the Royal Society of Edinburgh **3**, (1851), 91–98.

[8] Ali A, Rahman A.U. and Rahman G., "Thermoelectric properties of $Kcaf_3$." Physica B., **565,** (2019), 18.

[9] Rowe D.M. (ed.), "Thermoelectric, handbook, macro to nano." (Boca Raton. CRC Press, Taylor & Francis), (2006).

[10] Chiang P.W. and Gluck J.V., "Slip Modes of Hexagonal-Close-Packed Metals." J. Appl. Phys. **38,** (1967), 4671.

[11] Pradel A, Tadenac J.C., Brun Gand, Maurin M, "The Iron-Iron Carbide Phase Diagram: A Practical Guide to Some Descriptive Solid State Chemistry." J. Solid State Chem. **45,** (1982), 99.

[12] Kurosaki K, Kosuga A, Goto K, Muta Hand Yamanaka S, "Compositional Difference of Thermoelectric Properties in Ag_9TlTe_5." Mater. Trans. **47,** (2006), 1938.

[13] Hohenberg P and KohnW, "Inhomogeneous Electron Gas." Phys. Rev. B **136**, (1964), 71.

[14] Giannozzi P. et al. "QUANTUM ESPRESSO: A modular and open-source software project for quantum simulations of materials." J. Phys. Condense. Matter **21**, (2009), 395502.

[15] Blochl P. E., "The Interface between silicon and a high-k oxide." Phys. Rev. B **50**, (1994), 17953.

[16] Allen P. B., Picket W.E., and Krakauer H., "Anisotropic normal-state transport properties predicted and analyzed for high-tc oxide superconductors." Phys. Rev. B **37,** (1988), 7482.

[17] Corso A.D., "."Comput. Mater. Sci. **95**, (2014), 337.

[18] Monkhorst H.J. and Pack J.D., "Special points for brillouin-zone integrations." Phys. Rev. B **13**, (1976), 5192.

[19] Madsen G.K.H. and Singh D.J., "Boltz Trap. A Code for Calculating Band-Structure Dependent Quantities." Boltz Trap. Comput. Phys. Commun. **175,** (2006), 67.

[20] Sun J. and Singh D.J., "Thermoelectric properties of *n*-type $SrTiO_3$" APL Mater **4,** (2016), 104803.

[21] Bhan S. and Schubert K., "Kristallstruktur von Tl_5Te_3 und Tl_2Te_3." J. Less-Common Met. **20,** (1970), 229.

[22] Persson K.et al. "Commentary: The Materials Project: A materials genome approach to accelerating materials innovation." APL Mater. **1,** (2013), 011002.

[23] Xu B, Liang J., Li X., Sun J. F. and Yi L. "Effects of geometrical symmetry on the vortex in mesoscopic superconductors," Eur. Phys. J. B **79,** (2011), **275**.

[24] Onida G., Reining L., and Rubio, "Electronic Excitations: Density-Functional Versus Many-Body Green's-Function Approaches." A. Rev. Mod. Phys. **74,** (2002), 601.

[25] Rashkeev S.N. and Lambrecht W.R. L. "Second-Harmonic Generation of I-III-VI2 Chalcopyrite Semiconductors: Effects of Chemical Substitutions." Phys. Rev. B **63**, (2001), 165212.

[26] Yang N., Gang Z. and Li B, "Violation of Fourier's law and anomalous heat diffusion in silicon nanowires "Nano. Lett. **8**, (2007), 76.

[27] Bux S. K. et al.," Nanostructured Bulk Silicon as an Effective Thermoelectric Material." Adv. Funct. Mater. **19**, (2009), 2445.

Chapter #08

Effects of doping in $Tl_{10-x}ATe_6$ (A= Pb & Sb)

INTRODUCTION

The needs of the time is to develop large thermoelectric efficient systems with low-cost materials that are compatible with modern technology. Alternative energy ways particularly those based on thermoelectric materials are becoming increasingly important as fossil fuels are depleted. These compounds can change heat energy from a change in temperature converted into electrical energy or electrical energy is exploit a temperature gradient called Seebeck effect. (Effect of Peltier) it has piqued interest as a potential application in the automotive industry, where the waste thermal energy can be regenerated into electrical energy. The dimensionless figure of merit ZT [1] determines the performance of a material in thermoelectric applications. In compound electrical properties should be large e.g. Seebeck coefficient, and electrical conductivity, while the thermal conductivity is small possible and capable of keeping in the temperature variance between the hot and cold junctions. It can't be done to improve each of the three quantities on its own, because they are all interconnected with each other. The enhancement of Seebeck coefficient and electrical conductivity of compounds that are good for thermo-electrics, while decreases the thermal conductivity in arrangement to keep heat at junction and decreases the amount of heat lost. Tl_2SnTe_5 [2], Ag_9TlTe_5 [3], Tl-filled skutterudite [4, 5], and $TlSbTe_2$ are examples of Thallium Telluride or Thallium Antimony with complex crystalline structures. $Tl_9(Bi/Sb)\ Te_6$ [6, 7], $Tl_9(Sn/Pb)\ Te_6$ [8, 9], and $Tl_4(Sn/Pb)\ Te_3$ [10, 11] are some of the more useful ternary groups of Tl_5Te_3 that have enhanced thermoelectric characterization.

In this work, we have investigated Thallium Antimony Telluride, $Tl_{10-x}Sb_xTe_6$, which is a type of nano-material that have similar properties to Tl_4ZrTe_4 [12], Tl_2ZrTe_3 [13] with good thermoelectric properties to Tl_9SnTe_6 and Tl_9BiTe_6 systems. The same phenomenon occurs in the I4/mcm group as well as in the iso-structural to $Tl_5Te_3 \equiv Tl_{10}Te_6$ with different ratios in the Sb and Tl [14]. The nano-material of $Tl_{10-x}Sb_xTe_{6o}$ power factor is 4.4-8.9 $\mu Wcm^{-1}K^{-2}$which is compatible to that of Tl_4PbTe_3 - Tl_9PbTe_6 which is 5.2 to 6.2 $\mu Wcm^{-1}K^{-2}$ at temperature 685 K [9, 15]. This research helps to better understand how the effects of temperature and the thermoelectric effects on the "Sn" doped in Tellurium Telluride $Tl_{10-x}Sb_xTe_6$ over an entire range of

temperature, the power generator can also measure their thermo-electrical properties. The goal and significance of this research are to see the concentrations of charge carriers affect the Seebeck coefficient, electrical conductivity, and power factor of different dopants on thallium telluride nano-system. We studied thallium nano-particles because of their low thermal conductivity and moderate electrical performance in the investigation of superior nano-thermoelectric compounds [16].

Using varied dopant concentrations, we investigated the influence of charge carrier induction/reduction on thermal and transport properties. The concentration of charge carriers influences the electron-hole ratio, which rises the electron scattering and thus affects electrical conductivity and thermos power. Since we have studied ($Tl_{10-x}ATe_6$) compound properties which have low thermal and high electrical conductivity as well as the possibility of using it as an enhanced showing nano-thermoelectric properties.

In this chapter, we will measure different properties of the "Sn & Pb" (Tin, Lead) doped Thallium Telluride ($Tl_{10-x}ATe_6$) nano-structured scheme. It is synthesized by the ball milling method or mechanical milling. The XRD shows the crystal construction information and phase origin. The EDX shows the percentage components in the compound. The SEM shows the morphology of the nano-particles of the compounds. Lastly, fixed with "Sn, Pb" dopants at dissimilar absorptions and the explanations display that electrical and thermal possessions are pretentious. The four probe methods can be calculated as the Seebeck coefficient and electrical conductivity which had two standard probe computation schemes, respectively. The electrical conductivity and Seebeck coefficient help us to measure the Power factor (PF). As a result, the Seebeck coefficient is raised as the temperature of different concentrations of the compound is increased which is shown in table and figure.

8. Results and Discussions:

8.1 X-Ray diffraction

It is greatest multipurpose besides precise deflection method owing to structural study of crystalline scheme. By adopting mentioned method, lattice constant, miller indices, grain bigness arrangement, inter-atomic extent besides inter planner array can be strong-minded [17]. We inspected the cleanliness of the composite by examining peaks in XRD information that were far ahead and co-ordinate with situation in literature along with JCPDS cards, as shown in diagrams. An Intel powder

diffractometer equipment is used with a position-sensitive detector and a CuKα source that operates it. Afterwards carefully examining Forty-eight (48) peaks in XRD diagram, we are directed to accomplish that no contamination was originating in model. XRD sequence authorizes the single-phase arrangement of mixtures. Ourselves introduce XRD pattern got for $Tl_{10-x}ATe_6$ and associate it with that of $Tl_{10-x}ATe_6$ as shown below in Fig. 8.1.

The structural analysis of the materials is done using X-ray diffraction. It aids in the analysis of crystal structure and particle size. There are several $Tl_{10-x}ATe_6$ with doped "Pb" and "Sn". The A stands for a doped element that is different from the rest. "Pb" and "Sn" are represented by A, respectively. It has a variety of concentrations. Fig. 8.1 shows the X-ray diffraction of $Tl_{10-x}ATe_6$ with various "Pb" and "Sn" doping concentrations. Their peaks differ due to the different concentrations, as shown in Fig. 8.1.

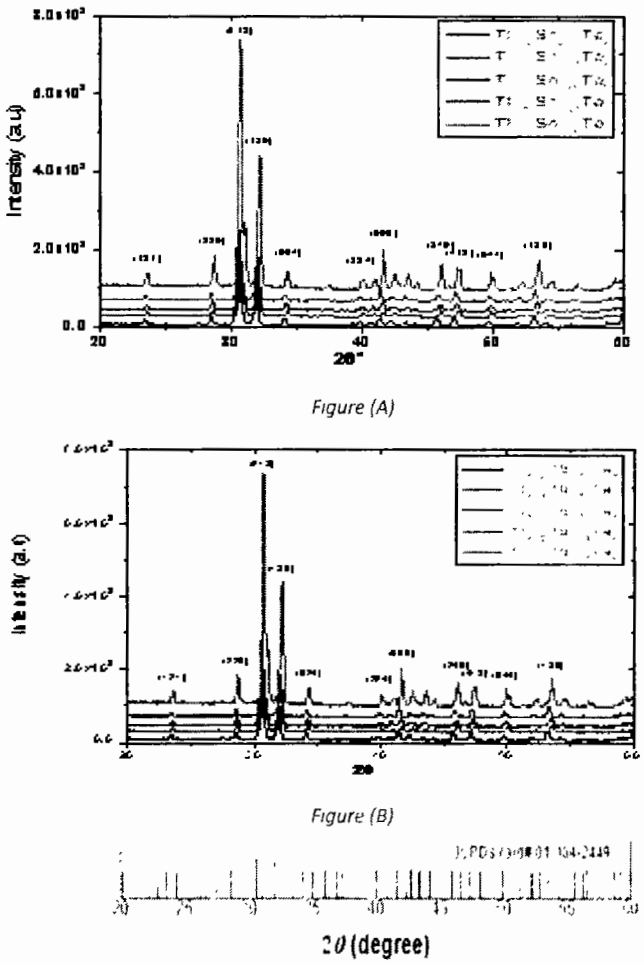

Figure 8.1: XRD $Tl_{10-x}ATe_6$ (x=1.00, 1.25, 1.50, 1.75, 2.00).

Table 8.1: XRD $Tl_{10-x}ATe_6$ (x=1.00, 1.25, 1.50, 1.75, 2.00).

	32.247	a = b = 8.8931 c = 13.0052	1004.521
	31.795	a = b = 8.84510 c = 13.07515	1023.925
	31.180	a = b = 8.82510 c = 13.00010	1013.429
	31.128	a = b = 8.81010 c = 13.0010	1009.093
	31.055	a = b = 8.84814 c = 13.16215	1022.722

Table (A)

	31.972	a = b = 8.8931 c = 13.0052	1004.521
	31.795	a = b = 8.84510 c = 13.07515	1023.925
	31.580	a = b = 8.82510 c = 13.00010	1013.425
	31.328	a = b = 8.81010 c = 13.0010	1009.091
	31.155	a = b = 8.84814 c = 13.16215	1022.712

Table (B)

8.2 Energy Dispersive X-ray Analysis

This technique has been accustomed to going into a qualitative and computable examination of numerous models. Elemental details are examined through mentioned method for every composite existing in the model. Together with percentage of uniqueness in model. EDX spectrum of Sn or Pb nano-particles doped in $Tl_{10-x}ATe_6$ with Sn or Pb=1.00, 1.25, 1.50, 1.75, 2.00. From the spectrum, it has been specified that the sample is comprised of wt% of 1.10% Sn, 25.53% Te, 25.53% Sb, and 69.46% Tl content in $Tl_{10-x}ATe_6$

The weight percentages (wt. %) display the precise stoichiometric amount of every element which is present within composite. Ourselves get to establish that "Sn or Pb" doped with dissimilar absorptions variations the degree of top shown through EDX figure. Consequently, Atomic percentages (At %) of elements are of 1.59% Sn, 34.41% Te, 5.53% Sb and 58.47% Tl in $Tl_{10-x}ATe_6$

For every component, Atomic percentages (At%) at numerous degrees of dissimilar crystals of a specific model have been averaged as well as associated with the quantified atomic percentage of comparable composite.

Spectral investigation was completed by exploring by the computer used the software (EDAX) along with origin software besides typical ZAF fitting act owing to little peak fitting. Electron rays were used in the range of 20 to 25eV, and average data was compiled for thirty (30) seconds, with each model retaining at least four spot scans and one full area. EDX is done with a high-vacuum EDAX Pegasus 120 detector and a thin polymer window to make sure disclosure in addition to carbon presence. EDAX Genesis was used to compare minor ZAF fitting ranges to a standardized peak fitting. The ray of electron utilized in the process is between 2.580 K eV and averages data assembled during 30-second intermissions with a maximum of one filled area examine.

The EDX of the $Tl_{10-x}ATe_6$ is shown in Fig. 8.2 with different concentrations of Pb and Sn doping in it. The composition of the compounds is shown by the EDX. It shows that it contains "Pb" and "Sn".

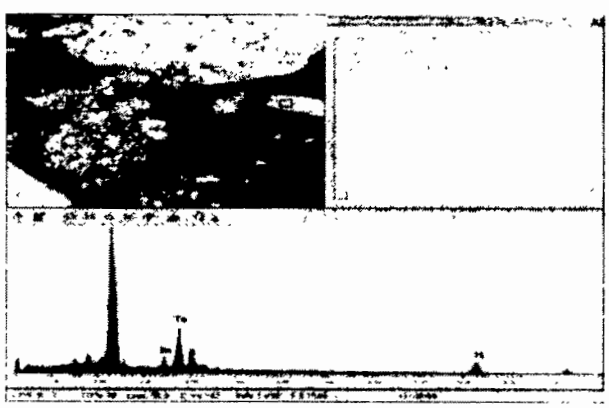

Figure (A)

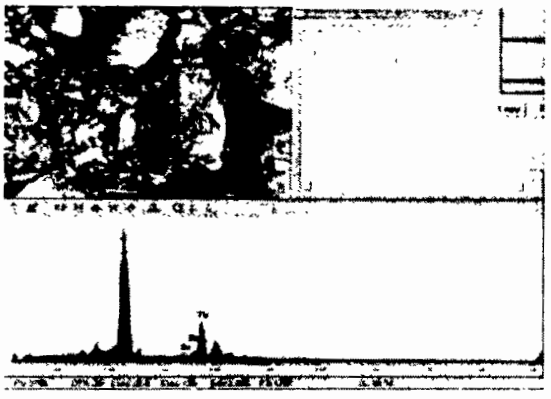

Figure (B)

Figure 8.2: Energy Dispersive X-Ray analysis screenshot of $Tl_{10-x}ATe_6$ (x= 1.00, 1.25, 1.50, 1.75, 2.00).

8.3 Electrical Conductivity Measurement

The electrical conductivity of these ternary models was examined and found to decrease with increasing temperature representing a positive temperature coefficient which is indicative of a degenerate characteristic. This is caused by charge carriers' phonon scattering and grain boundary effects [18].

We've seen an increase in hole concentration when the concentration of "Sn or Pb" is raised. The sample temperature contingent is reduced by grain boundary scattering, but only slightly.

There appears to be no discernible trend in the relationship between "Sn or Pb" absorptions and electrical conductivity for a chalcogenide scheme such as $Tl_{10-x}ATe_6$. In some cases, it might be said that the presence of oxide contamination. The electrical conductivity of the chalcogenide system decreases because it changes the phase of the boundary grain by the sinter at very low pressure [19]. One thing it says is that two causes could play a function in the electric abilities of a chalcogenide system. One is "Tin" doping, and the other is the phase of the grain boundary.

We investigated the electrical conductivity of $Tl_{10-x}ATe_6$ at various temperatures (x= 1.00, 1.25, 1.50, 1.75, 2.00). We know that as temperature rises, electrical conductivity decreases across the temperature spectrum, as shown in Fig. 8.3. The above-mentioned results support the existence of metallic conduct. It is possible to argue that similarity is an indication of relatively high carrier absorption.

As evidenced by detection, a significant decrease in electrical conductivity has been observed as a result of an increase in doping absorption. The following are examples of dissimilar experiences for dissimilar absorptions at 295 K, the maximum

value is 403.42 $(\Omega\text{-cm})^{-1}$ and minimum value is 184.16 $(\Omega\text{-cm})^{-1}$ at 550 K of $Tl_{10-x}ATe_6$ compound. Additional mixtures with absorptions (x= 1.00, 1.25, 1.50, 1.75, 2.00). $Tl_{10-x}ATe_6$ allotment keeps extremely near low values of 195.43 besides 205.79 $(\Omega\text{-cm})^{-1}$ correspondingly.

Ourselves get detected a negligible alteration from 230.21 to 230.13 $(\Omega\text{-cm})^{-1}$ in electrical conductivity for $Tl_{10-x}ATe_6$ compound at room temperatures of 445 K and 450 K on account of hot pressed pellets besides ingot. Above mentioned outcomes are shown beneath in table 8.2.

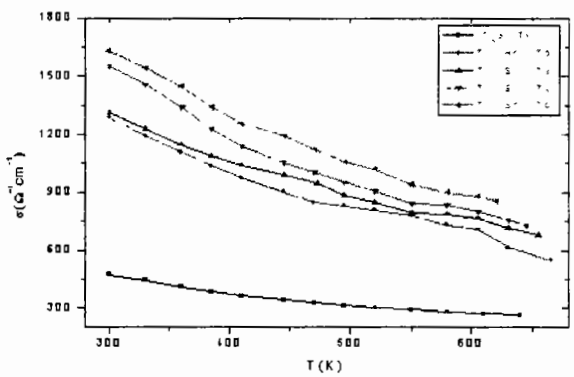

Figure (A)

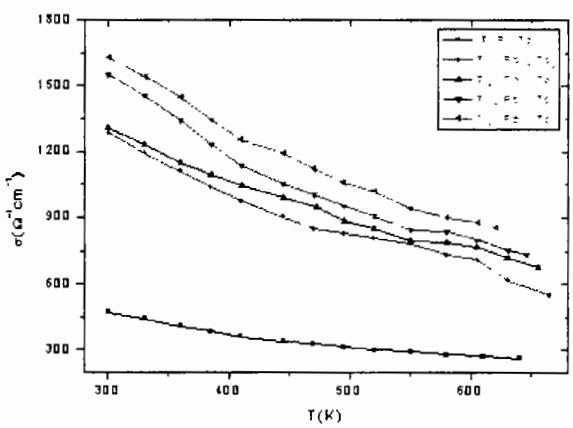

Figure (B)

Figure 8.3: Electrical conductivity of $Tl_{10-x}ATe_6$ at 300K, 400 K, and 550K.

Table 8.2: Electrical conductivity of $Tl_9Sb_{1-x}Sn_xTe_6$ at 300 K, 400 K, and 500 K.

Sample	Electrical conductivity (Ω^{-1} cm^{-1}) at 300 K	Electrical Conductivity (Ω^{-1} cm^{-1}) at 550 K
$Tl_9Pb_1Te_6$	1645	890
$Tl_{8.75}Pb_{1.25}Te_6$	1540	750
$Tl_{8.50}Pb_{1.50}Te_6$	1335	610
$Tl_{8.25}Pb_{1.75}Te_6$	1301	585
$Tl_8Pb_2Te_6$	460	288

Table (A)

Sample	Electrical conductivity (Ω^{-1} cm^{-1}) at 300 K	Electrical Conductivity (Ω^{-1} cm^{-1}) at 550 K
$Tl_9Sn_1Te_6$	1650	900
$Tl_{8.75}Sn_{1.25}Te_6$	1545	760
$Tl_{8.50}Sn_{1.50}Te_6$	1350	620
$Tl_{8.25}Sn_{1.75}Te_6$	1320	590
$Tl_8Sn_2Te_6$	450	295

Table (B)

8.4 Seebeck Coefficient Measurement

To study, the impact of decreased charge carriers on thermal and transport properties "Sn" content of $Tl_9Sb_{1-x}Sn_xTe_6$ (x=1.00, 1.25, 1.50, 1.75, 2.00) was increased by replacing "Sb" atoms in the formula with "Sn" atoms. Fig. 8.4 illustrates the Seebeck coefficient at temperature difference for $Tl_9Sb_{1-x}Sn_xTe_6$ (x=1.00, 1.25, 1.50, 1.75, 2.00) compounds. For all compounds, the positive Seebeck coefficient rises quickly as the temperature rises from 295 K to 550 K especially, since there are high charge carrier concentrations in p-type semiconductors. It is determined that all of the different temperatures cause the Seebeck coefficient, indicating that the thermoelectric transport in these compounds is governed by the conduction of the p-type (hole) carrier. The doping "Sn" is assumed to develop carrier density as the amount increases from "0.01 to 0.05". However, the small grains of "Sn" doping are thought to improve electron diffusion, resulting in an increase in the Seebeck coefficient as well as effective mass [20, 21]. It demonstrates that only a sufficient

amount of "Sn" doping is capable of increasing the Seebeck coefficient in this particular system. In other words, doping reduces the Seebeck coefficient significantly, when the "Sn" concentration is increased above its optimal value. Improved charge mobility and carrier density can be achieved simultaneously with improved Seebeck coefficient by (i) using a fast fabrication process such as melting rotation to reduce grain size in an abundantly better way, (ii) by improving doping elements and their consistent extent. [21]

Positive "S" is observed in all $Tl_9Sb_{1-x}Sn_xTe_6$ models. It rises with concentration (x=1.00,1.25,1.50,1.75,2.00) smoothly with increasing the temperature. The trend shows that there is a high charge carrier which is due to the p-type semiconductor as shown in Fig.8.4. With "x" = 2.00 Seebeck coefficient arc has a distinct maximum of S=+105.32 μVK^{-1} at 300 K and S=+193.63 μVK^{-1} at 550 K at a concentration of "x"=1.96. The Smallest Seebeck coefficient has a value of S=+75.54 μVK^{-1} at 295 K which rises to S=+145.65 μVK^{-1} at 550 K. It is recognized that the Seebeck coefficient increase with increase in the concentration of "Sn" within host illustration. For example, for "x"=2.00 concentration, the value of Seebeck coefficient is S=+88.12 μVK^{-1} at 300 K which rises to S=+173.88 μVK^{-1} at 500 K respectively.

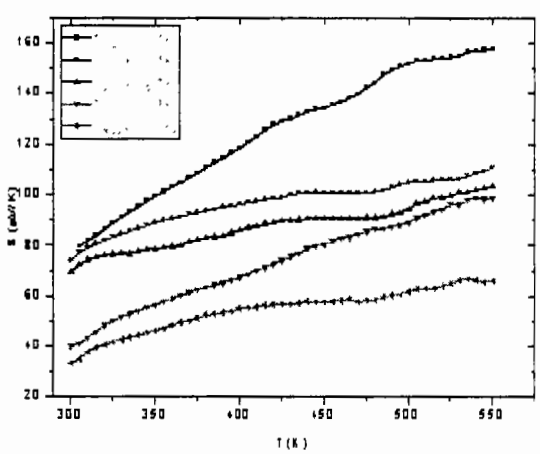

Figure (A)

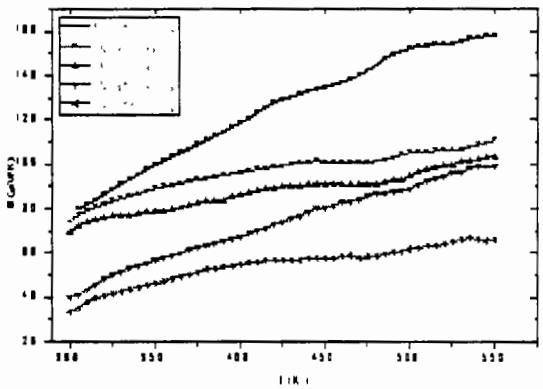

Figure (B)

Figure 8.4: Seebeck Coefficient of $Tl_{10-x}ATe_6$ at 300K, 400 K, and 550K.

Table 8.3: Seebeck Coefficient of $Tl_{10-x}ATe_6$ at 300K, 400 K, and 550K

Sample	See-beck coefficient(μV/K) at 300 K	See-beck coefficient(μV/K) at 550 K
$Tl_8Pb_1Te_6$	32	56
$Tl_{8.75}Pb_{1.25}Te_6$	40	90
$Tl_{8.50}Pb_{1.50}Te_6$	68	100
$Tl_{8.25}Pb_{1.75}Te_6$	73	110
$Tl_6Pb_2Te_6$	80	160

Table (A)

Sample	See-beck coefficient(μV/K) at 300 K	See-beck coefficient(μV/K) at 550
$Tl_8Sn_1Te_6$	30	80
$Tl_{8.75}Sn_{1.25}Te_6$	38	90
$Tl_{8.50}Sn_{1.50}Te_6$	66	98
$Tl_{8.25}Sn_{1.75}Te_6$	72	110
$Tl_6Sn_2Te_6$	78	158

Table (B)

8.5 Power Factor

In the above-mentioned compounds, Electrical conductivity decoupling, rather than Seebeck coefficient, is strongly suggested for enhancing the power factor (PF= $S^2\sigma$). We similarly distinguish that have found an inverted association on account of these binary terms in these schemes. Seebeck coefficient holds a deep influence on power factor. Accordingly, ourselves essential to improve "S" owing to power factor improvement. We experienced that power factor is measured by knowing of electrical conductivity and Seebeck coefficient and information take strategic in Fig. 8.5. Power factor is increasing with rising of temperature. Ourselves get experimented with extremely complicated conduct of power factor about doping absorption of "Sn".

The power factor inquiries display the aforementioned rising as well as because of developing conduct in Seebeck coefficient along with temperature. Moreover, there is a direct relationship among power factor toward square of Seebeck coefficient, as clarified circumstantially inside introduction section, along with electrical conductivity is as well declines purposely beside temperature. For "Sn"=*1.96,* smallest power factor has the value of 2.00 $\mu Wm^{-1}K^{-2}$ at 295 K while at 550 K, power factor rises to7.7 $\mu Wm^{-1}K^{-2}$ for "Sn"=2.00 in case of "Sn & Pb" =1.98, power factor starts at 2.63 $\mu Wm^{-1}K^{-2}$, and increases with increasing temperature, whereas in case of "Sn & Pb"=1.96 starting point of power factor is 2.00 $\mu Wm^{-1}K^{-2}$ and it increases with increasing temperature. Already stated power factor (PF) get detected because of tremendously less electrical conductivity of $Tl_9Sb_{0.99}Sn_{0.01}Te_6$ which act main character in power factor study.

Thermoelectric properties are optimised due to the Tin (Sn) dopant absorption in model, which is depending on high Seebeck coefficient (S) and high electrical conductivity while over low thermal conductivity. Because complicated conduct of power factor (PF) verse temperature is by no means explained real constancy of thermoelectric possessions enclosed by entire scheme, that is why this system is arbitrary locations of solid-state phenology while displaying faultiness on top of crystalline materials. Extra agent is electronic conduct because of unlike temperature choice of semiconductor materials, include gaps of disparate energy band.

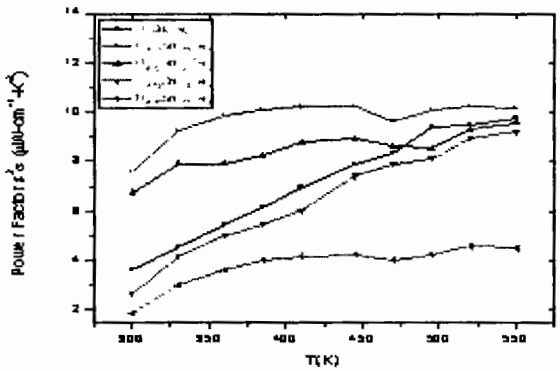

Figure (A)

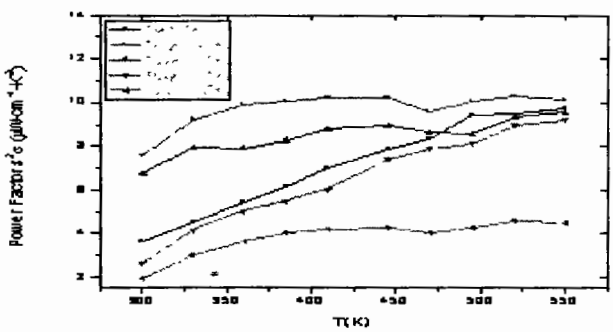

Figure (B)

Figure 8.5: Power Factor of $Tl_{10-x}ATe_6$ at 300K, 400 K, and 550K.

Table 8.4: Power Factor of $Tl_{10-x}ATe_6$ at 300K, 400 K, and 550K.

Sample	Power Factor	Power Factor
	1.8	4.7
	2.8	8.5
	6.8	10
	7.9	10.2
	3.6	9.7

Table (A)

Sample	Power Factor $S^2\sigma$ ($\mu Wcm^{-1}K^{-2}$) at 300K	Power Factor $S^2\sigma$ ($\mu Wcm^{-1}K^{-2}$) at 550K
$Tl_9Sn_1Te_6$	1.5	4.5
$Tl_{8.75}Sn_{1.25}Te_6$	2.4	8.4
$Tl_{8.50}Sn_{1.50}Te_6$	6.5	9.8
$Tl_{8.25}Sn_{1.75}Te_6$	7.5	10
$Tl_8Sn_2Te_6$	3.3	9.5

Table (B)

8.6 Conclusion

We had doped "Sn & Pb" in "$Tl_{10-x}ATe_6$" Substance by way of different absorptions. The different concentration of the doped "Sn and Pb" in the $Tl_{10-x}ATe_6$ nano-particles is synthesized by the solid state reaction within an evacuated silica sealed tube with the pellet size is 5*1*1 mm^3 in the rectangular dimension. The pellets were cut into roughly 5x1x1 mm^3 rectangular shapes for the electrical transport measurements using a 4-probe resistivity technique. In addition, inspect the physical possessions of these compounds with x= 1.96, 1.97, 1.98, 1.99, 2.00. The structural, and thermo-electrical properties of samples and determined using the Ball-Milling method. According to the results of the structural analysis, "$Tl_{10-x}ATe_6$" is structurally and space group which is 14/mcm is equivalent to Tl_5Te_3. The relative elements in the compounds show reliable peaks. And there are no more peaks in the compounds. This shows that we obtain crystal structure according to synthesized compound samples and demonstration that the sample is free of impurities and displacement. An EDX method is used for elemental analysis of a sample and confirms that the percentage of elements present in the sample is correct.

Although the electrical properties and characterization displayed that the pure materials behave like a semiconductor, enhancing the "Sn" & "Pb" concentration, these materials exhibit metallic properties demonstrating that as temperature increases, the electrical conductivity decreases.

All of the samples show the positive Seebeck coefficient value was positive. The Seebeck coefficient increased as the "Sn & Pb" concentration increased owing to an enhancement in the metallic performance of the material and a lower in its thermal

conductivity. When the temperature was increased, the Seebeck coefficient increased as well reaching its maximum value for "$Tl_{10-x}ATe_6$". S=+160.63 μVK^{-1}

The results showed an improved quality of the power factor (PF). It increases with increasing the concentration of "Sn" up to "Sn" & "Pb" =2.00. So, "$Tl_{10-x}ATe_6$" has a lower power factor due to the rate of electrical conductivity. Highest value of "$Tl_{10-x}ATe_6$" power factor was 10.2 $\mu Wm^{-1}K^{-2}$ observed. The essential aim of this research is to better the thermoelectric efficiency and as a result, the quality of thermoelectric applications.

The Seebeck coefficient of $Tl_{10-x}ATe_6$ nanoparticles increases due to "Pb" and "Sn" doping. Both nanoparticles' phases are changing as well. It also shows that as the temperature rises, the electrical conductivity of the $Tl_{10-x}ATe_6$ nanoparticles decreases due to "Pb" and "Sn" doping. Because the enhancement of Seebeck coefficient increases then the power factor of compounds increases as well.

8.7 References

[1] Rowe DM. Thermoelectrics Handbook: Macro to Nano, CRC Press. Taylor & Francis Group, Boca Raton, FL, USA (2006).

[2] Sharp JW, Sales BC, Mandrus DG, Chakoumakos BC. "Thermoelectric properties of Tl_2SnTe_5 and Tl_2GeTe_5." Appl. Phys. Lett. **74**, (1999), 3794–3796.

[3] Kurosaki K, Kosuga A, Muta H, Uno M, Yamanaka S. "A high-performance thermoelectric bulk material with extremely low thermal conductivity." Appl. Phys. Lett. **87**, (2005), 061919.

[4] Sales BC, Chakoumakos BC, Mandrus D. "Thermoelectric properties of thallium filled skutterudites." Phys. Rev. B **61**, (2000), 2475–2481.

[5] Harnwunggmoung A, Kurosaki K, Muta H, Yamanaka S. "High-temperature thermoelectric properties of thallium-filled Skutterudites." Appl. Phys. Lett. **96**, (2010).

[6] Yamanaka S, Kosuga A, Kurosaki K. "Thermoelectric properties of Tl_9BiTe_6." J. Alloys Comp. **352**, (2003), 275–278.

[7] Guo Q, Chan M, Kuropatwa BA, Kleinke H. "Enhanced thermoelectric properties of variants of Tl_9SbTe_6 and Tl_9BiTe_6." Chem. Mater. **25**, (2013), 4097–4104.

[8] Bryan A, Abdeljalil, Kleinke H. "Phase range and physical properties of the thallium tin tellurides $Tl_{10-x}Sn_xTe_6$ ($x \leq 2.2$)." Chem. Mater (2011), 6768–6772.

[9] Guo Q, Assoud A, Kleinke H. "Improved bulk materials with thermoelectric figure-of merit > 1: $Tl_{10-x}Sn_xTe_6$ and $Tl_{10-x}Pb_xTe_6$." Adv. Energy Mater. **4**, (2014), 1400348.

[10] Wölfing B, Kloc C, Teubner J, Bucher E. "High performance thermoelectric Tl_9BiTe_6 with an extremely low thermal conductivity". Phys. Rev. Lett. **86**, (2001), 4350–4353.

[11] Kosuga A, Kurosaki K, Muta H, Yamanaka S. Thermoelectric properties of Tl–X–TeTl–X–Te (X=GeX=Ge, Sn, and Pb) compounds with low lattice thermal conductivity. J. Appl. Phys. **99**, (2006), 063705.

[12] Sankar CR, Bangarigadu-Sanasy S, Assoud A, Kleinke H., "Syntheses, crystal structures and thermoelectric properties of two new thallium tellurides: Tl_4ZrTe_4 and Tl_4HfTe_4." J. Mater. Chem. **20**, (2010), 7485–7490.

[13] Sankar CR, Guch M, Assoud A, Kleinke H., "Structural, thermal, and physical properties of the thallium zirconium telluride Tl_2ZrTe_3." Chem. Mater. **23**, (2011), 3886–3891.

[14] Bangarigadu-Sanasy S, Sankar CR, Assoud A, Kleinke H. "Crystal structures and thermoelectric properties of the series $Tl_{10-x}La_xTe_6$ with $0.2 \leq x \leq 1.15$." Dalton Trans. **40**, (2011) 862–867.

[15] Kosuga A, Kurosaki K, Muta H, Yamanaka S. (2006). Thermoelectric properties of Tl–X–TeTl–X–Te (X=GeX=Ge, Sn, and Pb) compounds with low lattice thermal conductivity. J. Appl. Phys. **99**, (2006), 063705.

[16] Bangarigadu-Sanasy S, Sankar CR, Schlender P, Kleinke H. (2013). Thermoelectric properties of $Tl_{10-x}Ln_xTe_6$, with Ln = Ce, Pr, Nd, Sm, Gd, Tb, Dy, Ho, and Er, and $0.25 \leq x \leq 1.32$. J. Alloys Comp. **549**, (2013), 126–134.

[17] Y. K. Kurosaki, "Thermoelectric properties of Tl_9BiTe_6," Journal of Alloys and Compounds, (2003), 275–278.

[18] Z. Cai, L. Guo, X. Xu, Y. Yan, K. Peng, G. Wang, and X Zhou, J. Electronic Mater. **45**, (2016), 1441.

[19] R.J. Mehta, Y Zhang, C. Karthika eta, "A new class of doped nano bulk high-figure-of merit thermoelectrics by scalable bottom-up assembly" Nature Materials, **11**, (2012), 233-240.

[20] K. Kurosaki, A. Kosuge, H. Muta, M. Uno, S. Yamanaka, "Compositional Difference of Thermoelectric Properties in Ag_9TlTe_5." Applied Phys. Letts. **87**, (2005), 06191.

[21] J. Yang, F. R. Stablers, "Automotive Applications of Thermoelectric Materials." J. Electrn.Mater. **38**, (2009), 1245.

Chapter # 09

9.1 Summary and Conclusion

This dissertation summarizes key strategies for improving the thermoelectric materials for practical use and increase efficiency of the device environmentally friendly TlTe which has been thoroughly examined. There are a number of methods for decreasing the lattice thermal conductivity, such as point defects, grain boundary, harmonicas, and nanostructuring, as well as optimizing the figure of merit through carrier improvement, resonance energy level, band convergence, and band gap tuning. The thermoelectric properties of TlTe can be significantly improved through the use of synergistic band engineering and structural engineering techniques. We have conducted numerous experimental and theoretical studies, which include synthesis, electronic microscopy characterization of analyze and sintered nanostructure samples, thermoelectric property calculations, density of states, and band structure calculations. Maximum power factor at room temperature is caused by the resonance energy level in TlTe, which is caused by "Sn" doping. The results show that co-doping "Sn/Pd" with excess Te resulted in a higher figure of merit in TlTe. TlTe's thermoelectric properties can be improved by adjusting the ratio of "Sn" and "Pb". Using phonon modelling studies, it is possible to create phonon scattering sources at multiple scales, such as point defects, nano-precipitates, and grain boundaries. The results of this thesis provide a clear roadmap for the evolution of high performance thermoelectric compounds through the use of doping, nano-structuring, and band engineering. Specifically,

(i) Ball milling has been used to create "Sn" doped $Tl_{10}Te_6$ particles. The pristine Seebeck of $Tl_{10}Te_6$ is increased from ~ 80 $\mu V\ K^{-1}$ to ~ 158 $\mu V\ K^{-1}$due to the damage of density of states in the valence band by "Sn". An extensive TEM analysis of $Tl_{10}Te_6$ nano-precipitate revealed a tetragonal crystal structure. In $Tl_{10}Te_6$, a small change in the lattice parameters leads to lattice dislocations in the matrix, which reduce the system's thermal conductivity using scatter heat-carrying phonons.

(ii) A lot of research has gone into co-doping "Sb" with "Te". The Seebeck coefficient of the Sb co-doped $Tl_{10}Te_6$ scheme was importantly higher than the pristine $Tl_{10}Te_6$ system with Pisarenko plot. This comparison is founded on an individual parabolic band model. We believe that "Sb" significantly reduced the size $Tl_{10}Te_6$-related valence band at outset. So that heavy holes in $Tl_{10}Te_6$ could participate

in the electron-hole transport system. In addition, there is also a large amount of Nano-particles forming in the $Tl_{10}Te_6$ matrix. The presence of point defects, Nano precipitates, and grain boundaries importantly increased system's whole power factor from ~ 1.02 $\mu Wcm^{-1}K^{-2}$ to ~ 10.2 $\mu Wcm^{-1}K^{-2}$, resulting in an increase in high thermoelectric performance.

(iii) Band engineering and structure engineering were both used to improve the electronic and thermal properties of the co-doped $Tl_{10}Te_6$ system. This system was improved by using the 1:2 dopant ratio between "Sn" and "Sb". The phonon scattering is aided by the large atomic mass difference between the guest (Pb) and host (Sb) atoms. Theoretical calculations indicate that "Sn/Sb" co-doping modifies the pristine $Tl_{10}Te_6$ band structure. The electrical transport properties were improved by the presence of both resonance energy level and valence band convergence. Strain defects in Nano-precipitates containing numerous "Sn" and "Sb" lead to an increase in the total power factor from ~ 1.66 $\mu Wcm^{-1}K^{-2}$ to ~ 8.56 $\mu Wcm^{-1}K^{-2}$.

(iv) The co-precipitation method was used to successfully achieve co-doping in $Tl_{10}Te_6$. According to the results of extensive theoretical calculations, there has been important for valence band convergence and principal band gap expansion, which has resulted in an increase in PF from ~5.01 $\mu Wcm^{-1}K^{-}$ to ~8.25 $\mu Wcm^{-1}K^{-}$ in the pristine $Tl_{10}Te_6$. Point defects, strain field dislocations, and grain boundaries all contribute necessary.

(v) 1:2 dopant ratio was used between "Sb" and "Pb" to decrease the thermal while electrical properties of the "Sn/Sb" co-doped TlTe system are enhanced. This enhancement occurred through the exploitation of band engineering and structural engineering. Phonon scattering is aided by the sizeable atomic mass difference between the guest (Sb) and host (Sn) atoms. Theoretical calculations indicate that Pb/Sb co-doping modifies the pristine $Tl_{10}Te_6$ band structure the electrical transport properties were improved by the presence of both resonance energy level and valence band convergence. Resulting in a high ZT, strain defects in Nano-precipitates containing numerous Sn and Sb which help to increase the scattering of phonon and decrease the lattice thermal conductivity increasing the value of ZT. We calculated that average ZT was used to figure out device and found that it is achievable.

(vi) Ball milling has been used to create "Sn" doped $Tl_{10}Te_6$ particles. The pristine Seebeck of $Tl_{10}Te_6$ is increased from ~ 4.7 $\mu Wcm^{-1}K^{-2}$ to ~ 10.2 $\mu Wcm^{-1}K^{-2}$ due to the deformation of density of states in the valence band by "Sn. An extensive TEM analysis of $Tl_{10}Te_6$ Nano-precipitate revealed a tetragonal crystal structure. In $Tl_{10}Te_6$, a small change in the lattice parameters leads to lattice dislocations in the matrix, which reduce the system's thermal conductivity. The Seebeck coefficient of the Sb co-doped $Tl_{10}Te_6$ system was increased by the pure TlTe system with Pisarenko plot. This comparison is based on a single parabolic band model.

9.2 Recommendations

It is possible to make notes of the suggestions and recommendations made below for future reference.

- The crystals synthesized in this study are several nanometers in size. It would be interesting to synthesize nanometer-sized particles and study their effect on TlTe thermoelectric properties when doped with a suitable dopant. In this regard, During the synthesis process, it is possible to regulate the concentration and the amount of sodium hydroxide used. It may be necessary to enhance the sintering parameters in order to obtain solid bulk sintered samples that are free of cracks
- Additionally, phonon density of states calculations are necessary to understand the system's phonon behavior. As a result ,the matrix's phonon propagation and scattering can be better understood.
- Until now ,all thermoelectric materials based on TlTe have been reported to be P-type. As a result, there is considerable scope for research into n-type TlTe materials as well.

Additionally, it is strongly advised to manufacture an exemplary device for application physically. The device efficiency should be compared to the ZT obtained from the bulk sample.

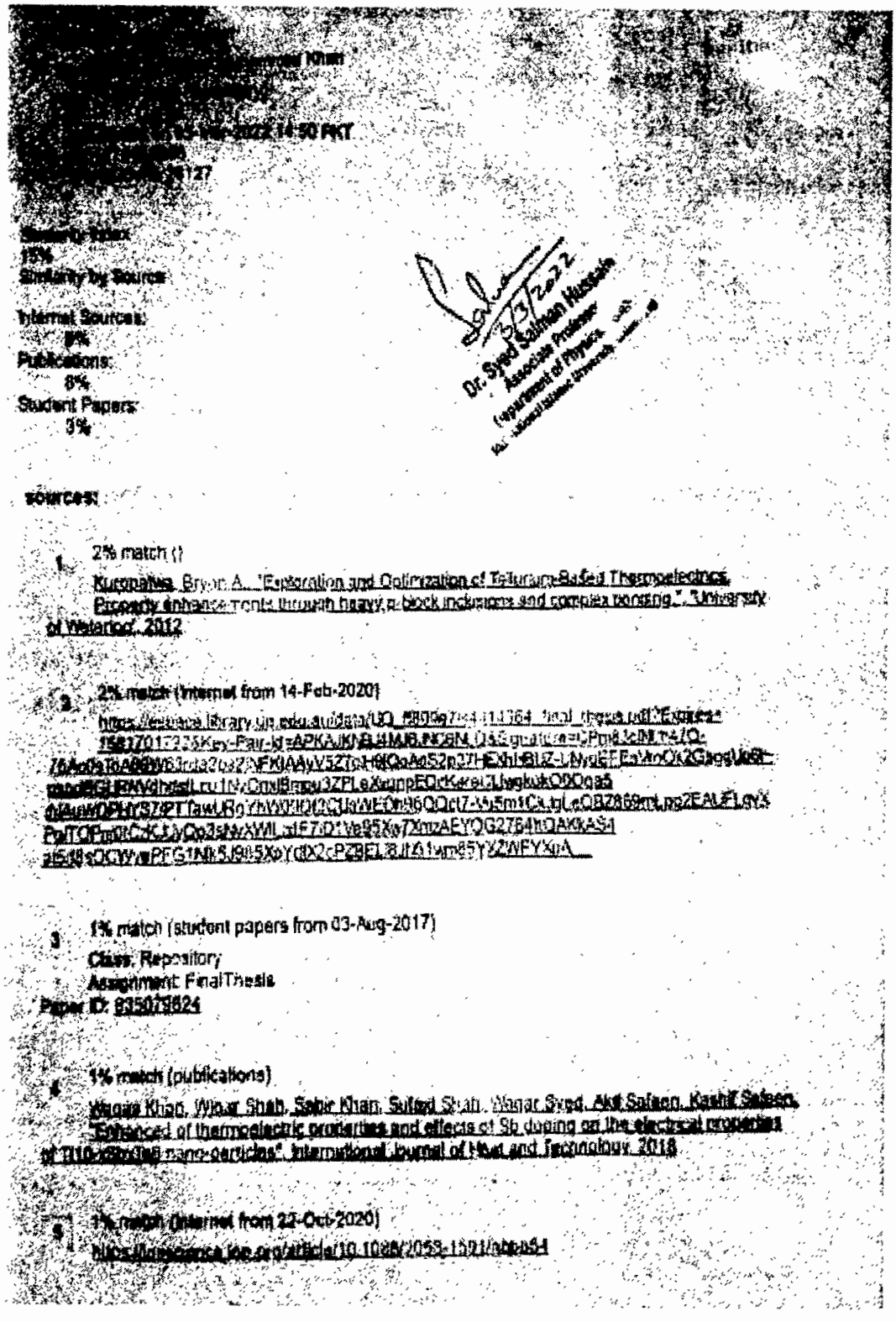

[redacted] Khan

[redacted] 14:50 PKT

[redacted] 127

Similarity Index
15%
Similarity by Source

Internal Sources:
9%
Publications:
8%
Student Papers:
3%

23/2022
Dr. Syed Sulfiqar Hussain
Associate Professor
(Department of Physics)

SOURCES:

1 2% match ()
Kucuman, Bryan A., "Exploration and Optimization of Tellurium-Based Thermoelectrics: Porosity Enhancements through heavy p-block inclusions and complex doping.", University of Waterloo, 2012

2 2% match (Internet from 14-Feb-2020)
https://ezproxy.library.qn.edu.au/data/UQ_[redacted]_final_thesis.pdf?Expires=1583701373&Key-Pair-Id=APKAJKVEJHMBJNQ6NQ&Signature=[redacted]

3 1% match (student papers from 03-Aug-2017)
Class: Repository
Assignment: FinalThesis
Paper ID: 835079824

4 1% match (publications)
Waqas Khan, Wajid Shah, Sabir Khan, Sufyal Shah, Nasar Syed, Akif Safeen, Kashif Safeen, "Enhanced of thermoelectric properties and effects of Sb doping on the electrical properties of TiO2-ZnO(Al) nano-particles", International Journal of Heat and Technology, 2018

5 1% match (Internet from 22-Oct-2020)
https://iopscience.iop.org/article/10.1088/2053-1591/aba954

Summary and Conclusion

Chalcogenide Letters Vol. 14, No. 2, February 2017, p. 61 - 68

EFFECTS OF Pb DOPING ON THE SEEBECK CO-EFFICIENT AND ELECTRICAL PROPERTIES OF $Tl_{8.67}Pb_xSb_{1.33-x}Te_6$ CHALCOGENIDE SYSTEM

W. H. SHAH*, A. KHAN, M. WAQAS, W.A. SYED
Department of Physics, Faculty of Basic and Applied Sciences, International Islamic University,H-10, Islamabad, Pakistan

We present the effects of Pb doping on the electrical and thermoelectric properties of Tellurium Telluride $Tl_{8.6}Pb_xSb_{1.33-x}Te_6$ (x=0.61, 0.63, 0.65, 0.67, 0.68, 0.70), prepared by solid state reactions in an evacuated sealed silica tubes. Additionally crystal structure data were used to model the data and support the findings. Structurally, all these compounds were found to be phase pure as confirmed by the x-rays diffractometery (XRD) and energy dispersive x-rays spectroscopy (EDS) analysis. The Seebeck co-efficient (thermopower) (*S*) was measured for all these compounds which show that *S* increases with increasing temperature from 295 to 550 K. The Seebeck coefficient is positive for the whole temperature range, showing p-type semiconductor characteristics. Complex behavior of Seebeck coefficient for Pb doped compounds has been observed that at room temperature, the values of S for *Pb* based compounds have complex behavior, first S decreasing with increase in *Pb* concentration i.e. x=0.65, and then S increases with increase in *Pb* contents upto x=0.70. Similarly the electrical conductivity (σ) and the power factors have also complex behavior with *Pb* concentrations. The power factor ($PF=S^2\sigma$) observed for $Tl_{8.67}Pb_xSb_{1.33-x}Te_6$ compounds are increases with increase in the whole temperature range (290 K-550 K) studied here. Telluride's are narrow band-gap semiconductors, with all elements in common oxidation states, according to $(Tl^+)_9(Sb^{3+})(Te^{2-})_6$. Phases range were investigated and determined with different concentration of *Pb* with consequents effects on electrical and thermal properties.

(Received December 30, 2016; Accepted February 21, 2017)

Keywords: Pb doping, Thermoelectric properties of Tellurium Telluride, Seebeck co-efficient, Electrical conductivity, Effects on power factor

1. Introduction

Thermoelectrics (TE's), as one of the most promising approaches for solid-state energy conversion between heat and electricity, is becoming increasingly important within the last decade as the availability and negative impact of fossil fuels draw increasing attention. Various TE's materials with a wide working temperature range (from 10 to 1000 K) for different applications in cooling and power generation have been extensively studied [1-5]. Tellurium telluride ((Tl_5Te_3)) is one of the most studied and used intermediate temperature TE materials with good thermoelectric properties , suitable for power generation applications such as waste heat recovery [1] and potentially in solar energy conversion [2]. Tellurium telluride based alloys are very attractive thermoelectric (TE) materials due to their high energy conversion efficiency at ambient temperature without requiring any driving parts or cooling system in electronic devices [3-7].

The dimensionless figure of merit, $ZT=S^2\sigma T\kappa$, where σ is the electrical conductivity, κ is the thermal conductivity, *S* is the Seebeck coefficient, and *T* is the absolute temperature determine the effectiveness of a material for thermoelectric applications [8]. The thermal and electrical properties are determined by the power factor, defined as $S^2\sigma$. The power factor can be optimized as a function of the carrier concentration; with the help of different doping concentration and injections of free electrons in the chalcogenide system.

*Corresponding author: wqarhussain@yahoo.com

Summary and Conclusion

Chalcogenide Letters Vol 14. No 5. May 2017. p 187 - 193

OPTIMIZATION OF POWER FACTOR IN SNDOPED $Tl_{10-x}Sn_xTe_6$ THERMOELECTRIC CHALCOGENIDENANO-MATERIALS

W. H. SHAH*, W. M. KHAN, S. TAJUDIN, M. TUFAIL, W. A. SYED
Department of Physics, Faculty of Basic and Applied Sciences, International Islamic University,
H-10, Islamabad, Pakistan

The electrical and thermal properties of the doped Tellurium Telluride ($Tl_{10}Te_6$) chalcogenide nano-particles are mainly characterized by a competition between metallic (hole doped concentration) and semi-conducting state. We have studied the effects of Sn doping on the electrical and thermoelectric properties of $Tl_{10-x}Sn_xTe_6$ ($1.00 \leq x \leq 2.00$), nano-particles, prepared by solid state reactions in sealed silica tubes and ball milling method. Structually, all these compounds were found to be phase pure as confirmed by the x-rays diffractometery (XRD) and energy dispersive X-ray spectroscopy (EDS) analysis. Additionally crystal structure data were used to model the data and support the findings. The particles size was calculated from the XRD data by Scherrer's formula. The EDS was used for an elemental analysis of the sample and declares the percentage of elements present in the system. The thermo-power or Seebeck co-efficient (S) was measured for all these compounds which show that S increases with increasing temperature from 295 to 550 K. The Seebeck coefficient is positive for the whole temperature range, showing p-type semiconductor characteristics. The electrical conductivity was investigated by four probe resistivity techniques revealed that the electrical conductivity decreases with increasing temperature, and also simultaneously with increasing Sn concentration. While for Seebeck coefficient the trend is opposite which is increases with increasing temperature. These increasing behavior of Seebeck coefficient leads to high power factor which are increases with increasing temperature and Sn concentration except For $Tl_8Sn_2Te_6$ because of lowest electrical conductivity but its power factor increases well with increasing temperature.

(Received February 10, 2017, Accepted May 15, 2017)

Keywords: Sn doping in Tellurium Telluride nano-materials, Electron holes competition, Seebeck co-efficient, effects of Sn doping on electrical conductivity, Effects on Power factor.

1. Introduction

The increasing awareness of declining global energy resources alternative method of power generation for example the thermoelectric energy conversion becomes increasingly important.[1] Thermoelectric (TE's) materials with a wide working temperature range for different applications in cooling and power generation have been extensively studied [1-5]. Tellurium telluride (Tl_5Te_3) is one of the most studied and used intermediate temperature TE materials with good thermoelectric properties, suitable for power generation applications.

The effectiveness of thermoelectric generator is determined by the investigation of power factor, which is measured by the square of Seebeck coefficient multiplied by electrical conductivity at particular temperature, i.e. $PF=S^2\sigma$ The power factor depends substantially on details of the electronic band structure and carrier scattering mechanism. The important condition for achieving a large power factor is by maximizing the Seebeck co-efficient S^2 and minimizing electrical conductivity σ. These conditions can be achieved in materials, having complex band structure, high degree of degeneracy with several co-existing bonding types and scattering

*Corresponding author: wqalhussain@yahoo.com

Summary and Conclusion

Chalcogenide Letters Vol. 16, No 7, July 2019, p 343 - 349

INCREASING THE POWER FACTOR BY Sb DOPED $Tl_{10-x}Sb_xTe_6$ IN CHALCOGENIDE SYSTEM

W. M. KHAN[a*], W. H. SHAH[a], S. SHAH[a], S. KHAN[a], W. A. SYED[a], N. AHMAD[a], A. SAFEEN[b], K. SAFEEN[b]
[a]*Department of Physics, Faculty of Basic and Applied Sciences, International Islamic University, Islamabad, Pakistan*
[b]*Department of Physics, Abdul Wali Khan University, Mardan, Pakistan*

The nano-particles system which is Thallium antimony telluride $Tl_{10-x}Sb_xTe_6$ with different doping with concentration of Sb (x = 1.00, 1.250, 1.500, 1.750, 2.00) were synthesized by solid state reaction method and then the nano-particles from the ingot by ball milling techniques. X-rays diffraction analysis has defined the phase purity of the system, as there is no extra peaks were observed. EDX spectroscopy result confirmed the elemental composition of $Tl_{10-x}Sb_xTe_6$. It is increasing thermal properties as the Sb is doping in the nano-system. While the electrical conductivity (σ) decreased in nano system otherwise the Seebeck coefficient (S) is increased. The different behavior of See-beck co-efficient and electrical conductivity which cause to increase the power factor. Our present study to show that the use of $Tl_{10-x}Sb_xTe_6$ is best nano-particles for thermos-electric generator

(Received March 21, 2019; Accepted July 16, 2019)

Keywords: Tellurium Telluride Nano-Particles, Sb doping, See-beck co-efficient, Electrical conductivity, Power factor

1. Introduction

It is statistical results show that up to 60% of energy is losing in vain worldwide, most in the form of waste heat. High value of performance which is thermoelectric (TE) materials that is directly and inversely change heat energy to electrical energy have thus draw growing attentions of governments and research institutes [1]. Thermoelectric system is an environment-friendly energy conversion technology with the advantages of small size, high reliability, no pollutants and feasibility in a wide temperature range. However, the efficiency of thermoelectric devices is not high enough to rival the Carnot efficiency [2, 3].

Many new thermoelectric materials or new material with which have high performance have been found such as skutterudites with high scattering rates of phonons [4,5], silicon nanowires [6,7], TE thin films [8], and nanostructured bismuth antimony telluride bulk alloys [9]. It was thinking that high barriers and extremely degenerately doped superl-attices must achieve significant increases in thermos-electric power factor over bulk materials [10]. It was revised that electron transport which are perpendicular to the barrier and investigated that large number of degenerate doped semiconductor or metal super-lattices could achieve which shows the power factors higher than the bulk and determined that non-maintenance of transverse momentum can have a large effect (especially in the case of metal super-lattices) by increasing the number of electrons contributing to conduction by thermionic emission [11].

The See-beck co-efficient for different metals and largely doped semiconductors is determined. The equation is related by the power factor, which is directly proportional to the See-beck coefficient squared, we determined that increasing the See-beck coefficient by having their high effective mass and low carrier concentration, which is in the semiconducting region, is need in a thermoelectric material. Ionic compounds will give us high effective mass with low mobility, while semiconductors with small electro-negativity differences have high mobility and low

* Corresponding author: waqaskhanwp@yahoo.com

Summary and Conclusion

Chalcogenide Letters Vol 16, No 8, August 2019, p. 395 - 403

ENHANCEMENT OF POWER FACTOR BY Sn DOPING IN $Tl_8Sb_{2-x}Sn_xTe_6$ NANO-CHALCOGENIDE SYSTEM

W. M. KHAN*, W. H. SHAH, M. TUFAIL, S. KHAN, W. A. SYED, N. AHMAD
Department of Physics, Faculty of Basic and Applied Sciences
International Islamic University, Islamabad, Pakistan

We have prepared the quaternary thermoelectric nanoparticles, thallium tin antimony telluride $Tl_8Sb_{2-x}Sn_xTe_6$ where the concentration of the Sn is (1.96, 1.97, 1.98, 1.99, 2.00) using the solid state reactions techniques. The nanoparticles have been prepared by the ball mining method. The Sn is doping in the quaternary compound which have changes their electrical and thermal properties. The crystal structure has been analyzed by the x-rays diffractometery (XRD), to determine the phase structure. The XRD data shows no extra peak; confirm the purity of the sample. The energy dispersive spectroscopy (EDX) shows the stoichiometric elemental ratio of the compound studied here. With the increasing concentration of the Sn in the compound, the electrical conductivity is decreases as temperature is increases while the Seebeck coefficient is increased as temperature is increases. At last, both electrical conductivity and Seebeck coefficient is increased. So that the power factor is also increased in the range of 300-550 K. The compound which has Sn concentration is 0.61, has the highest power factor at 550 K which is the 8.9 $\mu Wcm^{-1}K^{-2}$.

(Received April 24, 2019; Accepted August 11, 2019)

Keywords: Quaternary thermoelectric, Nanoparticles, Seebeck coefficient, Electrical Conductivity

1. Introduction

The chalcogenide compounds which are doped the metallic like properties become the semiconductors have the different applications in the thermoelectric appliances [1-7] solar volte's [8-11] different radiations detectors [12-14] and super capacitors [15-17]. Basically, there is insulators nature so there are different types of the chalcogenide materials found it [18-22]. Due to heavy atomic weight it has the marvelous properties like the low electrical conductivity for determining the detectors [19] and the low thermal and high electrical conductivity properties for the thermoelectric materials [20]. Our major aim is to change the chemistry of the chalcogenide material for benefits of the human beings. The thermoelectric materials is used to convert thermal energy into electrical energy [21, 23, and 24], in a reliable way [25] The most common example is exhausted of gases from the cars. So that there are some thermoelectric materials are found like skutterides [26] lead telluride [27] half Haussler's compound [28].

The motivation of thallium based compounds are, i) due to the heavy atomic weight so that it is reducing the thermal conductivity and ii) creating the complex behavior due to their lone pair of it which helps to create the different properties of compounds e.g., Tl_9SbTe_6 [29] Tl_9BiTe_6 [30] $Tl_{10-x}Sn_xTe_6$ [31] $TlBiTe_2$ [32] $TlSbTe_2$ [33] and Tl_6AgTe_3 [34].

The prime reason of this project is to design and fabricate such nano-materials system which are more efficient, i.e. have high power factor and environment friendly. The effectiveness of the material can be evaluated by the figure of merit $ZT=TS^2\sigma\kappa^{-1}$ where S is the Seebeck coefficient, σ is the electrical conductivity, κ is the thermal conductivity and T is the difference of the temperature [36] If the figure-of-merit is high, it has high efficiency that of converting the thermal energy into electrical energy. The figure of merit is depend on the high Seebeck and electrical conductivity while low thermal conductivity. So the narrow band gap doped semiconducting nano-system will be the best option [35].

*Corresponding author: waqaskhanrwp@yahoo.com

Summary and Conclusion

IOP Publishing Mater. Res. Express 7 (2020) 105010

Materials Research Express

PAPER

Toward controlled thermoelectric properties of Pb and Sb co-doped nanostructured Thallium Telluride for energy applications

Waqas Muhammad Khan [1], Altaf Ur Rahman [2,5], Muhammad Tufail [1], Muhammad Ibrar [3], Wiqar Hussain Shah [1], Waqar Adil Syed [4] and Banat Gul [1]

[1] Department of Physics, International Islamic University, Islamabad 44000, Pakistan
[2] Department of Physics, Riphah Institute of Computing & Applied Sciences, Riphah International University, 13 km Raiwind Rd, Chamru Pur Lahore, Pakistan
[3] Department of Physics, Islamia College Peshawar, Khyber Pakhtunkhwa, Peshawar 25120, Pakistan
[4] Military College of Engineering, National University of Science and Technology (NUST), Islamabad, Pakistan
[5] Authors to whom any correspondence should be addressed.

E-mail: altaf.urrahman@riphah.edu.pk and waqar.hussain@mce.edu.pk

OPEN ACCESS

RECEIVED
10 August 2020

REVISED
15 September 2020

ACCEPTED FOR PUBLICATION
24 September 2020

PUBLISHED
21 October 2020

Keywords: quaternary compound, electronic properties, thermoelectric properties, DFT, WGA

Abstract

Here, the structure-dependent electronic, thermal, and transport properties of nanostructured thallium telluride ($Tl_8Pb_xSb_{2-x}Te_6$) through controlled variation in Pb and Sb (x = 1.96, 1.97, 1.98, 1.99) concentrations have been investigated. In the temperature and concentration-dependent electrical conductivity measurements, the highest electrical conductivity 131.96 $\times 10^3\ \Omega^{-1}m^{-1}$ at 300 K was measured for x = 1.99 and the maximum observed Seebeck value for the optimized $Tl_8Pb_{1.96}Sb_{0.04}Te_6$ nanoparticles was 110.7 $\mu V/K$ at 550 K. Such an increased value of the Seebeck coefficient led to the achievement of a significantly improved high-power factor, which was found to be increasing with temperature and decreasing with the increase of Pb concentration. The density functional theory calculations performed for Pb and Sb co-doped Tl_5Te_3 resulted in the enhanced σ_e and S with a significant reduction in electronic thermal conductivity (κ_e) and is found consistent with experimentally measured κ_e. The highest ZT = 0.35 and 0.18 were recorded experimentally and theoretically for Pb and Sb co-doped in Tl_5Te_3 nanoparticles.

1. Introduction

The current global energy deficit and the environmental challenges ahead is an alarming situation for upcoming generations. The rise in the average temperature of Earth and worldwide pollution has produced far-reaching implications and damage to the ozone. The extraordinary demand and production and conversion of energy for domestic and industrial usage motivate rigorous investigation in the energy sector to explore numerous resources employing a different kind of nanoscale materials and technologies [1]. Also, considerable efforts have been devoted to achieving a possible control over the energy crisis and global warming through the minimization of energy losses in various industrial sectors. In the 21st century, the energy crisis and unrelated waste energy management are two key problems [2]. Various sources of energy are wind, solar, tidal, biofuel, geothermal and nuclear energy. Heat energy is utilized in human actions and industry procedures; at that instant wasted thermal energy has vanished without used energy change [3].

Historically, more than a century ago, the first-ever thermoelectric effect was discovered by Thomas Johanne Seebeck [4, 5] and Jean Charles Athanase Peltier [6, 7]. This effect is based on the principle of the production of electrical energy using a temperature gradient. Notable performance has been reported for Bi_2Te_3 for being an efficient thermoelectric (TE) material. It is worth mentioning here that for thermoelectric application a high temperature thermodynamically stable materials are desirable [7, 8]. Therefore, thermal stability and good thermoelectric properties make such materials prognosticating for next generation technologies utilizing waste heat and to convert it into useful electrical energy [9]. On average, industrial processes effectively consume and utilize only about 40% of the total energy and the balance is rejected in the form of waste heat. It is possible to

Summary and Conclusion

Journal of Ovonic Research Vol. 17. No 2. March - April 2021. p. 201 - 208

Effects on the seebeck co-efficient and electrical properties of $Tl_{10-x}ATe_6$ (A= Pb & Sn) in chalcogenide system

W. M. Khan*, W. H. Shah. N. Khan. M. Tufail. S. Khan, W. A. Syed
Department of Physics. Faculty of Basic and Applied Science. International Islamic University H-10, Islamabad, Pakistan

The different elements are doping in the tellurium telluride to determine the different properties like electrical and thermal properties of nanoparticles. The chalcogenide nanoparticles can be characteristics by the doping of the different metals which are like the holes. We present the effects of Pb and Sn doping on the electrical and thermoelectric properties of Tellurium Telluride $Tl_{10-x}Pb_xTe_6$ and $Tl_{10-x}Sn_xTe_6$(x=1.00. 1.25. 1.50. 1.75. 2.00) respectively. which were prepared by solid state reactions in an evacuated sealed silica tubes. Structually. all these compounds were found to be phase pure as confirmed by the x-rays diffractometery (XRD) and energy dispersive X-ray spectroscopy (EDS) analysis. The thermo-power or Seebeck co-efficient (S) was measured for all these compounds which show that S increases with increasing temperature from 295 to 550 K. The Seebeck coefficient is positive for the whole temperature range. showing p-type semiconductor characteristics. Similarly. the electrical conductivity (σ) and the power factors have also complex behavior with *Pb and Sn* concentrations The power factor ($PF=S^2\sigma$) observed for $Tl_{10-x}Pb_xTe_6$ and $Tl_{10-x}Sn_xTe_6$ compounds are increases with increase in the whole temperature range (290 K-550 K) studied here Telluride's are narrow band-gap semiconductors, with all elements in common oxidation states, according to $(Tl^{+})_9(Pb^{3-})(Te^{2-})_6$ and $(Tl^{+})_9(Sn^{3-})(Te^{2-})_6$. Phases range were investigated and determined with different concentration of *Pb and Sn* with consequents effects on electrical and thermal properties

(Received August 31. 2020. Accepted April 8. 2021)

Keywords. Pb and Sn doping. Seebeck coefficient. Electrical conductivity. Power factor

1. Introduction

The thermo-electro-materials are now used as the renewable energy It is used as the place of the coal. water tides. solar cells etc. The thermo electro-materials have more efficiency and reliable. Thermoelectric is one of the most important approaches in the solid state physics which can be converted the heat energy in the electrical energy. help to increase the efficiency. effectiveness and competency. It's importance is increase since last twenty years when the ease of use of fossil fuel is decrease. So there are different thermoelectric materials are used for the different temperatures from 10K to the 1000 K which are used in the different applications for the cooling and heating [1-5]. Tellurium telluride is one important compound of the thermoelectric material which is studied, modified and increases the efficiency for the more and more applications for generation of power [1] and solar cells [2]. Tellurium telluride is a basically alloy that is used for the increases the energy conversion efficiency at the any temperature of the heating and cooling in the electrical circuit [3-7].

The figure of merit is

$$ZT=\frac{S^2\sigma T}{k}$$

where is σ is the electrical conductivity. k is the thermal conductivity. S is the see-beck coefficient. and T is the absolute temperature which is determined the efficiency of the thermo

* Corresponding author. waqaskhanrwp@yahoo com